

**Modeling Dislocation Sources and Plastic Flow through Grain
Boundaries in Mesoscopic Field Dislocation Mechanics**

Submitted in partial fulfillment of the requirements for

the degree of

Doctor of Philosophy

in

The Department of Civil and Environmental Engineering

Saurabh Puri

B.Tech., Mining Engineering, Institute of Technology, Banaras Hindu University,
India

M.S., Mining Engineering, University of Utah, USA

Carnegie Mellon University
Pittsburgh, PA

December, 2009

ABSTRACT

This work involves the modeling and understanding of mechanical behavior of crystalline materials using a continuum approach, Phenomenological Mesoscopic Field Dislocation Mechanics (*PMFDM*; Acharya and Roy, 2006). Specifically, this thesis contains three major parts. The first part involves the modeling of some aspects of dislocation sources that represent the emission of dislocation dipoles. The developed strategy is then used to investigate the dependence of mechanical response on the external dimensions of idealized single crystalline cubical samples with varying source and initial excess dislocation density distribution. The second part involves the modeling of plastic flow through grain boundaries in polycrystalline materials. The model is then used to analyze dislocation microstructure development in polycrystalline thin films and its effect on the mechanical response. The effect of thickness and the presence/absence of surface passivation on the plastic deformation of thin films is also studied. Results from these simulations are found to be in good *qualitative* agreement with experimental observations. The last part involves the numerical implementation of finite deformation *PMFDM* theory. The developed computational tool is capable of analyzing the deformation of crystalline materials under geometric and material nonlinearity.

Dedicated to

my father

Mr. Sushil Kumar Puri

ACKNOWLEDGEMENTS

I want to express my sincere appreciation to all the individuals who helped me during the course of my studies. My deepest thanks go to my family and friends for their constant support and encouragement.

I would like to thank my advisor, Prof. Amit Acharya, for providing me the opportunity to work on challenging problems. I would especially like to thank him for teaching me debugging of codes in addition to dislocation mechanics. It was really an honor working with him.

I would also like to thank the members of my committee, Dr. Craig Maloney (Civil & Environmental Engineering), Dr. Kaushik Dayal (Civil & Environmental Engineering), Prof. Anthony Rollett (Materials Science and Engineering), Prof. Robert M. Suter (Department of Physics) and Prof. Armand Beaudoin (Mechanical Science and Engineering, University of Illinois at Urbana-Champaign) for providing constructive feedback and suggestions. Special thanks to Prof. Armand Beaudoin and Satya Varadhan for helping me in the parallelization of code. Continuous support and help provided by Anish Roy right from the beginning of this degree is gratefully acknowledged. A special thanks to my colleagues, especially, Mudasar Zahoor and Rajarshi Singh, for reviewing my presentations from time to time. I am grateful to the administrative staff at Civil and Environmental Engineering, especially, Maxine Leffard, for helping me over the last four years.

I am grateful to my undergraduate advisor, Prof. T. N. Singh (Indian Institute of Technology, Bombay, India), for his constant inspiration and support. I thank Amit Pandey (John Hopkins University) for technical discussions about various experimental techniques from time to time.

Financial Support for this work from the National Science Foundation (Grant number: DMI-0423304) and the Dowd-ICES Fellowship is gratefully acknowledged.

TABLE OF CONTENTS

ABSTRACT	ii
ACKNOWLEDGEMENTS	iv
LIST OF FIGURES	viii
LIST OF TABLES	xii
LIST OF NOTATIONS	xiii
OVERVIEW	1
1.1 MOTIVATION	1
1.2 LITERATURE REVIEW: THEORETICAL MODELS	3
1.3 CURRENT WORK (OUTLINE)	5
1.4 NOTATION AND TERMINOLOGY	7
SMALL DEFORMATION FIELD DISLOCATION MECHANICS THEORY	9
2.1 THEORY	9
2.2 CONSTITUTIVE RESPONSE BASED ON THERMODYNAMICS	14
2.3 CONSTITUTIVE SPECIFICATION	21
2.4 NUMERICAL FORMULATION	25
2.5 ALGORITHM	28
2.6 PARALLELIZATION OF THE CODE	28
MODELING DISLOCATION SOURCES AND SIZE EFFECTS AT INITIAL	
YIELD IN CONTINUUM PLASTICITY	32
3.1 RESULTS AND DISCUSSION	33
3.2 CONCLUSIONS	44
GRAIN BOUNDARIES IN CONTINUUM PLASTICITY MODEL	55
4.1 SOLVING FOR $\bar{\zeta}$	56
4.2 JUMP CONDITION FOR EXCESS DISLOCATION DENSITY (ED)	57

4.3	NUMERICAL IMPLEMENTATION	59
4.4	TEST CASE: DEFORMATION OF A BICRYSTAL	60
4.5	CONCLUSIONS.....	65
PLASTIC DEFORMATION OF MULTICRYSTALLINE THIN FILMS		72
5.1	PROBLEM SETUP	73
5.2	RESULTS AND DISCUSSIONS	76
5.2.1	<i>Effect of Passivation</i>	76
5.2.2	<i>Effect of Thickness (Size Effect)</i>	79
5.2.3	<i>Effect of Grain Boundary Constraints</i>	81
5.3	CONCLUSIONS.....	84
FINITE DEFORMATION FIELD DISLOCATION MECHANICS		99
6.1	THEORY	99
6.2	CONSTITUTIVE SPECIFICATION.....	102
6.3	NUMERICAL FORMULATION	104
6.4	ALGORITHM.....	107
CONCLUSIONS		114
REFERENCES.....		117

LIST OF FIGURES

Chapter 2

Figure 2.1. Curve showing the performance of small deformation <i>PMFDM</i> code implemented in FORTRAN (t is the total run time).....	31
---	----

Chapter 3

Figure 3.1. Schematic layout of a typical model geometry.	46
Figure 3.2. (a) Physical representation of a Frank Read source; (b) Representation of a numerically simulated Frank Read Source; (c) Excess dislocation density at $\Gamma = 0.1\%$ for pattern (a).....	47
Figure 3.3. Schematic layout of position of sources (Black spots represents the dislocation sources).....	48
Figure 3.4. Size effect in simple shear with a predefined spatial distribution of dislocation sources, within a conventional plasticity framework.	49
Figure 3.5. Size effect in simple shear with a predefined source pattern with: (a) equation (2.59) used for hardening rate, (b) equation (3.5) used for hardening rate. ...	50
Figure 3.6. Variability in stress-strain response in simple shear with perturbation in boundary conditions: (a) $0.6\mu\text{m}$, (b) $3.0\mu\text{m}$ and (c) Mean response for the two sizes	51
Figure 3.7. Variability in stress-strain response with change in the source pattern.....	52
Figure 3.8. (a) Variation in average of $ \alpha $ over the whole domain with time, (b) Size effect in simple shear with a non- zero initial excess dislocation density.	53
Figure 3.9. Size effect in simple shear with a non- zero initial excess dislocation density and the new pattern as shown in the inset.	54

Chapter 4

Figure 4.1. Schematic layout of the bicrystal under consideration.....	66
Figure 4.2 (a) Mesh refinement analysis of the bicrystal with constrained grain boundary; (b) Effect of grain boundary constraints on the stress-strain response of a bicrystal with both grains of cubic orientation (g_o is the initial yield strength).....	67
Figure 4.3 Field plot of $ \alpha $ at 0.2% applied strain, (a) with constrained grain boundary; (b) with unconstrained grain boundary.....	68

Figure 4.4. Effect of misorientation between the two grains of the bicrystal on the mechanical response, (a) unconstrained grain boundary case, (b) constrained grain boundary, (c) difference between the constrained and unconstrained grain boundary. 69

Figure 4.5. Schematic layout of the bicrystal with dislocation sources localized along the grain boundary in a thin layer of width h 70

Figure 4.6. (a) Mesh refinement analysis for the case with $h = 0.05\mu m$; (b) Mesh refinement analysis for the case with $h = 0.1\mu m$; (c) Effect of h on the mechanical response. 71

Chapter 5

Figure 5.1. Schematic layout of typical model geometry (shaded portion represents the passivation layer) 86

Figure 5.2. Convergence analysis for the film passivated on both sides and grain boundaries being impenetrable to dislocations; (a) stress-strain plot; (b) stress at 1% applied strain plotted against $H (= \sqrt{h^2 + d^2})$ 87

Figure 5.3. Effect of surface passivation on the stress-strain behavior of thin films undergoing cyclic loading; (a) $h = 0.35\mu m$, conventional plasticity; (b) $h = 1.40\mu m$, conventional plasticity; (c) $h = 0.35\mu m$, unconstrained grain boundaries, *PMFDM*; (d) $h = 1.40\mu m$, unconstrained grain boundaries, *PMFDM*; (e) $h = 0.35\mu m$, constrained grain boundaries, *PMFDM*; (f) $h = 1.40\mu m$, constrained grain boundaries, *PMFDM*. (*bsp- both side passivated; nsp- no side passivated*) 88

Figure 5.4. Stress-strain behavior of thin films undergoing cyclic loading (grain boundaries are unconstrained) 89

Figure 5.5. Field plot of $|\alpha|$ at 0.6% applied strain for $h = 0.35\mu m$; (a) both side passivated and constrained grain boundary, (b) both side passivated and unconstrained grain boundary, (c) no side passivated and constrained grain boundary, (d) no side passivated and unconstrained grain boundary. Figures (a) and (b) are plotted using same contour levels; Figures (c) and (d) are plotted using same contour levels. 90

Figure 5.6. Effect of surface passivation on the stress-strain behavior of thin films for different orientation sets (For each line, bottom point represents unpassivated case and

top point represents both side passivated case; **gbc**- grain boundary constrained; **gbu**- grain boundary unconstrained) 91

Figure 5.7. Effect of subsequent cycles of loading and unloading on Bauschinger effect; (a) Orientation set 1; (b) Orientation set 2; (c) Orientation set 3; (d) Schematic for defining reverse plastic strain (ϵ_{rp}) and pre-strain (ϵ_p) (after Xiang and Vlassak, 2006) (**bsp**- both side passivated; **nsp**- no side passivated; **gbc**- grain boundary constrained; **gbu**- grain boundary unconstrained). 92

Figure 5.8. (a) Stress-strain behavior and (b) Bauschinger effect in thin films on unloading at different strain levels for $h = 0.35\mu m$; (c) Schematic for defining reverse plastic strain (ϵ_{rp}) and pre-strain (ϵ_p) (after Xiang and Vlassak, 2006) (**bsp**- both side passivated; **nsp**- no side passivated; **gbc**- grain boundary constrained; **gbu**- grain boundary unconstrained)..... 93

Figure 5.9. Effect of film thickness on the stress-strain behavior of films undergoing cyclic loading; (a) both side passivated, conventional plasticity; (b) no side passivated, conventional plasticity; (c) both side passivated, unconstrained grain boundaries, *PMFDM*; (d) no side passivated, unconstrained grain boundaries, *PMFDM*; (e) both side passivated, constrained grain boundaries, *PMFDM*; (d) no side passivated, constrained grain boundaries, *PMFDM*. 94

Figure 5.10. Field plot of $|\alpha|$ at 0.6% applied strain for both side passivated and unconstrained grain boundaries case; (a) $h = 0.35\mu m$ and (b) $h = 1.40\mu m$. X_2 -coordinate in both films is normalized by their thickness. 95

Figure 5.11. Effect of film thickness on the stress-strain behavior for different orientation sets (For each line, bottom point represents $h = 1.40\mu m$ and top point represents $h = 0.35\mu m$, except in no side passivated/grain boundary constrained case; **bsp**- both side passivated; **nsp**- no side passivated; **gbc**- grain boundary constrained; **gbu**- grain boundary unconstrained). 96

Figure 5.12. Effect of grain boundary constraints on the stress-strain behavior of films undergoing cyclic loading; (a) $h = 0.35\mu m$, both side passivated; (b) $h = 0.35\mu m$, no side passivated; (c) $h = 1.40\mu m$, both side passivated; (d) $h = 1.40\mu m$, no side passivated (**gbc**- grain boundary constrained; **gbu**- grain boundary unconstrained)... 97

Figure 5.13. Effect of grain boundary constraints on the stress-strain behavior for different orientation sets (For each line, bottom point represents grain boundary

unconstrained case and top point represents constrained case; *bsp*- both side passivated; *nsp*- no side passivated) 98

Chapter 6

Figure 6.1. Schematic showing the significance of $\tilde{\chi}$ and $\frac{\partial f}{\partial x}$ 112

Figure 6.2. Comparison of results from small and finite deformation *PMFDM* theory; (a) stress-strain curve; (b) field plot from small deformation theory; (c) field plot from finite deformation theory. 113

LIST OF TABLES

Chapter 6

Table 6.1. Solution procedure for the equations of finite deformation theory.108

LIST OF NOTATIONS

\mathbf{u}	total displacement field
\mathbf{U}^e	elastic distortion tensor (small deformation)
\mathbf{U}^p	plastic distortion tensor (small deformation)
$grad\ z$	compatible part of \mathbf{U}^p
\mathbf{z}	plastic displacement
$\boldsymbol{\chi}$	incompatible part of \mathbf{U}^e
\mathbf{C}	fourth-order tensor of linear elastic moduli
$\boldsymbol{\alpha}$	excess dislocation density tensor
\mathbf{V}	dislocation velocity vector
\mathbf{s}	dislocation nucleation rate tensor
\mathbf{T}	stress tensor
\mathbf{S}	averaged slipping distortion (slip rate)
\mathbf{L}^p	mean slip-distortion rate produced by Statistical Dislocations (SD)
\mathbf{T}'	deviatoric stress
\mathbf{d}	direction of the dislocation velocity
$\dot{\gamma}$	magnitudes of the SD slipping rate
v	magnitudes of averaged Excess Dislocation density velocity
m	rate-sensitivity of the material
g	strength of the material
$\dot{\gamma}_0$	reference strain rate
μ	shear modulus
b	Burgers vector magnitude
\mathbf{m}_0^κ	unstretched unit slip direction
\mathbf{n}_0^κ	unstretched unit slip normal
τ^κ	resolved shear stress on slip system κ
Ω^κ	back stress corresponding to individual slip systems κ
L	hardening coefficient (in back stress evolution rate)
c	recovery coefficient (in back stress evolution rate)
n_{slip}	total number of slip systems
k_0	a material parameter
η	a material parameter
g_s	saturation stress
θ_0	Stage II hardening rate
g_0	initial yield stress
\mathbf{F}^e	elastic distortion tensor (finite deformation)
$\tilde{\boldsymbol{\chi}}$	incompatible part of \mathbf{F}^{e-1}
$grad\ \mathbf{f}$	compatible part of \mathbf{F}^{e-1}
\mathbf{f}	plastic position vector
\mathbf{v}	velocity field
\mathbf{L}	velocity gradient

ψ	free energy per unit mass
ρ	Density
\mathbf{m}^κ	stretched unit slip direction on the current configuration
\mathbf{n}^κ	stretched unit slip normal on the current configuration

CHAPTER 1

OVERVIEW

1.1 Motivation

Over the last few decades, crystalline materials have found increasing use in information technology, energy, medicine and other sectors. However, their behavior under critical conditions is not yet completely understood. It is a well-known experimental fact that the mechanical response of such materials shows a very strong size and microstructural dependence. Some of these observations are discussed below:

1.1.1 Size effects at initial yield: There is a considerable body of experimental evidence that demonstrates that plastic deformation in FCC and other crystalline solids is size dependent at length scales of the order of tens of microns and smaller (e.g. Fleck *et al.*, 1994; Ma and Clarke, 1995; Stolken and Evans, 1998). Research has suggested that this behavior can be either an effect of constraint imposed on dislocation motion from grain boundaries or internal interfaces or an effect of excess dislocation density resulting from similar externally imposed constraints. However, recently, experiments performed on unconstrained single crystals demonstrated strong size effects at initial yield (including a hardening phenomenon at small strains) as well (Uchic *et al.*, 2004; Dimiduk *et al.*, 2005; Greer *et al.*, 2005; Frick *et al.*, 2008).

1.1.2 Deformation of polycrystalline thin films: Experiments on metallic thin films have been done recently to study their mechanical behavior (Espinosa *et al.*, 2004; Xiang and Vlassak, 2006). In particular, it is found that for thin films with

passivation on one or more surfaces, stress-strain response gets harder on decreasing thickness. In unpassivated films, mechanical response seems to be comparatively independent of film thickness. For thin films undergoing subsequent cycles of loading and unloading, a very strong Bauschinger effect is also observed in passivated films in comparison to unpassivated films. The Bauschinger effect is also size dependent, with thinner films having a high reverse plastic strain as compared to thick films (Xiang and Vlassak, 2006).

1.1.3 Large Strain Effects: In bulk production processes like rolling or extrusion, materials are deformed up to 100% strain or more, producing significant lattice rotations. A change in microstructure is observed experimentally at large strains in comparison to that at small strains. Chang and Asaro (1981) observed the formation of coarse slip bands at small strains and macroscopic shear bands at large strains in Aluminum-Copper alloy crystals deformed in tension. In the experiments performed by Hughes and Hansen (1997) it has been observed that the microstructure changes from geometrically necessary boundaries (GNB) and incidental dislocation boundaries (IDB) observed at small-medium strains ($\epsilon_{vm} = 0.06 - 0.80$), to long lamellar boundaries (LB) at large strains.

Other than the experimental observations mentioned in above sections, Mughrabi *et al.* (1979), Ahmed *et al.* (1997), and Ahmed *et al.* (2001) observed the formation of dislocation structures in fatigue experiments (small strain). These structures, particularly the persistent slip bands, are associated with crack initiation in these materials. Given these experimental observations and applications of crystalline materials, a framework that can predict deformation mechanisms in such materials at

different spatial scales and critical conditions is needed to optimally design the devices made of them. Applications of such a framework are many. For example, it can be used to enhance the design of MEMS devices through better understanding of their reliability against fatigue and fracture. Also, design of single crystal (alloy) turbine blades for aerospace and energy production technology can be optimized. Another application would be to optimize the design of light weight auto-body panels that will not only improve fuel efficiency but will also help in reducing green house gas emissions.

1.2 Literature Review: Theoretical Models

The classical theory of plasticity has been successful in predicting some interesting experimentally observed phenomena at macroscopic scale (Asaro, 1983). It is capable of modeling permanent deformation due to plastic flow, although the hardening and plastic strain rate is specified phenomenologically. The drawbacks of classical plasticity theory are that it can neither predict experimentally observed size effects at initial yield in micron sized specimens, nor the spatial inhomogeneity in a homogeneous material under boundary conditions corresponding to homogeneous deformation. This is because dislocations are not explicitly characterized in this framework. Also, this theory cannot predict the width of localized shear bands formed during plane strain compression of metals due to the absence of an intrinsic length scale.

Strain gradient plasticity models have been successful in predicting size effects in work hardening but have limited capability of predicting microstructure (Fleck *et al.*,

1994; Acharya and Beaudoin, 2000; Gurtin, 2000, 2002, 2004; Gurtin and Anand, 2005).

There are several atomistic continuum approaches that have proven to be satisfactory but the computational expense is so high that it is impossible to study a practical problem in case of problems with large number of dislocations (Ortiz and Phillips, 1999).

Discrete dislocation plasticity models (Kubin *et al.*, 1992; van der Giessen & Needleman, 1995) have been successful in predicting some experimental observations. The drawback of this theory is that the computational expense is so high that it is impossible to study a practical problem at a reasonable strain rate. Moreover, it is not able to deal with the controlled plastic flow through grain boundaries in polycrystalline materials.

A recently proposed continuum approach, Phenomenological Mesoscopic Field Dislocation Mechanics (*PMFDM*; Acharya and Roy, 2006) has been successful in modeling some benchmark problems in plasticity at mesoscopic scale and small strains (Roy & Acharya, 2006). It is a combination of (a) field dislocation mechanics theory (Acharya 2001, 2003, 2004) – as a model for the plastic flow of polar, mobile dislocation density and long-range internal stress, and (b) gradient polycrystal plasticity which is used as a model for plastic flow of statistical dislocation distributions and strength arising from short-range interactions. The mesoscopic model has been derived from field dislocation mechanics through an elementary space-time averaging of its equations. The shortcoming of this model is that the

hardening and plastic strain rate needs to be specified phenomenologically but it allows performing simulations at reasonable strain rates.

1.3 Current Work (Outline)

This thesis involves the modeling and understanding of some aspects of deformation of crystalline materials using *PMFDM* theory. The governing equations, boundary and initial conditions of the small deformation *PMFDM* theory are briefly explained in Chapter 2 followed by the spatio-temporal discretization of the equations.

Specifically, the current work involves three major parts:

- (a) Developing a continuum representation of the appearance of dislocation dipoles that accompany the operation of dislocation sources. This is explained in Chapter 3. The developed algorithm is then used to model size effects at initial yield (prior to Stage II) of idealized single crystal micron-sized specimens. Two different aspects are considered: i) specification of a density of dislocation sources that represent the development of dislocation dipoles, and ii) the presence of an initial, spatially inhomogeneous excess dislocation (ED) content. Discreteness of the source distribution appears to lead to a stochastic response in stress-strain curves, with the stochasticity diminishing as the number of sources increases. Variability in stress-strain response due to variations of source distribution is also shown. These size effects at initial yield are inferred to be due to physical length scales in dislocation mobility and the discrete description of sources that induce internal-stress-related effects, and not due to length-scale effects in the mean-field strain-hardening response (as represented through a constitutive equation). The text of this

chapter is an accepted paper in Journal of Mechanics of Materials and Structures.

- (b) Modeling of controlled plastic flow through grain boundaries. This is discussed in Chapter 4. The effect of constraints on plastic flow through grain boundaries on the mechanical response and microstructure of a bicrystal is presented as a test case. Cases with dislocation sources distributed throughout the body and localized along the grain boundary are considered. It is found that impenetrable grain boundaries causes significant work hardening as compared to penetrable grain boundaries due to the accumulation of excess dislocations along them.

Next, *PMFDM* theory is used to model the deformation of multicrystalline thin films undergoing cycles of plane strain tension and compression as described in Chapter 5. The numerical experiments presented in this chapter show that surface passivation layer on thin films introduce thickness dependence of the mechanical response. However, the effect of passivation decreases in films with impenetrable grain boundaries. The orientation of individual grains of the multicrystal also has a significant effect on mechanical response. This Chapter will be submitted for publication in a journal.

- (c) Numerical implementation of the finite deformation *PMFDM* theory (Acharya, 2004; Acharya and Roy, 2006). The governing equations are presented in Chapter 6 along with a description of required initial and

boundary conditions. The numerical implementation of the theory and the constitutive specification are also presented. The developed tool is then used to study the deformation of multicrystalline thin film under plane strain tension to test the implementation.

Finally, Chapter 7 presents a summary of this thesis in addition to suggestions for future work.

1.4 Notation and Terminology

Let B be the body under consideration with boundary ∂B . The *curl* operation on B and the cross product of a second-order tensor and a vector are defined as follows: for a second-order tensor A , a vector \mathbf{v} , and a spatially constant vector field \mathbf{c} ,

$$\begin{aligned} (A \times \mathbf{v})^T \mathbf{c} &= (A^T \mathbf{c}) \times \mathbf{v} \quad \text{for all } \mathbf{c} \\ (\text{curl } A)^T \mathbf{c} &= \text{curl}(A^T \mathbf{c}) \quad \text{for all } \mathbf{c}. \end{aligned} \tag{1.1}$$

In rectangular Cartesian components,

$$\begin{aligned} (A \times \mathbf{v})_{im} &= e_{mjk} A_{ij} v_k \\ (\text{curl } A)_{im} &= e_{mjk} A_{ik,j}, \end{aligned} \tag{1.2}$$

where e_{mjk} is a component of the third-order alternating tensor \mathbf{X} and a subscript comma refers to partial differentiation.

Given a scale of resolution l , we refer to the spatial average of Nye's (1953) dislocation-density tensor over a volume l^3 around a point as the *Excess/Polar Dislocation* (ED) density tensor at that point. Nye's tensor being a tensorial quantity, the dislocations that are averaged out in this process due to cancellation in sign form a

density that we refer to as the *Statistically Distributed Dislocation* (SD) density. Thus, the difference of local value of Nye's tensor field and its spatial average (ED) is referred to as SD.

CHAPTER 2

SMALL DEFORMATION FIELD DISLOCATION MECHANICS THEORY

The governing equations, boundary conditions and initial conditions of small deformation field dislocation mechanics (*FDM/PMFDM*) theory are summarized in this chapter. Details of the theory appear in Acharya (2001), Acharya (2003) and Acharya and Roy (2006). The salient features are mentioned in Section 2.1 followed by constitutive specifications in Section 2.2. The numerical implementation of the theory using Finite Element Method is described in Roy and Acharya (2005) and Roy and Acharya (2006), and discussed briefly in Section 2.3. The algorithm is mentioned in Section 2.4. Most of Section 2.1, 2.2, 2.3 and 2.4 have appeared in references mentioned above. They are included here for this thesis to be self contained. A part of the text of Section 2.1 is from Roy *et. al* (2007). The contributions of this thesis to this part are, (1) implementation of crystal plasticity framework mentioned in Section 2.2, (2) addition of an extra boundary term in the weak formulation of excess dislocation density mentioned in Section 2.3, and (3) parallelization of the code discussed in Section 2.4.

2.1 Theory

A theory of fine-scale dislocation mechanics, Field Dislocation Mechanics (FDM), has been proposed (Acharya, 2001; 2003), building on the pioneering works of

Kroner (1981), Mura (1963), and Willis (1967). It is summarized in this section for completeness of this thesis. The (symmetric) stress tensor \mathbf{T} satisfies

$$\begin{aligned}\mathbf{T} &= \mathbf{C} : \mathbf{U}^e \\ \text{div} \mathbf{T} &= \mathbf{0}\end{aligned}\tag{2.1}$$

along with standard traction/displacement boundary conditions. \mathbf{C} is the possibly anisotropic fourth order tensor of linear elastic moduli and \mathbf{U}^e is the elastic distortion tensor defined as

$$\mathbf{U}^e = \text{grad } \mathbf{u} - \mathbf{U}^p.\tag{2.2}$$

In the above equation, \mathbf{u} is the total displacement field and \mathbf{U}^p is the plastic distortion tensor which is decomposed uniquely into compatible and incompatible parts as

$$\mathbf{U}^p = \text{grad } \mathbf{z} - \boldsymbol{\chi}.\tag{2.3}$$

where \mathbf{z} is the plastic displacement and $\boldsymbol{\chi}$ is the incompatible part of elastic distortion. Thus, the elastic distortion tensor may be rewritten as,

$$\mathbf{U}^e = \text{grad}(\mathbf{u} - \mathbf{z}) + \boldsymbol{\chi},\tag{2.4}$$

where the field $\boldsymbol{\chi}$ cannot be written as a non-trivial gradient. The incompatible part, $\boldsymbol{\chi}$, is given by

$$\begin{aligned}\text{curl } \boldsymbol{\chi} &= \boldsymbol{\alpha} \\ \text{div } \boldsymbol{\chi} &= \mathbf{0}\end{aligned}\tag{2.5}$$

where $\boldsymbol{\alpha}$ is space-time averaged excess dislocation density tensor field, \mathbf{n} is the unit normal on the boundary of the body ∂B . The vector field \mathbf{z} whose gradient represents the compatible part of $\mathbf{U}^e/\mathbf{U}^p$ obeys the relation

$$\text{div}(\text{grad } \dot{\mathbf{z}}) = \text{div}(\boldsymbol{\alpha} \times \mathbf{V})\tag{2.6}$$

where \mathbf{V} is the averaged dislocation velocity vector. Finally the temporal evolution of the excess dislocation density tensor field is prescribed as

$$\dot{\boldsymbol{\alpha}} = -\text{curl}(\boldsymbol{\alpha} \times \mathbf{V}) + \mathbf{s} \quad (2.7)$$

These equations admit well-defined initial conditions and boundary conditions that have been discussed in detail in Acharya (2003), Acharya and Roy (2006) and Roy and Acharya (2006).

To derive an averaged theory corresponding to above set of equations, a common averaging procedure utilized in the study of multiphase flows is used (e.g. Babic, 1997). For a microscopic field f given as a function of space and time, the mesoscopic space-time averaged field \bar{f} is defined as follows (Acharya and Roy, 2006):

$$\bar{f}(\mathbf{x}, t) := \frac{1}{\int_{I(t)} \int_{\Omega(\mathbf{x})} w(\mathbf{x} - \mathbf{x}', t - t') d\mathbf{x}' dt'} \int_{\mathfrak{S}} \int_B w(\mathbf{x} - \mathbf{x}', t - t') f(\mathbf{x}', t') d\mathbf{x}' dt' \quad (2.8)$$

where, B is the body, \mathfrak{S} a sufficiently large interval of time, $\Omega(\mathbf{x})$ is a bounded region within the body around the point \mathbf{x} with linear dimension of the order of the spatial resolution of the macroscopic model we seek, and $I(t)$ is a bounded interval in \mathfrak{S} containing t . The weighting function w is non-dimensional, assumed to be smooth in the variables $\mathbf{x}, \mathbf{x}', t, t'$ and, for fixed \mathbf{x} and t , have support (i.e. to be non-zero) only in $\Omega(\mathbf{x}) \times I(t)$ when viewed as a function of (\mathbf{x}', t') . Applying this

operator to the equations in , we obtain an *exact* set of equations for the averages given as

$$\begin{aligned}
\text{curl } \bar{\boldsymbol{\chi}} &= \bar{\boldsymbol{\alpha}} \\
\text{div } \bar{\boldsymbol{\chi}} &= \mathbf{0} \\
\text{div}(\text{grad } \dot{\bar{\mathbf{z}}}) &= \text{div}(\bar{\boldsymbol{\alpha}} \times \bar{\mathbf{V}} + \mathbf{L}^p) \\
\bar{\mathbf{U}}^e &= \text{grad}(\bar{\mathbf{u}} - \bar{\mathbf{z}}) + \bar{\boldsymbol{\chi}} \\
\text{div } \bar{\mathbf{T}} &= \mathbf{0}, \bar{\mathbf{T}} = \mathbf{C} : \bar{\mathbf{U}}^e \\
\dot{\bar{\boldsymbol{\alpha}}} &= -\text{curl } \mathbf{S} \\
\mathbf{S} &:= \bar{\boldsymbol{\alpha}} \times \bar{\mathbf{V}} + \mathbf{L}^p
\end{aligned} \tag{2.9}$$

where \mathbf{L}^p , defined as

$$\mathbf{L}^p(\mathbf{x}, t) := \overline{(\boldsymbol{\alpha} - \bar{\boldsymbol{\alpha}}) \times \mathbf{V}}(\mathbf{x}, t) = \overline{\boldsymbol{\alpha} \times \mathbf{V}}(\mathbf{x}, t) - \bar{\boldsymbol{\alpha}}(\mathbf{x}, t) \times \bar{\mathbf{V}}(\mathbf{x}, t), \tag{2.10}$$

\mathbf{S} is the averaged slipping distortion (slip rate), $\bar{\mathbf{V}}$ is the averaged excess dislocation velocity vector, and \mathbf{L}^p , represents that part of the total slip strain rate which is not represented by the slipping produced by the averaged signed dislocation density. \mathbf{L}^p and $\bar{\mathbf{V}}$ require constitutive specifications.

From here onwards in Section 2.1, fields without overhead bars refer to averaged fields.

2.1.1 Boundary Conditions: The following boundary conditions are admitted:

$$\begin{aligned}
\boldsymbol{\chi} \mathbf{n} &= \mathbf{0} \text{ on the boundary } \partial B \text{ of the body with outward unit normal } \mathbf{n}, \\
(\text{grad } \dot{\mathbf{z}}) \mathbf{n} &= (\boldsymbol{\alpha} \times \mathbf{V} + \mathbf{L}^p) \mathbf{n} \text{ on } \partial B,
\end{aligned} \tag{2.11}$$

Standard displacement/traction boundary conditions on ∂B .

Other than the above conditions, equation (2.9)₆ admits boundary conditions on the dislocation flow (Acharya and Roy, 2006). In general, a natural boundary condition of the form

$$\mathbf{S} \times \mathbf{n} = \Phi, \quad (2.12)$$

where, Φ is a (second-order tensor valued) specified function of time and position along the boundary satisfying the constraint $\Phi \mathbf{n} = \mathbf{0}$ is appropriate to model controlled flow at the boundary. A rigid boundary with respect to slipping may be represented with a zero flow boundary condition

$$\mathbf{S} \times \mathbf{n} = \mathbf{0} \quad (2.13)$$

on the entire boundary. Imposing such a boundary condition can lead to the development of shocks or discontinuities. A less restrictive boundary condition is the imposition of the dislocation flux, $\alpha(\mathbf{V} \cdot \mathbf{n})$, on inflow points of the boundary (where $\mathbf{V} \cdot \mathbf{n} < 0$), along with a specification of $\mathbf{L}^p \times \mathbf{n}$ on the entire boundary. This condition allows free exit of dislocations without any added specification.

2.1.2 Initial Conditions: The field equations mentioned above admits initial conditions on the fields \mathbf{u} , α and $grad z$ which are as follows. For the \mathbf{u} field we assume $\mathbf{u}|_{t=0} \equiv \mathbf{0}$, which is a physically natural initial condition on the displacement field. Unless otherwise mentioned, we assume that the body is initially excess dislocation free which translates to $\alpha|_{t=0} \equiv \mathbf{0}$. Initial

condition on the $grad \mathbf{z}$ field is obtained from solving (2.9)₁₋₂ and (2.9)₄₋₅,
with $\mathbf{u}|_{t=0} \equiv \mathbf{0}$.

2.1.3 Auxiliary Condition: The value of $\dot{\mathbf{z}}$ is prescribed at an arbitrarily chosen point of the body and in our case is assumed to vanish without loss of generality.

2.2 Constitutive Response based on Thermodynamics

This Section involves the derivation of the general form of constitutive equations for dislocation velocity, \mathbf{V} and the mean slip-distortion rate produced by SD, \mathbf{L}^p .

The internal energy e , in the body can be written as a sum of Helmholtz free energy per unit mass W and entropy per unit mass function η .

$$e(\mathbf{U}^e, \theta) = W(\mathbf{U}^e, \theta) + \eta(\mathbf{U}^e, \theta)\theta \quad (2.14)$$

where, θ is absolute temperature and \mathbf{U}^e is the elastic distortion.

From the Clausius Duhem inequality,

$$\int_V \rho \dot{\eta} dv \geq - \int_{\partial V} \frac{\mathbf{q}}{\theta} \cdot \mathbf{n} da + \int_V \frac{r}{\theta} dv \quad (2.15)$$

for all material volumes V , where \mathbf{q} is the heat flux vector defined by $\mathbf{q} \cdot \mathbf{n}$ being the heat flux out of the body through a boundary point with outward unit normal \mathbf{n} , and r is the heat supply.

Using divergence theorem, (2.15) results in

$$\int_V \rho \dot{\eta} dv \geq - \int_V \frac{\text{div } \mathbf{q}}{\theta} dv + \int_V \frac{\mathbf{q} \cdot \text{grad } \theta}{\theta^2} dv + \int_V \frac{r}{\theta} dv \quad (2.16)$$

From balance of energy,

$$\begin{aligned} \frac{d}{dt} \int_V \rho e dv + \frac{d}{dt} \int_V \frac{1}{2} \rho \mathbf{v} \cdot \mathbf{v} dv = \\ \int_{\partial V} \mathbf{T} \mathbf{n} \cdot \mathbf{v} da + \int_V \mathbf{b} \cdot \mathbf{v} dv - \int_{\partial V} \mathbf{q} \cdot \mathbf{n} da + \int_V r dv \end{aligned} \quad (2.17)$$

Using conservation of linear momentum (with inertia), equation (2.17) can be written as,

$$\frac{d}{dt} \int_V \rho e dv = \int_V \mathbf{T} : \dot{\boldsymbol{\varepsilon}} dv - \int_{\partial V} \mathbf{q} \cdot \mathbf{n} da + \int_V r dv \quad (2.18)$$

Eliminating r from (2.16) using (2.18),

$$\int_V \rho \theta \dot{\eta} dv - \int_V \frac{\mathbf{q} \cdot \text{grad } \theta}{\theta} dv - \int_V \rho \dot{e} dv + \int_V \mathbf{T} : \dot{\boldsymbol{\varepsilon}} dv \geq 0 \quad (2.19)$$

From equation (2.14) and (2.19),

$$\int_V \rho \theta \dot{\eta} dv - \int_V \frac{\mathbf{q} \cdot \text{grad } \theta}{\theta} dv - \int_V \rho (\dot{W} + \dot{\eta} \theta + \eta \dot{\theta}) dv + \int_V \mathbf{T} : \dot{\boldsymbol{\varepsilon}} dv \geq 0 \quad (2.20)$$

$$\int_V \left(- \frac{\mathbf{q} \cdot \text{grad } \theta}{\theta} - \rho (\dot{W} + \eta \dot{\theta}) + \mathbf{T} : \dot{\boldsymbol{\varepsilon}} \right) dv \geq 0 \quad (2.21)$$

$$\int_V \left(- \frac{\mathbf{q} \cdot \text{grad } \theta}{\theta} - \rho \left(\frac{\partial W}{\partial \mathbf{U}^e} : \dot{\mathbf{U}}^e + \frac{\partial W}{\partial \theta} \dot{\theta} + \eta \dot{\theta} \right) + \mathbf{T} : \dot{\boldsymbol{\varepsilon}} \right) dv \geq 0 \quad (2.22)$$

$$\int_V \left(- \frac{\mathbf{q} \cdot \text{grad } \theta}{\theta} - \rho \left(\frac{\partial W}{\partial \mathbf{U}^e} : (\dot{\boldsymbol{\varepsilon}} - \dot{\mathbf{U}}^p) + \frac{\partial W}{\partial \theta} \dot{\theta} + \eta \dot{\theta} \right) + \mathbf{T} : \dot{\boldsymbol{\varepsilon}} \right) dv \geq 0 \quad (2.23)$$

$$\int_V \left(\left(\mathbf{T} - \rho \frac{\partial W}{\partial \mathbf{U}^e} \right) : \dot{\boldsymbol{\varepsilon}} - \frac{\mathbf{q} \cdot \text{grad } \theta}{\theta} - \rho \left(\frac{\partial W}{\partial \theta} + \eta \right) \dot{\theta} + \rho \frac{\partial W}{\partial \mathbf{U}^e} \dot{\mathbf{U}}^p \right) dv \geq 0 \quad (2.24)$$

Assuming standard thermoelastic constitutive equations,

$$\begin{aligned} \mathbf{T} &= \rho \frac{\partial W}{\partial \mathbf{U}^e} \\ \eta &= -\frac{\partial W}{\partial \theta} \end{aligned} \quad (2.25)$$

Satisfaction of the second law of thermodynamics requires,

$$\int_V \left(-\frac{\mathbf{q} \cdot \text{grad } \theta}{\theta} + \rho \frac{\partial W}{\partial \mathbf{U}^e} : \dot{\mathbf{U}}^p \right) dv \geq 0 \quad (2.26)$$

Assuming Fourier's law for the heat flux vector \mathbf{q} ,

$$\mathbf{q} = -k \text{ grad } \theta; \quad k \geq 0 \quad (2.27)$$

Thus, equation (2.25)₃ reduces to

$$\int_V \left(\rho \frac{\partial W}{\partial \mathbf{U}^e} : \dot{\mathbf{U}}^p \right) dv \geq 0 \quad (2.28)$$

From equation (2.25)₁ and (2.28),

$$\int_V (\mathbf{T} : \dot{\mathbf{U}}^p) dv \geq 0 \quad (2.29)$$

Using equation (2.3),

$$\int_V (\mathbf{T} : (\nabla \dot{\mathbf{z}} - \dot{\boldsymbol{\chi}})) dv \geq 0 \quad (2.30)$$

Given a sufficiently smooth \mathbf{T} field there exists a unique tensor field \mathbf{W} satisfying (Acharya *et. al*, 2008),

$$\begin{aligned} \text{div } \mathbf{W} &= \mathbf{0} \text{ on } B \\ \mathbf{W} \times \mathbf{n} &= \mathbf{0} \text{ on } \partial B \end{aligned} \quad (2.31)$$

and a unique tensor field $\text{grad } \mathbf{g}$ satisfying,

$$(\text{grad } \mathbf{g} - \mathbf{T})\mathbf{n} = \mathbf{0} \text{ on } \partial B \quad (2.32)$$

such that

$$\begin{aligned} \mathbf{T} &= \text{curl } \mathbf{W} + \text{grad } \mathbf{g} \quad \text{and} \\ \int_B \text{grad } \mathbf{g} : \text{curl } \mathbf{W} dv &= 0 \end{aligned} \quad (2.33)$$

Using (2.33) and (2.30),

$$\int_V ((\text{curl } \mathbf{W} + \text{grad } \mathbf{g}) : (\nabla \dot{\mathbf{z}} - \dot{\boldsymbol{\chi}})) dv \geq 0 \quad (2.34)$$

$$\int_V (\text{curl } \mathbf{W} : \nabla \dot{\mathbf{z}} - \text{curl } \mathbf{W} : \dot{\boldsymbol{\chi}} + \text{grad } \mathbf{g} : \nabla \dot{\mathbf{z}} - \text{grad } \mathbf{g} : \dot{\boldsymbol{\chi}}) dv \geq 0 \quad (2.35)$$

Evaluating the first term of equation (2.35),

$$\begin{aligned} \int_V (\text{curl } \mathbf{W} : \nabla \dot{\mathbf{z}}) dv &= \int_V (e_{kjm} W_{ij,k} \dot{z}_{i,m}) dv \\ &= \int_V (e_{kjm} W_{ij,k} \dot{z}_i)_{,m} dv - \int_V (e_{kjm} W_{ij,km} \dot{z}_i) dv \\ &= \int_{\partial V} (e_{kjm} W_{ij,k} \dot{z}_i n_m) da - \int_V (e_{kjm} W_{ij,km} \dot{z}_i) dv \\ &= \int_{\partial V} (\text{curl } \mathbf{W}) \mathbf{n} \cdot \dot{\mathbf{z}} da - \int_V \text{div}(\text{curl } \mathbf{W}) \cdot \dot{\mathbf{z}} dv \\ &= \int_{\partial V} (\mathbf{T} - \text{grad } \mathbf{g}) \mathbf{n} \cdot \dot{\mathbf{z}} da - \int_V \text{div}(\text{curl } \mathbf{W}) \cdot \dot{\mathbf{z}} dv \end{aligned} \quad (2.36)$$

Using (2.32),

$$\int_V (\text{curl } \mathbf{W} : \nabla \dot{\mathbf{z}}) dv = 0 \quad (2.37)$$

Evaluating the second term of equation (2.35),

$$\begin{aligned}
\int_V (\mathit{curl} \mathbf{W} : \dot{\boldsymbol{\chi}}) dv &= \int_V (e_{kjm} W_{ij,k} \dot{\chi}_{im}) dv \\
&= \int_V (e_{kjm} W_{ij} \dot{\chi}_{im})_{,k} dv - \int_V (e_{kjm} W_{ij} \dot{\chi}_{im,k}) dv \\
&= \int_{\partial V} (e_{kjm} W_{ij} \dot{\chi}_{im} n_k) da - \int_V (e_{kjm} W_{ij} \dot{\chi}_{im,k}) dv \\
&= - \int_{\partial V} (\mathbf{W} \times \mathbf{n}) : \dot{\boldsymbol{\chi}} da + \int_V (\mathit{curl} \dot{\boldsymbol{\chi}} : \mathbf{W}) dv \\
&= \int_V (\dot{\boldsymbol{\alpha}} : \mathbf{W}) dv = - \int_V (\mathit{curl} \mathbf{S} : \mathbf{W}) dv \\
&= - \int_V (e_{kjm} S_{ij,k} W_{im}) dv \\
&= - \int_V (e_{kjm} S_{ij} W_{im})_{,k} dv + \int_V (e_{kjm} S_{ij} W_{im,k}) dv \\
&= - \int_{\partial V} (e_{kjm} S_{ij} W_{im} n_k) da + \int_V (e_{kjm} S_{ij} W_{im,k}) dv \\
&= - \int_{\partial V} (\mathbf{W} \times \mathbf{n}) : \mathbf{S} da - \int_V (\mathit{curl} \mathbf{W} : \mathbf{S}) dv
\end{aligned} \tag{2.38}$$

Using (2.31)₂,

$$\int_V (\mathit{curl} \mathbf{W} : \dot{\boldsymbol{\chi}}) dv = - \int_V (\mathit{curl} \mathbf{W} : \mathbf{S}) dv \tag{2.39}$$

Evaluating the third term of equation (2.35),

$$\begin{aligned}
\int_V (\mathit{grad} \mathbf{g} : \nabla \dot{\mathbf{z}}) dv &= \int_V (g_{i,j} \dot{z}_{i,j}) dv \\
&= \int_V (g_{i,j} \dot{z}_{i,j})_{,j} dv - \int_V (g_i \dot{z}_{i,j}) dv
\end{aligned} \tag{2.40}$$

Using equation (2.9)₃,

$$\int_V (\mathit{grad} \mathbf{g} : \nabla \dot{\mathbf{z}}) dv = \int_{\partial V} (g_i \dot{z}_{i,j} n_j) da - \int_V (g_i S_{ij,j}) dv \tag{2.41}$$

Using equation (2.11)₂,

$$\begin{aligned}
\int_V (\mathit{grad} \mathbf{g} : \nabla \dot{\mathbf{z}}) dv &= \int_{\partial V} (g_i S_{ij} n_j) da - \int_V (g_i S_{ij,j}) dv \\
&= \int_V (g_i S_{ij})_{,j} dv - \int_V (g_i S_{ij,j}) dv \\
&= \int_V (g_{i,j} S_{ij}) dv \\
&= \int_V (\mathit{grad} \mathbf{g} : \mathbf{S}) dv
\end{aligned} \tag{2.42}$$

Evaluating the fourth term of equation (2.35),

$$\begin{aligned}
\int_V (\mathbf{grad} \mathbf{g} : \dot{\boldsymbol{\chi}}) dv &= \int_V (\mathbf{g}_{i,j} \dot{\chi}_{ij}) dv \\
&= \int_V (\mathbf{g}_i \dot{\chi}_{ij})_{,j} dv - \int_V (\mathbf{g}_i \dot{\chi}_{ij,j}) dv \\
&= \int_{\partial V} (\mathbf{g}_i \dot{\chi}_{ij} \mathbf{n}_j) da - \int_V (\mathbf{g}_i \dot{\chi}_{ij,j}) dv \\
&= \int_{\partial V} (\mathbf{g} \cdot \boldsymbol{\chi} \mathbf{n}) da - \int_V (\mathbf{g} \cdot \mathbf{div} \boldsymbol{\chi}) dv
\end{aligned} \tag{2.43}$$

Using equations (2.9)₂ and (2.11)₁,

$$\int_V (\mathbf{grad} \mathbf{g} : \dot{\boldsymbol{\chi}}) dv = 0 \tag{2.44}$$

Using (2.36) - (2.43), (2.35) reduces to,

$$\int_V (\mathbf{curl} \mathbf{W} : \mathbf{S}) dv + \int_V (\mathbf{grad} \mathbf{g} : \mathbf{S}) dv \geq 0 \tag{2.45}$$

Using equation (2.33)₁,

$$\int_V (\mathbf{T} : \mathbf{S}) dv \geq 0 \tag{2.46}$$

Using equation (2.9)₇,

$$\int_V (\mathbf{T} : \boldsymbol{\alpha} \times \mathbf{V} + \mathbf{T} : \mathbf{L}^p) dv \geq 0 \tag{2.47}$$

$$\int_V (X(\mathbf{T}\boldsymbol{\alpha}) \mathbf{V} + \mathbf{T} : \mathbf{L}^p) dv \geq 0 \tag{2.48}$$

where, $X(\mathbf{T}\boldsymbol{\alpha}) = e_{ijk} T_{jr} \alpha_{rk}$

Equation (2.48) indicates that the driving forces for dislocation velocity and slip due to SD are $X(\mathbf{T}\boldsymbol{\alpha})$ and \mathbf{T} , respectively.

$$\begin{aligned} V &\rightarrow X(\mathbf{T}\boldsymbol{\alpha}) \\ L^p &\rightarrow \mathbf{T} \end{aligned} \quad (2.49)$$

Next, we substitute the above mentioned constitutive assumptions in the balance of energy (2.18) (assuming $r = 0$ for simplicity),

$$\begin{aligned} \int_V \left(\rho \frac{\partial W}{\partial U^e} : (\dot{\boldsymbol{\varepsilon}} - \dot{\mathbf{U}}^p) + \rho \frac{\partial W}{\partial \theta} \dot{\theta} - \rho \frac{\partial W}{\partial \theta} \dot{\theta} - \theta \frac{\partial \mathbf{T}}{\partial \theta} : \dot{\mathbf{U}}^e - \rho \theta \frac{\partial^2 W}{\partial \theta^2} \dot{\theta} \right) dv \\ = \int_V \rho \frac{\partial W}{\partial U^e} : \dot{\boldsymbol{\varepsilon}} dv - \int_{\partial V} k \text{grad } \theta \cdot \mathbf{n} da \end{aligned} \quad (2.50)$$

This implies that,

$$-\rho \theta \frac{\partial^2 W}{\partial \theta^2} \dot{\theta} = -\text{div}(k \text{grad } \theta) + \theta \frac{\partial \mathbf{T}}{\partial \theta} : \dot{\mathbf{U}}^e + \mathbf{T} : \dot{\mathbf{U}}^p \quad (2.51)$$

$$\rho c \dot{\theta} = -\text{div}(k \text{grad } \theta) + \theta \frac{\partial \mathbf{T}}{\partial \theta} : \dot{\mathbf{U}}^e + \mathbf{T} : \dot{\mathbf{U}}^p \quad (2.52)$$

where, $c := -\theta \frac{\partial^2 W}{\partial \theta^2}$ specific heat capacity at constant volume.

In case of an adiabatic process, equation (2.52) reduces to,

$$\rho c \dot{\theta} = \theta \frac{\partial \mathbf{T}}{\partial \theta} : \dot{\mathbf{U}}^e + \mathbf{T} : \dot{\mathbf{U}}^p \quad (2.53)$$

Thus, in an adiabatic process, plastic work is utilized in raising the temperature of the body. In case of an isothermal process, equation (2.52) reduces to,

$$-\text{div}(k \text{grad } \theta) + \theta \frac{\partial \mathbf{T}}{\partial \theta} : \dot{\mathbf{U}}^e = \mathbf{T} : \dot{\mathbf{U}}^p \quad (2.54)$$

If k is assumed to be constant and scalar, then equation (2.54) reduces to the Poisson's equation.

2.3 Constitutive Specification

Physically reasonable choices for the mean (i.e. space-time average) of signed velocity of dislocation segments (that may be associated with the velocity of mean ED), \mathbf{V} , and the mean slip-distortion rate produced by SD, \mathbf{L}^p , are made based on the requirement of non-negativity of plastic working and ingredients of conventional plasticity theory. The constitutive specifications for a natural extension of J2 and crystal plasticity are mentioned below:

J2 Plasticity: Simple choices motivated by *J2* plasticity and the thermodynamics of PMFDM (Acharya and Roy, 2006) are,

$$\begin{aligned} \mathbf{L}^p &= \dot{\gamma} \frac{\mathbf{T}'}{|\mathbf{T}'|} \quad ; \quad \dot{\gamma} \geq 0, \\ \mathbf{V} &= v \frac{\mathbf{d}}{|\mathbf{d}|} \quad ; \quad v \geq 0, \end{aligned} \tag{2.55}$$

where, \mathbf{T}' is the stress deviator, \mathbf{d} is the direction of the dislocation velocity, $\dot{\gamma}$ and v are non-negative functions of state representing the magnitudes of the SD slipping rate and the averaged ED velocity, respectively. The direction of the dislocation velocity is defined by

$$\begin{aligned} \mathbf{d} &:= \mathbf{b} - \left(\mathbf{b} \cdot \frac{\mathbf{a}}{|\mathbf{a}|} \right) \frac{\mathbf{a}}{|\mathbf{a}|}, \\ \mathbf{b} &:= \mathbf{X}(\mathbf{T}'\boldsymbol{\alpha}) \quad ; \quad b_i = e_{ijk} T'_{jr} \alpha_{rk} \quad ; \quad \mathbf{a} := \mathbf{X}(\text{tr}(\mathbf{T})\boldsymbol{\alpha}) \quad ; \quad a_i = \left(\frac{1}{3} T_{mm} \right) e_{ijk} \alpha_{jk}. \end{aligned} \tag{2.56}$$

Thermodynamics indicates \mathbf{b} as the driving force for \mathbf{V} ; the definition of \mathbf{d} is to ensure pressure independence of plastic straining in the model. We choose a power law relation for $\dot{\gamma}$ as

$$\dot{\gamma} = \dot{\gamma}_0 \left(\frac{|\mathbf{T}'|}{\sqrt{2g}} \right)^{\frac{1}{m}}, \quad (2.57)$$

where, m is the rate-sensitivity of the material, g is the strength of the material, and $\dot{\gamma}_0$ is a reference strain rate. The expression for v is assumed to be

$$v(state) = \eta^2 b \left(\frac{\mu}{g} \right)^2 \dot{\gamma}(\mathbf{T}', g), \quad (2.58)$$

where μ is the shear modulus, b the Burgers vector magnitude and $\eta = 1/3$ a material parameter.

The strength of the material is assumed to evolve according to

$$\dot{g} = \left[\frac{\eta^2 \mu^2 b}{2(g - g_0)} k_0 |\boldsymbol{\alpha}| + \theta_0 \left(\frac{g_s - g}{g_s - g_0} \right) \right] \{ |\boldsymbol{\alpha} \times \mathbf{V}| + \dot{\gamma} \}, \quad (2.59)$$

where g_s is the saturation stress, g_0 is the yield stress, and θ_0 is the Stage II hardening rate. The material parameters $g_s, g_0, \mu, b, \dot{\gamma}_0, m$ are known from conventional plasticity (Voce Law and power-law hardening). Consequently, k_0 is the only extra parameter that needs to be fitted and can be obtained from experimental grain-size dependence of flow stress results, as shown in Acharya and Beaudoin (2000) and Beaudoin et al. (2000).

Crystal Plasticity: The corresponding equations for crystal plasticity are mentioned below.

$$\begin{aligned}
\mathbf{L}^p &= \sum_{\kappa} \dot{\gamma}^{\kappa} \mathbf{m}_0^{\kappa} \otimes \mathbf{n}_0^{\kappa} \\
\mathbf{V} &= v \frac{\mathbf{d}}{|\mathbf{d}|} ; v \geq 0
\end{aligned} \tag{2.60}$$

where, \mathbf{m}_0^{κ} and \mathbf{n}_0^{κ} are the unstretched unit slip direction and normal, respectively, \mathbf{d} is the direction of the dislocation velocity, $\dot{\gamma}^{\kappa}$ represents the magnitudes of SD slipping rate on the slip system κ and v is the averaged ED velocity.

The current framework involves an accurate calculation of stresses corresponding to the averaged excess dislocation density $\bar{\alpha}$. However, it stands to reason that averaged kinetics of plastic deformation depends on the stress field of the fluctuation $\boldsymbol{\alpha} - \bar{\boldsymbol{\alpha}}$ (described in Section 2.1), especially, at small scales, as can be seen from the definition of \mathbf{L}^p and \mathbf{V} (described in Section 2.1). It is to model this contribution that a phenomenological back stress tensor $\boldsymbol{\Omega}$, is introduced in the expression for $\dot{\gamma}^{\kappa}$ (power law relation),

$$\dot{\gamma}^{\kappa} = \dot{\gamma}_0^{\kappa} \text{sgn}(\tau^{\kappa} - \Omega^{\kappa}) \left(\frac{|\tau^{\kappa} - \Omega^{\kappa}|}{g} \right)^{\frac{1}{m}} \tag{2.61}$$

where, τ^{κ} is the resolved shear stress on slip system κ , Ω^{κ} is the back stress corresponding to individual slip systems κ , m is the rate-sensitivity of the material, g is the strength of the material, and $\dot{\gamma}_0^{\kappa}$ is a reference strain rate on the slip system κ . The expression of back stress evolution is based on the Armstrong–Frederick (1966) form and is a function of excess dislocation density (ED).

$$\dot{\Omega}^\kappa = \left(|\boldsymbol{\alpha} \mathbf{m}_0^\kappa| + |\boldsymbol{\alpha} \mathbf{p}_0^\kappa| \right) L \mu \dot{\gamma}^\kappa - c \Omega^\kappa |\dot{\gamma}^\kappa|; \mathbf{p}_0^\kappa = \mathbf{m}_0^\kappa \times \mathbf{n}_0^\kappa \quad (2.62)$$

where, L is the hardening coefficient and c is the recovery coefficient. Back stress evolves only if there is a non-zero excess dislocation content in the body. Each back stress component is considered independent of other slip systems. The expression for back stress evolution (2.62), is currently phenomenological. Recovery has a very significant effect on the mechanical response and microstructure evolution in crystalline materials. It needs to be specified based on the accurate coarse graining of the very nonlinear underlying set of equations representing the motion of individual dislocations, represented either discretely or by PDE- clearly a formidable theoretical challenge, thus making the case for good phenomenological descriptions even more compelling.

The resolved shear stress τ^κ is calculated as follows:

$$\tau^\kappa = \mathbf{m}_0^\kappa \cdot \mathbf{T} \mathbf{n}_0^\kappa \quad (2.63)$$

The direction of dislocation velocity, \mathbf{d} is same as mentioned above for $J2$ plasticity,

$$\mathbf{d} := \mathbf{b} - \left(\mathbf{b} \cdot \frac{\mathbf{a}}{|\mathbf{a}|} \right) \frac{\mathbf{a}}{|\mathbf{a}|}, \quad (2.64)$$

$$\mathbf{b} := \mathbf{X}(\mathbf{T}' \boldsymbol{\alpha}) ; b_i = e_{ijk} T'_{jr} \alpha_{rk} ; \quad \mathbf{a} := \mathbf{X}(\text{tr}(\mathbf{T}) \boldsymbol{\alpha}) ; a_i = \left(\frac{1}{3} T_{mm} \right) e_{ijk} \alpha_{jk}.$$

The expression for v is assumed to be

$$v(\text{state}) = \frac{\eta^2 b}{n_{slip}} \left(\frac{\mu}{g} \right)^2 \sum_{\kappa} \dot{\gamma}^\kappa \quad (2.65)$$

where μ is the shear modulus, b the Burgers vector magnitude, n_{slip} is the total number of slip systems and $\eta = 1/3$ a material parameter.

The strength of the material is assumed to evolve according to

$$\dot{g} = \left[\frac{\eta^2 \mu^2 b}{2(g - g_0)} k_0 |\alpha n_0^\kappa| + \theta_0 \left(\frac{g_s - g}{g_s - g_0} \right) \right] \left\{ |\alpha \times V| + \sum_\kappa \dot{\gamma}^\kappa \right\} \quad (2.66)$$

where g_s is the saturation stress, g_0 is the yield stress, and θ_0 is the Stage II hardening rate.

2.4 Numerical Formulation

The solution algorithm and details of the spatio-temporal discretization of the equations for the *mesoscopic* theory are explained in this section. The symbol $\delta(\cdot)$ represents a variation (or test function) associated with the field (\cdot) in a suitable class of functions. $\delta(\cdot)$ is arbitrary up to satisfying any prescribed essential boundary conditions for the field (\cdot) . An increment of time $[t, t + \Delta t]$ is considered, and fields without any superscripts refer to values at $t + \Delta t$ and those with the superscript t refer to values at time t . All spatial fields are discretized by first-order, 8-node (three-dimensional), isoparametric brick elements.

All the spatial derivatives in this section are taken with respect to the reference configuration. The equation for the evolution of dislocation density, (2.9)₆, is considered first. A combination of the Galerkin Method and the Least Squares Finite Element Method (LSFEM), the so-called Galerkin Least Squares Method (GLS)

(Hughes *et al.*, 1989) is used for its FE discretization. The discretized equation for (2.9)₆ in components with respect to an orthonormal basis is as follows:

$$\begin{aligned}
& \int_B \delta\alpha_{ij} (\alpha_{ij} - \alpha'_{ij}) dv - \Delta t \int_B [\delta\alpha_{ij,k} \alpha_{ij} V'_k - \delta\alpha_{ij,k} \alpha_{ik} V'_j] dv \\
& - \Delta t \int_B \delta\alpha_{ij} s^t_{ij} dv + \Delta t \int_{\partial B_i} \delta\alpha_{ij} F_{ij} da \\
& + \Delta t \int_{\partial B_o} \delta\alpha_{ij} \alpha'_{ij} (V'_k n_k) da - \Delta t \int_{\partial B} \delta\alpha_{ij} \alpha'_{ik} n_k V'_j da \\
& - \Delta t \int_B \delta\alpha_{ij,k} e_{jkl} L^p_{il} dv + \Delta t \int_{\partial B} \delta\alpha_{ij} e_{jkl} L^p_{il} n_k da \\
& + \int_{B_{\text{interiors}}} A_{ri} (\delta\alpha_{ri} + \Delta t [\delta\alpha_{ri,j} V'_j + \delta\alpha_{ri} V'_{j,j} - \delta\alpha_{rj,j} V'_i - \delta\alpha_{rj} V'_{i,j}]) dv \\
& + \Delta t \int_{\partial B_i} \delta\alpha_{ij} (F_{ij} - \alpha'_{ij} (V'_k n_k)) da = 0
\end{aligned} \tag{2.67}$$

where

$$A_{ri} = \alpha_{ri} - \alpha'_{ri} + \Delta t [\alpha'_{ri,j} V'_j + \alpha'_{ri} V'_{j,j} - \alpha'_{rj,j} V'_i - \alpha'_{rj} V'_{i,j} - s^t_{ri} + e_{ijk} L^p_{rk,j}], \tag{2.68}$$

\mathbf{F} is the prescribed flux on the inflow boundary (∂B_i), ∂B_o is the set of outflow/neutral points of the boundary where $\mathbf{V} \cdot \mathbf{n} \geq 0$ and $B_{\text{interiors}}$ refers to the union of the element interiors. The setting of surface terms to zero in the above expression results in a no-flow boundary condition. The underlined term in (2.67) is an additional term that enters the discretization for excess dislocation-density evolution over those described in Roy and Acharya (2006). This new formulation with an extra term corresponding to the LSFEM discretization of the inflow boundary condition on α was used in Puri *et al.* (2009) following Varadhan *et.al* (2006). The scheme is consistent even without the addition of this term; numerical experiments show a better imposition of inflow boundary conditions with its inclusion.

LSFEM is used for the discretization of equations (2.9)₁₋₂,

$$\int_B e_{ijk} \delta \chi_{rk,j} [e_{imn} \chi_{rn,m} - \alpha_{ri}] dv + \int_B \delta \chi_{ij,j} \chi_{im,m} dv = 0. \quad (2.69)$$

The essential boundary condition (2.11)₁ needs to be imposed and requires, in certain circumstances, the use of linear constraint equations.

Standard Galerkin method is used for the discretization of (2.9)₃ and (2.9)₅. The discretized form of (2.9)₃ is,

$$\int_B \delta z_{i,j} [z_{i,j} - z_{i,j}^t - \Delta t (L_{ij}^p + e_{jmk} \alpha_{im}^t V_k^t)] dv = 0 \quad (2.70)$$

specify $z_i = 0$ at an arbitrarily chosen point.

Next, the discretized form of equilibrium equation (2.9)₅ is,

$$T_{ij} = C_{ijkl} (u_{i,j} - z_{k,l} + \chi_{kl})$$

$$\int_B \delta u_{i,j} T_{ij} dv - \int_{\partial B_i} \delta u_i t_i da = 0 \quad (2.71)$$

and standard displacement b.c.s.

In (2.71), ∂B_i represents the set of points on the boundary on which tractions are specified.

2.5 Algorithm

A problem is typically solved in steps. The first step solves the problem of internal stress due to the presence of a prescribed initial excess dislocation density in the body, and defines the initial condition for slip distortion as mentioned in section 2.1.2. A time evolving analysis may be performed in the subsequent steps. The system of equations to be solved is broken up into parts. First α is solved for with S treated as data, followed by χ and z where α and S are treated as data. Finally we solve for u with χ and $grad z$ treated as data. Each of these solves were done using Newton-Raphson scheme. The time step is controlled by

$$\Delta t \leq \min \left\{ f \frac{h}{|V|}, \frac{0.002}{|\alpha \times V| + \dot{\gamma}} \right\}, \quad f \sim 0.1. \quad (2.72)$$

This reflects a conservative choice between a Courant condition and a maximum bound of 0.2% on the plastic strain increment. Here h is a minimum element edge length.

2.6 Parallelization of the Code

The above formulation is implemented in a Fortran code which invokes parallel PETSc (Balay *et al.*, 2001) libraries. PETSc automatically solves the system of equations in parallel on using appropriate commands. Calculations required to form respective matrices and vectors are divided equally into the number of processors through a separate FORTRAN subroutine. There were two major changes involved in the parallelization of the serial code: (a) defining vectors and matrices corresponding

to variables, α, χ, u, z , as parallel objects, and (b) extraction of values from a parallel vector (using commands like VecScatterBegin()/VecScatterEnd(), MPI_Send()/MPI_Recv()).

Scalability analysis was done to check the performance of the code. A cubical solid with an edge length of $20 \mu\text{m}$ is discretized into a finite element mesh of $20 \times 20 \times 20$ elements. The imposed boundary conditions are as follows: displacements on the bottom face are constrained in all three directions. The displacements corresponding to a compressive strain are prescribed through the kinematic boundary condition

$$u_2(x_1, x_2, x_3, t) = d(x_2) \dot{\Gamma} t \quad (2.73)$$

on the nodes of the top faces. Here, $d(x_2)$ is the height, from the bottom of the cube, of the point with coordinates (x_1, x_2, x_3) . Γ is the average engineering strain given by the ratio of the applied vertical displacement of the top surface to the cube height; $\dot{\Gamma}$ is an applied strain rate of 1 sec^{-1} , and t is time.

Material parameters used for this computational experiment are, $b = 2.5 \times 10^{-4} \mu\text{m}$, $k_0 = 20$, $m = 0.03$, $g_s = 210 \text{ MPa}$, $g_0 = 50 \text{ MPa}$, $\theta_0 = 205 \text{ MPa}$. The physical meaning of these parameters is described in Section 2.2. The reference strain rate is $\dot{\gamma}_0 = 1 \text{ sec}^{-1}$. Isotropic elastic constants of the representative material, Copper, are $E = 110 \text{ GPa}$, $\nu = 0.34$, where E is the Young's modulus and ν is the Poisson's ratio.

On increasing the number of processors from 10 to 40, the time required to attain 0.5% applied strain decreased from 4.3 hrs to 2.4 hrs. The scalability curve is shown in Figure 2.1. The *ideal* curve in Figure 2.1 is based on the assumption that the time required to do a simulation is halved on doubling the number of processors for a fixed problem size. As of now just a basic parallelization of the code has been done and it worked quite well for the kind of problems mentioned in this thesis. More changes are required to make it more efficient.

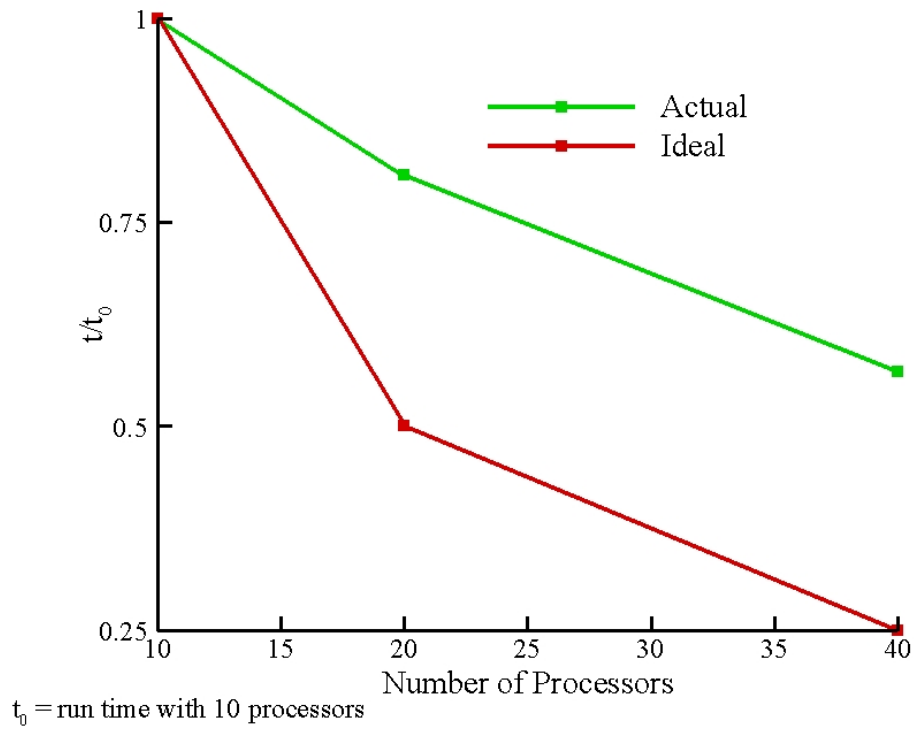


Figure 2.1. Curve showing the performance of small deformation *PMFDM* code implemented in FORTRAN (t is the total run time).

CHAPTER 3

MODELING DISLOCATION SOURCES AND SIZE EFFECTS AT INITIAL YIELD IN CONTINUUM PLASTICITY*

In this chapter we examine the question of how dislocation sources may be modeled in continuum plasticity and if the nature of sources contributes to size effects within a continuum representation of idealized simulation cells. We find the answer to be affirmative and use the strategy to demonstrate size effects at initial yield within the context of *PMFDM* theory (Acharya and Roy, 2006). Size effects at initial yield were modeled within a 2d Discrete Dislocation (DD) framework in Deshpande et al. (2005), Benzerga et al. (2005), Benzerga and Shaver (2006) and Balint et al. (2006) and, more recently using 3d DD techniques (Rao et al. (2008), Tang et al. (2008)). While those studies showed via selected DD frameworks that size effects may arise from aspects of dislocation source properties and source availability, they did not consider the fact that related size effects may arise simply from the dislocation source attributes and heterogeneous spatial arrangement coupling to the boundary constraints when considered completely within a continuum theory for the flow kinematics. Here we specifically discuss size effects at initial yield based on two continuum-level mechanisms. First, size effects are demonstrated in idealized simulation cells having a predefined pattern of statistical dislocation (SD) sources. For the second mechanism, simulations are performed on cells having an initial, spatially inhomogeneous excess dislocation (ED) distribution.

* Puri et. al. (2009)

This chapter is organized as follows: Section 3.1 involves discussion of modeling strategy and results so obtained. The chapter ends with some concluding remarks in Section 3.2. Constitutive specifications corresponding to $J2$ plasticity are used in this work. They are mentioned in detail in Section 2.2.

3.1 Results and Discussion

Unless otherwise mentioned, material parameters used for all the computational experiments are $b = 4.05 \times 10^{-4} \mu\text{m}$, $m = 1.0$, $g_s = 161 \text{ MPa}$, $g_0 = 17.3 \text{ MPa}$, $\theta_0 = 392.5 \text{ MPa}$ and $k_0 = 20.0$. The reference strain rate is $\dot{\gamma}_0 = 1 \text{ sec}^{-1}$. Isotropic elastic constants of the representative material, Aluminum, are $E = 62.78 \text{ GPa}$, $\nu = 0.3647$, where E is the Young's modulus and ν is the Poisson's ratio. The meaning of these parameters is described in Section 2.2.

A comment on the rate sensitivity value is in order. Our intent here is to model a situation where dislocations move in unobstructed, free-flight mode in large parts of the body. Under these circumstances, and with the understanding that rate-insensitivity is a manifestation of very fast motions homogenized in time with near stationary events, it is only reasonable to utilize a rate-sensitivity parameter value representative of linear drag in our simulations.

Time-dependent simple-shearing solutions are studied numerically. The imposed boundary conditions corresponding to such a loading are as follows: displacements on the bottom face are constrained in all three directions while those on the top, left and right faces are constrained in the x_2, x_3 directions only (Figure 3.1). The front and back faces are displacement-constrained in the x_3 direction and traction free in

x_1, x_2 direction. The displacements corresponding to a simple shear strain are prescribed through the kinematic boundary condition

$$u_1(x_1, x_2, x_3, t) = d(x_2) \dot{\Gamma} t \quad (3.1)$$

on the nodes of the left, right, top and bottom faces. Here, $d(x_2)$ is the height, from the bottom of the cube, of the point with coordinates (x_1, x_2, x_3) . Γ is the average engineering shear strain given by the ratio of the applied horizontal displacement of the top surface to the cube height; $\dot{\Gamma}$ is an applied shear strain rate of 1 sec^{-1} , and t is time.

All computations are performed on one of two desktop machines with 2GB and 8GB RAM, respectively using the serial code. In the interpretation of results, symbol τ refers to the nominal (reaction) shear traction on the top surface of the simulation cell.

3.1.1. Dislocation source distribution

The effect of physical dimensions of the simulation cell (having a predefined distribution of SD sources) on the initial yield strength is described in this section. First we discuss how a Frank Read source is grossly represented in our framework. In general, a Frank Read source produces dislocation loops that cannot be sensed if their size is less than the scale of resolution. However, once the loop expands up to the scale of resolution, it can be sensed as demonstrated in Figure 3.2a. In order to numerically simulate (SD) dislocation sources in the framework of PMFDM, the size of the region representing a source is assumed to be greater than or equal to the scale of resolution (Figure 3.2b). In the interior of the source region there are no EDs due to cancellation in signs during averaging. This corresponds to the physical situation of the dislocation loop not being sensed when its size is smaller than the scale of

resolution. The plastic strain rate corresponding to the motion of these unresolved dislocations, however, is sensed, and is taken into account through L^p . At the interface between slipped and un-slipped region, EDs are observed due to the gradient in plastic strain rate (2.9)₆. This observation corresponds to the physical definition of a dislocation loop being sensed when its size equals or exceeds the scale of resolution. A simple test is performed to demonstrate this idea. Consider a cubical cell of edge length of 1.0 μm and discretized into a finite element grid. The element at the center is the dislocation source region, as shown in Figure 3.2b. The cell is unstressed and ED free initially, with some SD content in the source region. Displacement boundary conditions corresponding to a simple shear strain of 0.1% are imposed. With the onset of plasticity in the source region, excess edge dislocations (α_{13}) of opposite signs generated at the sub-grid scale of resolution cancel each other, resulting in zero ED density inside the source region, though a change in the magnitude of L_{12}^p values corresponding to these cancelled dislocations is observed. Since L^p is zero in non-slipped regions, a gradient in L_{12}^p develops at the interfaces of the slipped and non-slipped regions which in turn leads to the generation of α_{13} through (2.9)₆, as shown in Figure 3.2c. The generated α_{13} density contributes to flow in the non-source-containing grid elements.

Now we discuss size effects at initial yield in cells having a predefined distribution of dislocation sources. Two cubical samples with edge lengths of 0.6 μm and 3.0 μm are considered. Spatial distribution of dislocation sources is shown in Figure 3.3. Both cells are discretized into a finite element grid with equal element size and equal to the size of a dislocation source region, in order to avoid any size effect due to the scale of resolution. Displacement boundary conditions corresponding to an engineering simple

shearing strain of 0.3% are imposed on the cells as in (3.1). First, experiments were performed in the context of conventional plasticity theory. Conventional plasticity may be recovered from PMFDM by setting $\alpha = \mathbf{0}$ for all times and replacing (2.9)₄ with

$$\mathbf{U}^e = \text{grad } \mathbf{u} - \mathbf{U}^p ; \dot{\mathbf{U}}^p = \mathbf{L}^p \quad (3.2)$$

Since, $\alpha = \mathbf{0}$ in the conventional plasticity framework, non-source regions are elastic in nature. A size effect is observed for this case as shown in Figure 3.4, with smaller being harder. It can be inferred from dimensional analysis that in the case of a homogeneous material, there is no length scale in the classical plasticity theory and hence it is not possible to predict size effects in this framework. However, a length scale emerges when a body consisting of discrete dislocation sources is considered. Dimensional analysis of τ yields,

$$\tau = \mu \Phi \left(\frac{\theta_0}{\mu}, \frac{g_s}{\mu}, \frac{g_0}{\mu}, \frac{\dot{\Gamma}}{\dot{\gamma}_0}, m, \Gamma, \frac{s}{H} \right), \quad (3.3)$$

where H denotes the dimension of the body, s is a representative measure of the distance between the sources (strictly speaking, the size of the sources should also enter as another length-scale parameter), and Φ is a dimensionless function of the arguments shown. It can be deduced from the relation above that if s is kept the same and H is changed, a difference in average response is expected. Thus, it is the spatial layout of dislocation sources that introduces a physical length scale in classical plasticity theory which is otherwise absent. However, the magnitude of that size effect on an average response utilizing discrete sources in an otherwise conventional elasto-plastic material falls short of what is qualitatively observed in experiment, indicating the existence of other scale effects and the need for better theory. Nonetheless, this same phenomenology of dislocation sources carries in PMFDM, but now with a

greater effect because of the generation of ED at all spatial discontinuities of flow (such as source and non-source grid elements) and its transport, as well as its accurate accounting in stress response via (2.9)₁₋₅.

The same numerical experiment is now performed with PMFDM. Accordingly, two cubical cells having edge lengths of 0.6 μm and 3.0 μm and a spatial distribution of dislocation sources as shown in Figure 3.3, are considered. *The area density of sources is identical(0.1) in both cells.* The displacement boundary conditions corresponding to a simple shear strain of 0.8% are applied through (3.1). The non-source regions can behave in a plastic manner when ED content is transported through them; however, there is no SD slip rate in these regions.

The average shear stress-strain response, in Figure 3.5a, shows that initial yield strength strongly depends on the cell size with smaller being harder. The size effect is maintained throughout the process of deformation in qualitative agreement with experimentally observed trends (Dimiduk *et al.*, 2005; Greer *et al.*, 2005). A significant stress drop corresponding to the dislocation activity developing bursts of plastic strain rate is observed in our results which is absent in the experimental results Uchic *et al.* (2004) but may be present in the results from Greer *et al.* (2005). This is due to the fact that numerical experiments performed here correspond to displacement control (similar to those by Greer *et al.* (2005)) whereas the experimental results presented in Uchic *et al.* (2004) and Dimiduk *et al.* (2005) involved mixed (load and displacement) control. The applied load was not allowed to decrease during the experiments performed by Uchic *et al.* (2004) and Dimiduk *et al.* (2005) and thus, stress drops are not observed for that study. The other serrations observed in the experimental results can be obtained in this setup by incorporating a stochastic constitutive response for the plastic strain rate and the ED velocity. We have

intentionally stayed away from doing so to demonstrate size effects with the least constitutive input.

In order to understand the cause of size-effect in the current framework, dimensional analysis of the applied, (reaction) nominal stress τ is performed which implies the following relation,

$$\tau = \mu \Phi \left(\frac{\theta_0}{\mu}, \frac{g_s}{\mu}, \frac{g_0}{\mu}, \frac{\dot{\Gamma}}{\dot{\gamma}_0}, \frac{b}{H}, \alpha_0 H, m, \Gamma, k_0, \eta, \frac{s}{H} \right) \quad (3.4)$$

where, α_0 is a representative measure of the magnitude of the initial ED density field, s is a representative measure of the distance between sources and Φ is a dimensionless function of the arguments shown. The dimensionless arguments $b/H, \alpha_0 H, s/H$ introduce a dependence of average response on the Burgers vector of the material, the geometric proportion of the body, the initial ED density and the layout of sources. In these series of tests, the response is independent of $\alpha_0 H$ as the specimens were initially ED-free. Due to the change in spatial distribution of dislocation sources (with associated changes in ED generation), internal stresses may change. Thus, s/H corresponds to the effect of internal stresses of dislocation distributions on average response. The argument (b/H) corresponds to the size effects due to dislocation mobility (2.58) and strain hardening (2.59). To evaluate the dependence of the response on internal length scale in strain hardening, the following equation is used for strength rate instead of (2.59),

$$\dot{g} = \theta_0 \left(\frac{g_s - g}{g_s - g_0} \right) \{ |\boldsymbol{\alpha} \times \boldsymbol{V}| + \dot{\gamma} \}. \quad (3.5)$$

Use of such an equation removes all excess hardening by the ED evolution and interactions as can be seen from the following expression

$$h = \frac{dg}{dP} = \theta_0 \left(\frac{g_s - g}{g_s - g_0} \right); P = \int \{ |\boldsymbol{\alpha} \times \mathbf{V}| + \dot{\gamma} \} dt. \quad (3.6)$$

Nonetheless, significant size effects are observed as shown in Figure 3.5b. Thus, from these sets of computational experiments it may be inferred that a strong size effect at initial yield in PMFDM is primarily due to length scales induced by i) a discrete SD source distribution and ii) the ED mobility, but not due to strain hardening in the mean-field or Stage II sense. This finding is qualitatively consistent with the recent reports by Norfleet *et al.* (2008), and Rao *et al.* (2008), both of which show a potent size effect in microcrystal deformation that is associated with the instantaneous mobile dislocation density relative to the imposed loading conditions. Further, the result does not preclude other hardening phenomena, such as the absence of sources as suggested by Greer *et al.* (2005), or the hardening of sources as suggested by Parthasarathy *et al.* (2006), from providing alternate or additional hardening mechanisms, respectively. Those effects, while not investigated in the present study, may be represented via alternative selections of the constitutive assumptions of (13-15).

3.1.1.1. Effect of dynamic instability

To study the possibility of dynamical sensitivity of the stress-strain response at initial yield, additional numerical experiments were performed, each corresponding to a small perturbation of the order of 10^{-15} μm in the boundary condition for displacement. The spatial distribution of sources is assumed to be similar to that used in section 3.1.1. It is observed that this small magnitude of perturbation in boundary condition results in a significant difference in the stress-strain response as shown in Figures 3.6a and 3.6b. There is about a 34% variation in the shear stress at 0.8% applied strain for

the cell having an edge length of $0.6\mu\text{m}$ and 16% for the cell having a $3.0\mu\text{m}$ edge length. The mean shear stress-strain response for each cell size is shown in Figure 3.6c. The mean values show a cell-size dependence with smaller being harder.

The mechanical response at macroscopic scale is insensitive to minor perturbations. At the macroscopic scale, sources are considered to be present everywhere in the body. Motivated by this fact, numerical experiments were performed with sources present everywhere in the body, i.e. L^p is set active in the entire cell. The four simple shear experiments with varying boundary condition perturbations were performed on the small and big cells. It was observed that in the case of plastically unconstrained cells the stress-strain response up to 0.8% simple shear strain is insensitive to such perturbation in the boundary conditions.

From these experiments and results presented in Roy and Acharya (2006) pertaining to the effect of size on stability of stress-strain response in PMFDM, one may infer that i) discreteness in source distribution and ii) decreasing cell size lead to dynamical sensitivity to perturbations in this model. Note that a qualitatively similar sensitivity to perturbations was found in DD simulations by Deshpande *et al.* (2001). Interestingly, there are experimental observations of drastically different responses in samples of the same size when subjected to a prescribed deformation (Uchic *et al.*, 2004). However, it is not yet possible to deduce from those experiments the degree to which such variation results from differences in initial dislocation configurations and how much may result from small perturbations in the testing. The existence of such intrinsic instability in flow response also emphasizes the importance of the stochastic nature of the material response and the need to average over large numbers of samples to glean the typical material behavior at small scales.

3.1.1.2. Variation of microstructure

It was deduced from dimensional analysis performed in section 3.1.1 that the stress-strain response of PMFDM material depends upon the dimensionless argument s/H . Here we investigate the effect of changes in the spatial distribution of sources in a cell of fixed size containing a fixed source density. Calculations for a cubic cell having an edge length of $3\mu\text{m}$ were performed with three different patterns of source distribution, as shown in Figure 3.7. No perturbations were imposed in this case. Figure 3.7 shows that average stress at 0.8% applied strain varies approximately from 43 MPa to 180MPa with varying source pattern. This demonstrates the variation of mechanical response of same-sized cells with a change in microstructure.

Since cells (a) and (c) are geometrically symmetric (if cell (a) is rotated by 180 degrees about the x_3 direction, it will be geometrically similar to cell (c)), the intuitive expectation is to get the same response in these cases. It is evident from Figure 3.7 that the top face of (a) corresponds to the bottom face of (c) after rotation. Reaction forces, however, are measured at the top face of all cells. The cause for this difference in the reaction force for the two different source patterns is due to the presence of non-zero tractions in the 1-direction on left and right faces of the cube due to the imposed displacement boundary conditions for simple shear. Accordingly, the reaction forces on the top need not be equal in magnitude to the reaction forces at the bottom of the cell. The horizontal reaction force on the top face of (a) (bottom face of (a)) was indeed identical to the horizontal reaction at the bottom face of (c) (top face of (c)) as required by symmetry. The top and bottom face reactions would have to be equal in magnitude from statics for both (a) and (c) if the side faces of the cube were traction free in the 1-direction; this was verified in our numerical experiments.

Power (P) is calculated for cases (a) and (c) using the following expression,

$$P = \int_{\partial B} \mathbf{t} \cdot \mathbf{v} \, da \quad (3.7)$$

where, \mathbf{t} is the traction on the external surface and \mathbf{v} is the velocity. It was found that for a certain time increment in the plastic regime, total supplied power in case (a) and (c) differ by a very small amount (2.3 %).

3.1.2. Size effects due to initial ED distribution

Low energy dislocation microstructures are observed in materials. Such structures frequently consist of an array of like-signed dislocations having a low-energy arrangement, such as a tilt or twist boundary. Here we investigate the variation of initial yield strength in cells having a predefined spatial distribution of initial ED density of a common sign. Two cubical cells having edge lengths of $0.6\mu\text{m}$ and $3\mu\text{m}$ are considered. The spatial distribution of initial ED density is shown in Figure 3.3 for an excess edge-dislocation density of $\alpha_{23} = -2.025 \times 10^{-3} \mu\text{m}^{-1}$ prescribed on the nodes of shaded elements. In order to obtain an equilibrium state of initial ED density distribution, cells are relaxed in time without any external load. The volume average of $|\alpha|$ is used as a measure of ED content in the cell. Equilibrium is considered to be attained at $t = 0.03\text{sec}$ when this measure attains a constant value with respect to time, as shown in Figure 3.8a. The strength of the material is assumed to be constant throughout the deformation process, i.e. $\dot{g} = 0$ in (2.59). Once equilibrium is attained, simple shear boundary conditions corresponding to a strain of 0.3% are imposed on the cells. The average shear stress at 0.3% strain for the cell having an edge length of $0.6\mu\text{m}$ is 2.5 times higher than that of cell having a $3\mu\text{m}$ edge length as shown in Figure 3.8b. Next, a similar test was performed with an initially-prescribed ED

density of same magnitude and opposite in sign. A reversed size effect is observed in this test wherein the larger cell shows a harder response (Figure 3.8b). One can infer from the dimensional analysis performed in section 3.1.1 (3.4), that the average response of the material depends upon $\alpha_0 H$ for these cases. With a prescribed α_0 among different sized cells a size effect is expected but it is not possible to predict the sense of size effect based on dimensional analysis alone. Due to the complexity and difference in initial ED distribution in these examples, a simpler problem is studied to understand the variation in the sense of size effect depending on the sign of initial ED density. For this simpler case, an initial excess edge-dislocation density $\alpha_{23} = 2.025 \times 10^{-3} \mu\text{m}^{-1}$ is prescribed at the center of two cubic cells having edge lengths of $0.6 \mu\text{m}$ and $3 \mu\text{m}$, as shown in Figure 3.9. The cells are relaxed in time to obtain corresponding equilibrated ED arrangements. Then, displacement boundary conditions corresponding to an engineering simple shearing strain of 0.3% are imposed on the cell. The average shear stress-strain response demonstrates that the smaller cell is indeed harder than the large one. However, a reversed size effect is observed with a change in sign of initial excess dislocation density (Figure 3.9). This phenomenon is explained as follows.

Consider a traction free finite cubical block containing a dislocation. In order to understand the resulting stress distribution in the block, we first note that the equations for determining the stress field of a specified ED field in PMFDM are linear; thus superposition applies. Consider now the stress field of a dislocation in an infinite medium, situated as in Figure 3.9. This infinite medium stress field naturally induces tractions on the surface of the finite crystal. Thus, image tractions equal in magnitude and opposite in sign of those induced by the dislocation need to be present on the external surface of the block to satisfy the traction free boundary conditions.

Therefore, the *initial stress* field of a traction free finite crystal in equilibrium can be considered as a superposition of (a) the internal stress due to initial ED distribution in the linear elastic infinite medium and (b) the image stress required to satisfy the traction-free boundary conditions. When an external stress is applied, the stress at any point in the finite body is a sum of the initial stress and the applied stress due to boundary conditions (again using superposition) at that point. In the regions having an initially prescribed ED density, less applied stress is required to cause flow if both the initial stress and the applied stress are of the same sign as compared to the case when both are of opposite sign. Now, consider two cubic blocks of different sizes and same initial ED distribution. The magnitude of image stress corresponding to the $(1/r)$ fundamental stress field of a dislocation is higher for the smaller block than the larger block. Accordingly, in the case of the external applied stress being the same sign as the initial stress in the dislocation ‘core’ region, the smaller cell yields before the large cell (for a constant yield stress). If the sign of the initial ED density is now changed with the direction of applied stressing remaining the same, the initial stress changes sign, the larger cell has a smaller-in-magnitude initial stress that *subtracts* from the applied stress and consequently yields later than the smaller cell.

3.2 Conclusions

A finite element implementation of PMFDM has been shown to predict size effects at initial yield in plasticity of micron-scale simulation cells. The results are qualitatively consistent with experimental observation in Uchic *et al.* (2004), Dimiduk *et al.* (2005) and Greer *et al.* (2005), as well as with recent discrete dislocation simulations of Weygand *et al.* (2007), Senger *et al.* (2008), Tang *et al.* (2007, 2008) and Rao *et al.*

(2008). In the PMFDM framework, size effects are caused by the internal stress of the dislocation distribution, its coupling to the imposed deformation conditions including deformation rate and, natural length scales that enter the theory through strain hardening and the ED velocity. However, an important observation from the computational experiments presented here is that length scales associated with the internal stress due to discrete source patterns and those associated with the plastic strain rate of ED, are solely sufficient for size effects at initial yield within this model. We observe a sensitivity of the overall mechanical response to the presence of discrete source volumes or regions. Size-effect reversals under appropriate circumstances are also observed and explained. For the most part, such sample-scale kinematical size effects have not been treated in DD simulations (notable exceptions being those following the Needleman-Van der Giessen formulation of discrete DD) and, have only been peripherally considered in explanations of the widening set of size-effect experiments.

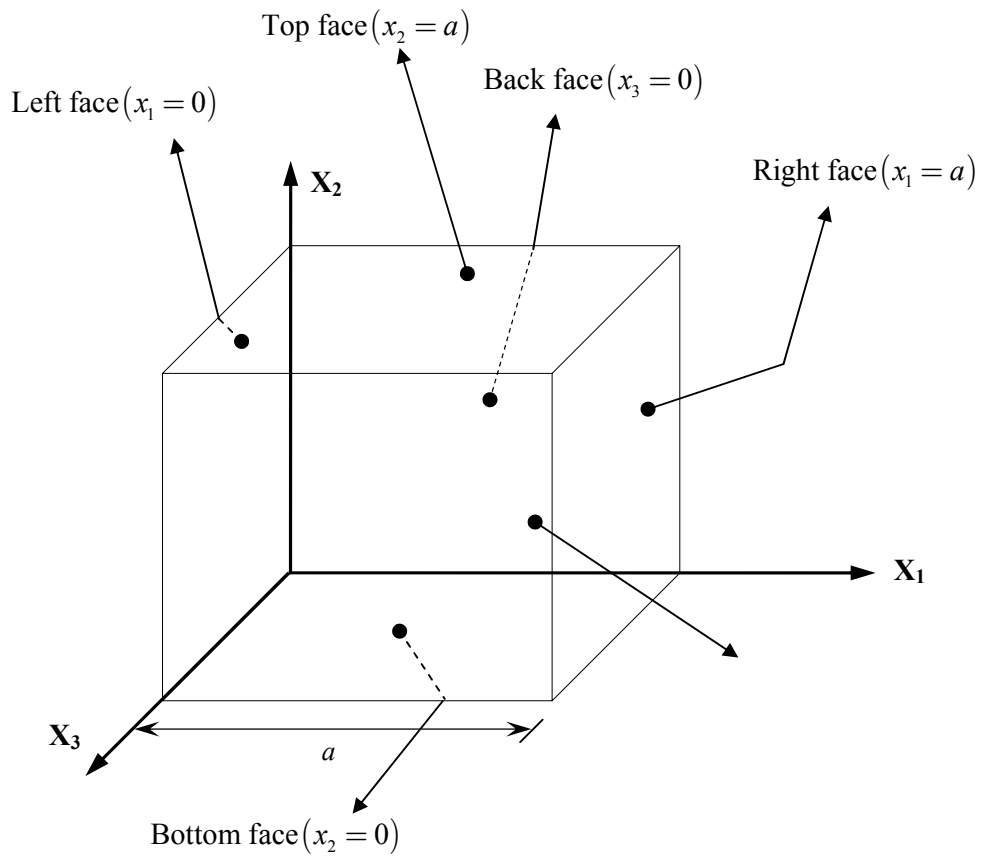


Figure 3.1. Schematic layout of a typical model geometry.

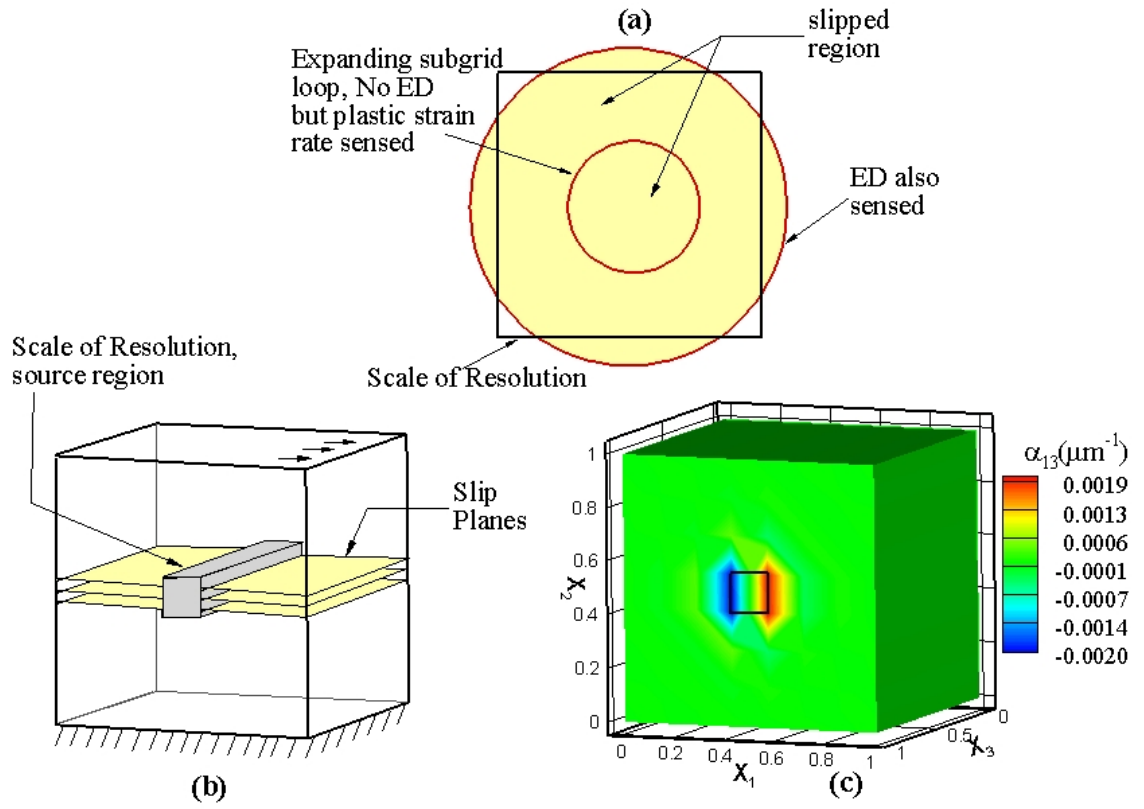


Figure 3.2. (a) Physical representation of a Frank Read source; (b) Representation of a numerically simulated Frank Read Source; (c) Excess dislocation density at $\Gamma = 0.1\%$ for pattern (a)

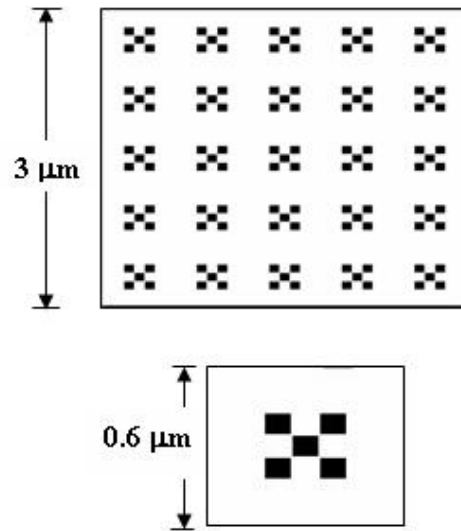


Figure 3.3. Schematic layout of position of sources (Black spots represents the dislocation sources)

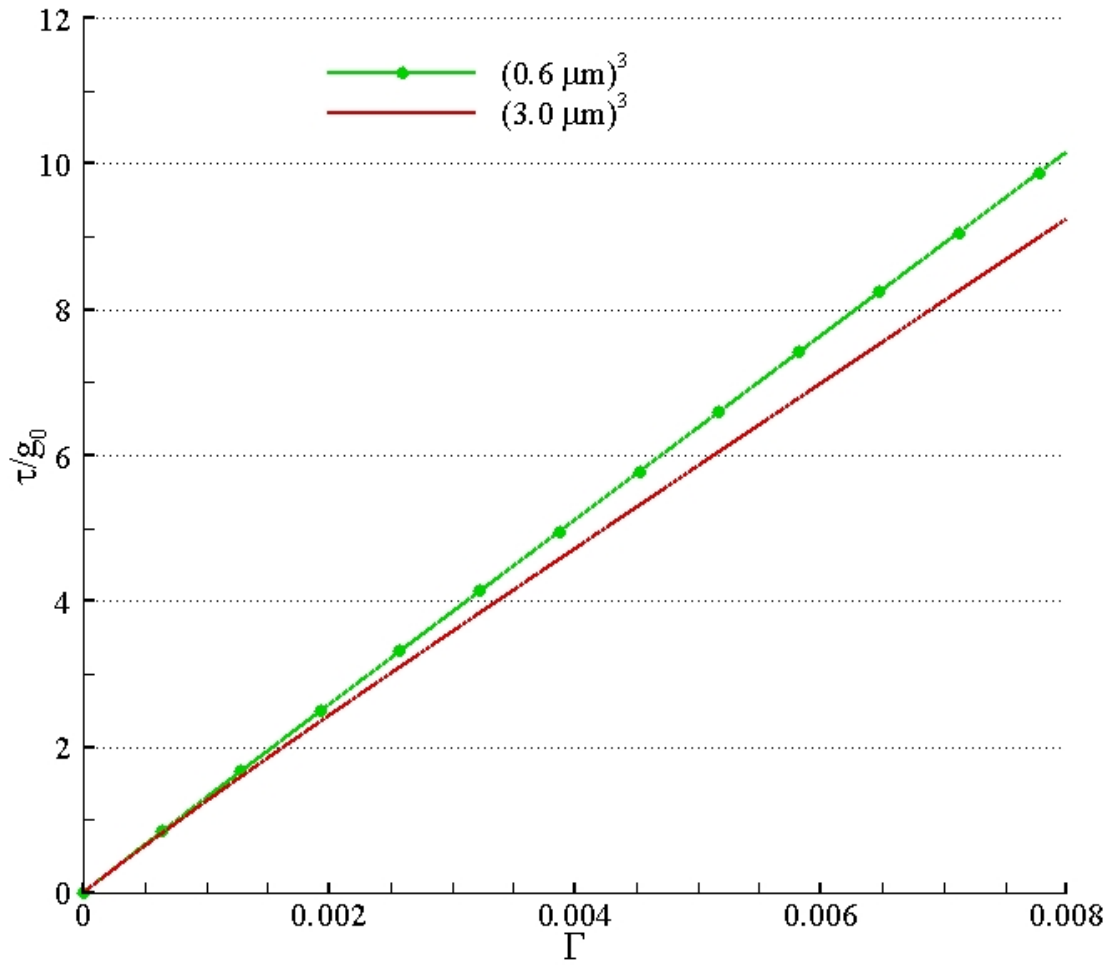
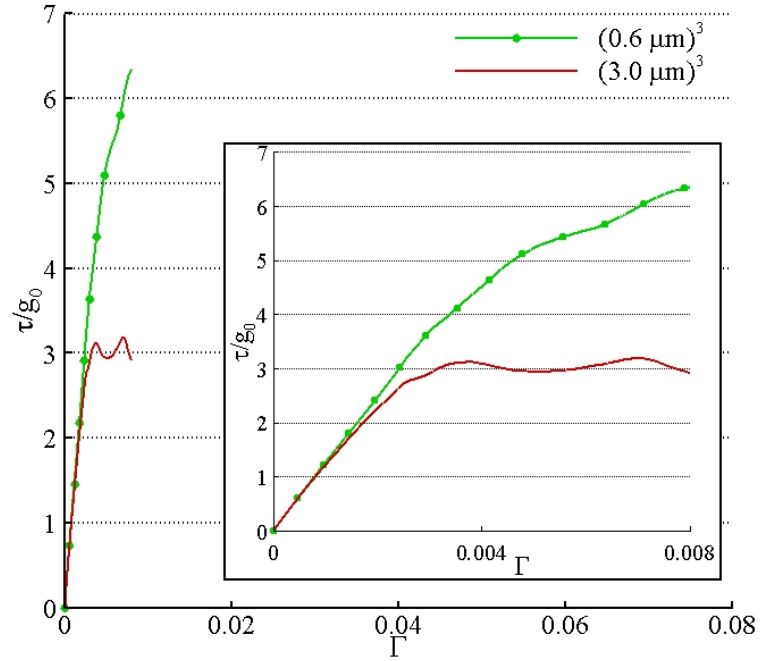
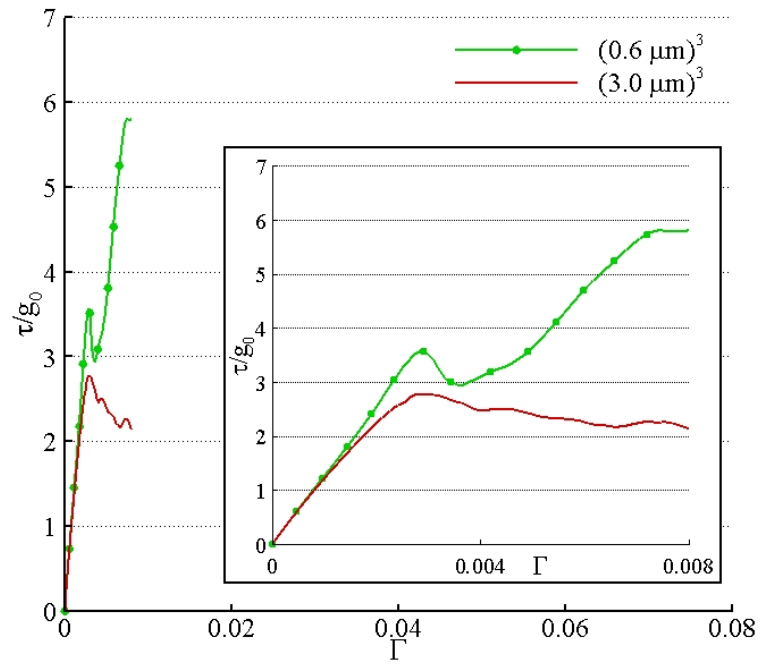


Figure 3.4. Size effect in simple shear with a predefined spatial distribution of dislocation sources, within a conventional plasticity framework.



(a)



(b)

Figure 3.5. Size effect in simple shear with a predefined source pattern with: (a) equation (2.59) used for hardening rate, (b) equation (3.5) used for hardening rate.

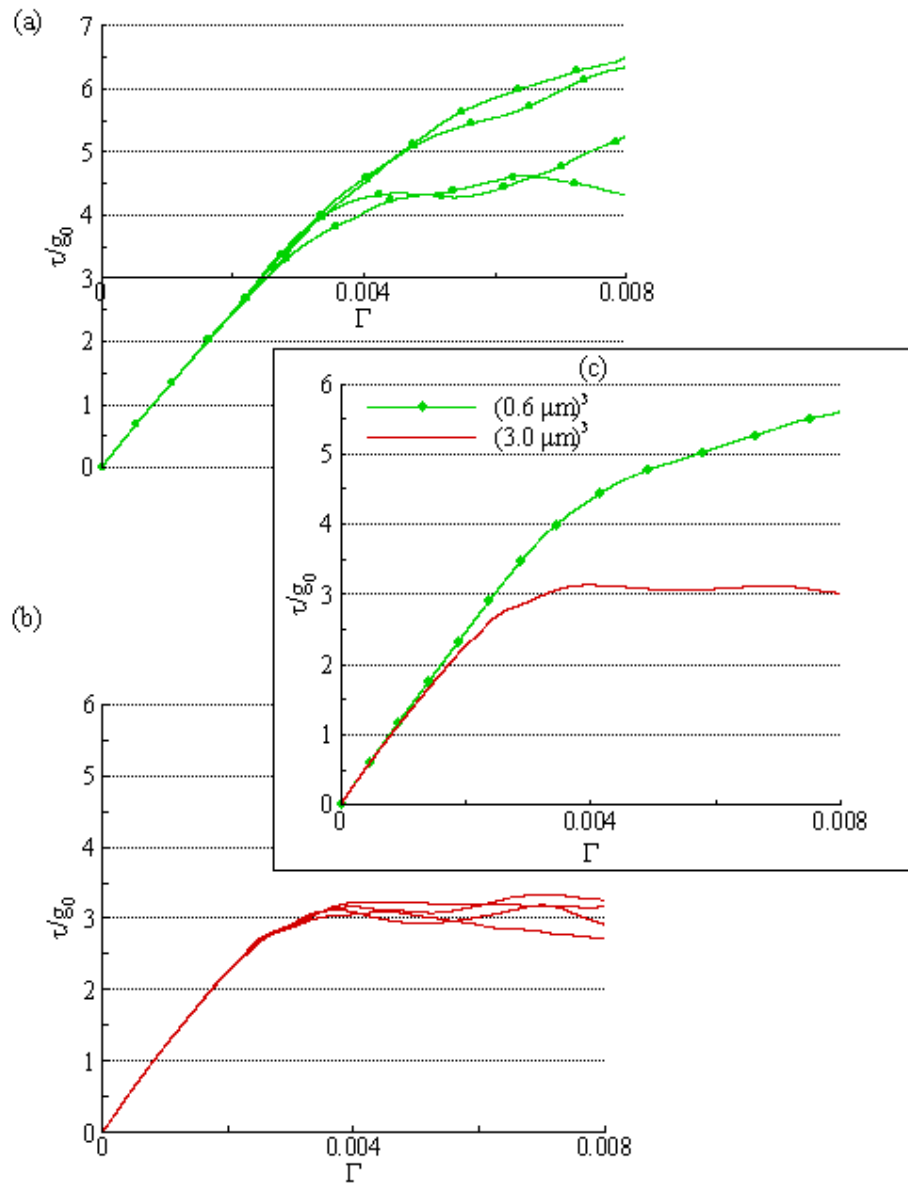


Figure 3.6. Variability in stress-strain response in simple shear with perturbation in boundary conditions: (a) $0.6 \mu\text{m}$, (b) $3.0 \mu\text{m}$ and (c) Mean response for the two sizes

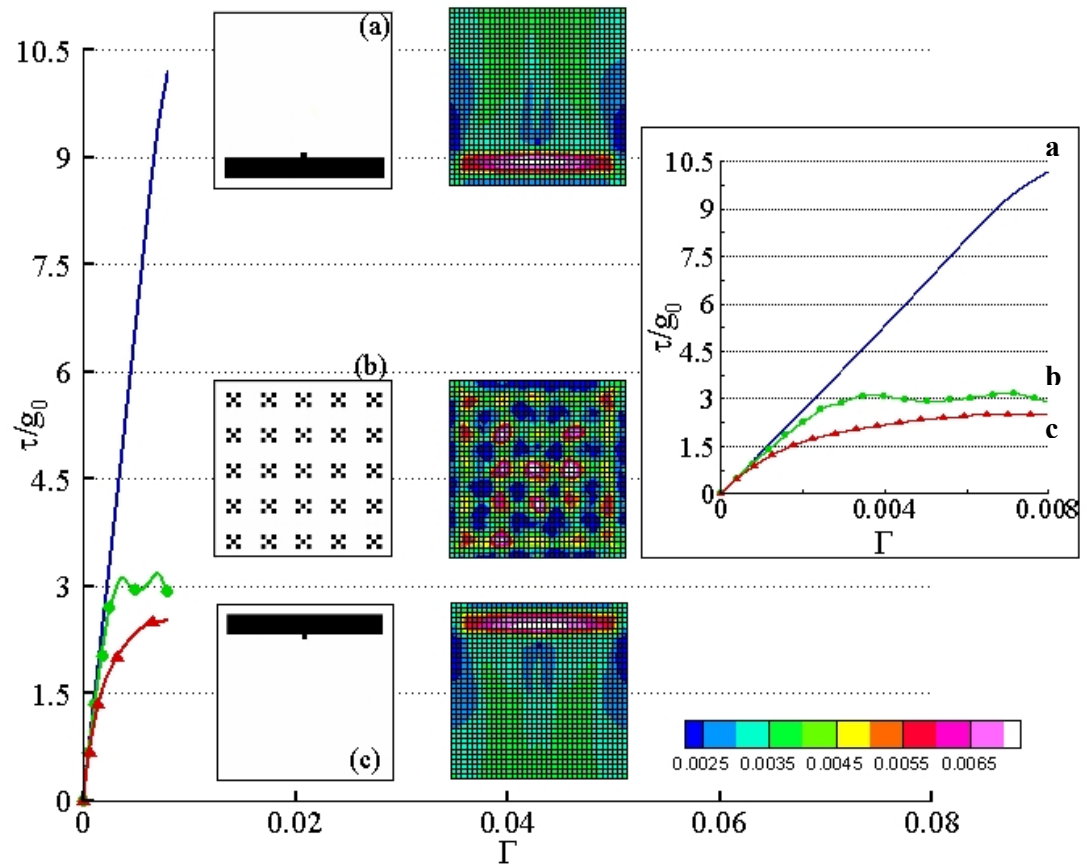
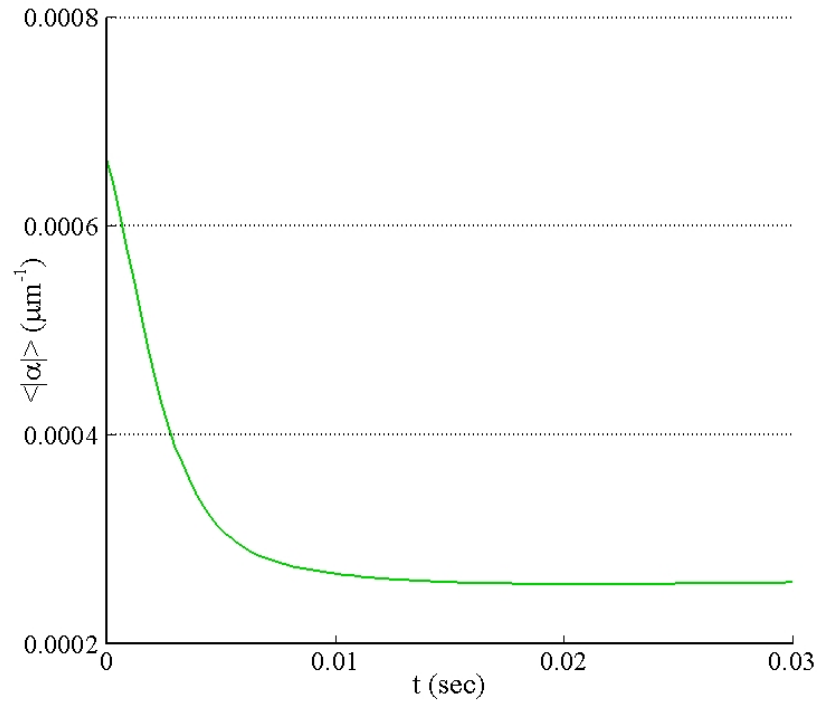
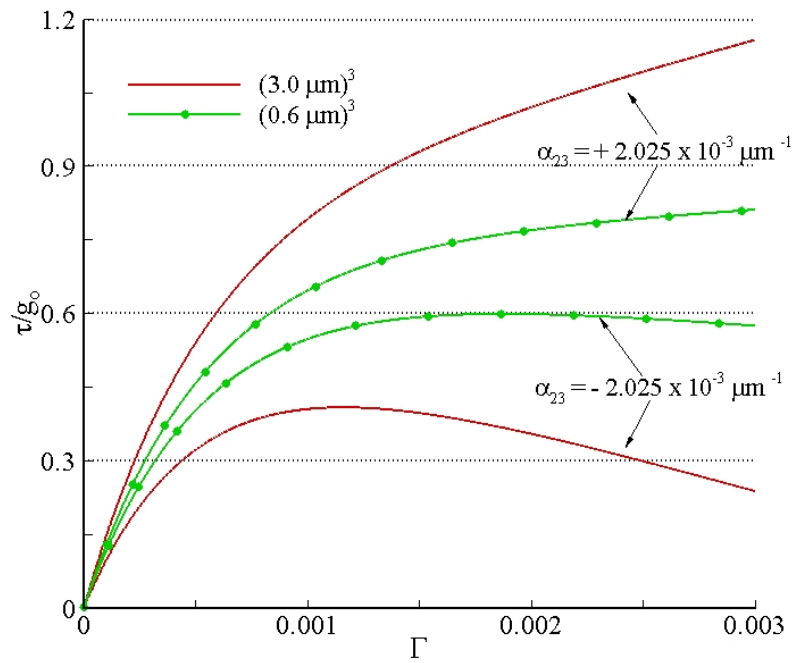


Figure 3.7. Variability in stress-strain response with change in the source pattern.



(a)



(b)

Figure 3.8. (a) Variation in average of $|\alpha|$ over the whole domain with time, (b) Size effect in simple shear with a non-zero initial excess dislocation density.

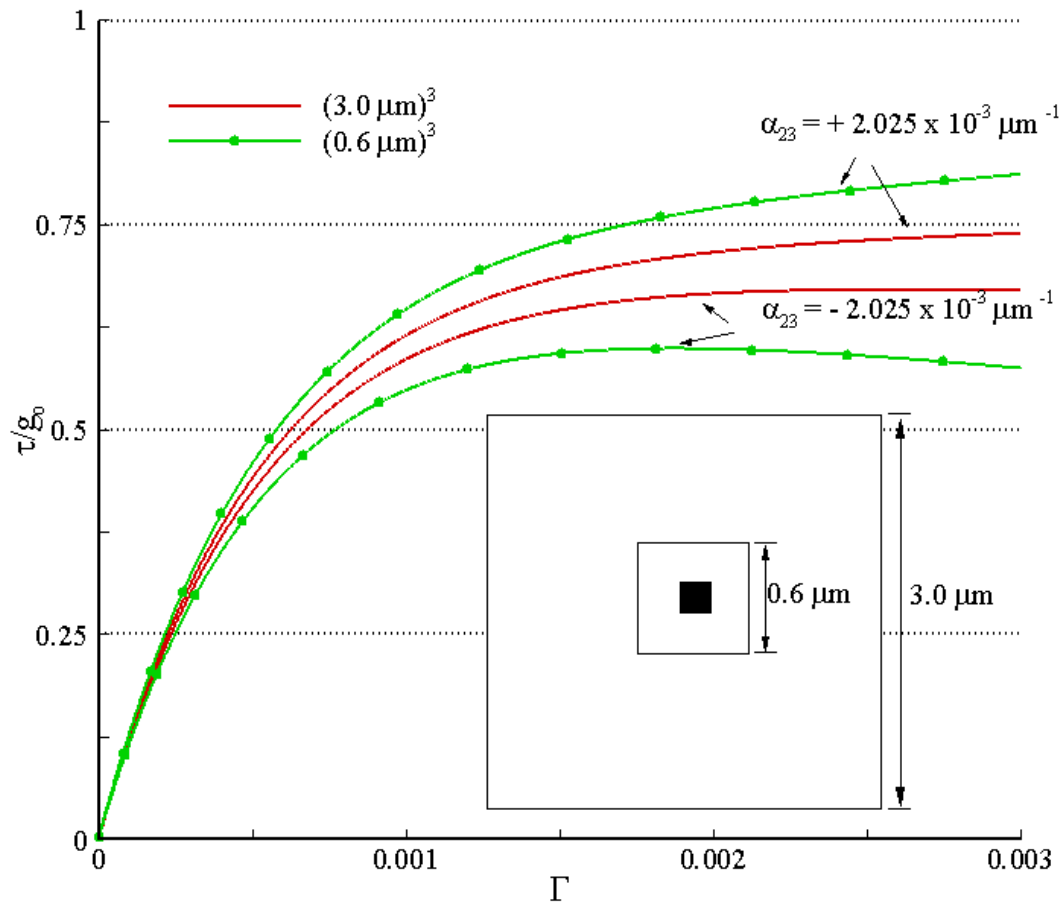


Figure 3.9. Size effect in simple shear with a non- zero initial excess dislocation density and the new pattern as shown in the inset.

CHAPTER 4

GRAIN BOUNDARIES IN CONTINUUM PLASTICITY MODEL

A grain boundary is an interface between two grains of different orientation. It may act as a source/sink or an obstruction to the flow of dislocations. Any of these possibilities significantly affect the evolution of microstructure of polycrystalline solids which subsequently affects their mechanical response. It is not possible to model these features in classical crystal plasticity theory due to the absence of an explicit characterization of dislocations. In Discrete Dislocation modeling, the correct rules for dislocation transmission through grain boundaries are not known yet.

In the *PMFDM* framework, a polycrystal is set up by using appropriate slip systems for different grains. However, by doing so the structure of equations allows free flow of dislocations through grain boundaries. A jump condition at an interface for excess dislocation density in the context of *PMFDM* theory is developed in Acharya (2007). This jump condition allows the modeling of different characteristics of grain boundaries and its implementation is discussed in this chapter. The deformation of a bicrystal under different classes of constraints to plastic flow is presented as a test case. Cases with dislocation sources distributed throughout the grain as well as localized to the region adjacent to grain boundary will be considered. The influence of a length scale introduced due to the spatial distribution of sources on plastic response will also be studied.

This chapter is organized as follows: an auxiliary field is introduced in the numerical implementation of the theory in addition to those mentioned in Chapter 2 and is discussed in Section 4.1. The jump condition at an interface for excess dislocation density evolution is discussed briefly in Section 4.2 for completeness. Implementation of the jump condition in the finite element framework is discussed in Section 4.3 followed by an illustration of the effect of grain boundary constraints on mechanical response of a bicrystal in Section 4.4. The chapter ends with some concluding remarks in Section 4.5.

4.1 Solving for \bar{z}

As mentioned in Section 2.1.1, the evolution equation for excess dislocation density admits a boundary condition on $\bar{\alpha} \times \bar{V} + L^p$. Due to the use of a primarily explicit solution framework, constraint boundary conditions on $\bar{\alpha} \times \bar{V} + L^p$ (plastic flow) cannot directly be accounted for in the discretization of equations for \bar{z} . An auxiliary field \mathbf{P} , is introduced to implement the same boundary condition for plastic flow in \bar{z} solve,

$$\begin{aligned} \text{div}(\text{grad } \dot{\bar{z}}) &= \text{div}(\mathbf{P}) \\ \mathbf{P} &= \bar{\alpha} \times \bar{V} + L^p \\ \mathbf{P} \times \mathbf{n} &= (\bar{\alpha} \times \bar{V} + L^p) \times \mathbf{n} \text{ on } \partial B \end{aligned} \tag{4.1}$$

From here onwards in Section 4.1, fields without overhead bars refer to averaged fields. First, \mathbf{P} is calculated from (4.1)₂₋₃ and then \mathbf{z} is updated using (4.1)₁. LSFEM is used for the discretization of equations (4.1)₂₋₃,

$$\int_B \delta P_{ij} [P_{ij} - L_{ij}^t + e_{jmk} \alpha_{im}^t V_k^t] dv + k \left(\int_{\partial B} \delta P_{ik} e_{jkl} n_l [e_{jmn} P_{im} n_n - \alpha_{im} n_m V_j - e_{mnj} L_{im}^t n_n] da + \int_{\partial B_o} \delta P_{ik} e_{jkl} n_l [\alpha_{ij} V_m n_m] da + \int_{\partial B_i} \delta P_{ik} e_{jkl} n_l F_{ij} da \right) = 0 \quad (4.2)$$

\mathbf{F} is the prescribed flux on the inflow boundary (∂B_i), ∂B_o is the set of outflow/neutral points of the boundary where $\mathbf{V} \cdot \mathbf{n} \geq 0$. k is introduced as a penalty parameter for the constraint condition, (4.1)₃. k is set to be equal to 10.0 if a particular external surface is a barrier to the flow of dislocations, other wise it is set to zero. \mathbf{P} is calculated using LSFEM only if a particular element has at least one face that is a part of external surface of the body. The Standard Galerkin method is used for the discretization of (4.1)₁,

$$\int_B \delta z_{i,j} [z_{i,j} - z_{i,j}^t - \Delta t (P_{ij}^t)] dv = 0 \quad (4.3)$$

specify $z_i = 0$ at an arbitrarily chosen point.

4.2 Jump Condition for Excess Dislocation Density (ED)

The jump condition for excess dislocation density along a *material* interface in *PMFDM* is explained briefly in this section. The evolution equation for excess dislocation density is,

$$\dot{\boldsymbol{\alpha}} = -\text{curl } \mathbf{S} + \mathbf{s} \quad (4.4)$$

Since, $\boldsymbol{\alpha}$ is a solenoidal field, i.e. divergence free, the nucleation rate field, \mathbf{s} , can be written as a curl of a second order tensor valued nucleation rate potential field, $\boldsymbol{\Omega}$,

$$\mathbf{s} = \text{curl } \boldsymbol{\Omega} \quad (4.5)$$

At a *material interface* the result reduces to

$$[[\mathbf{S}]] \times \mathbf{n} + [[\mathbf{\Omega}]] \times \mathbf{n} = \mathbf{0}. \quad (4.6)$$

The value of $\mathbf{\Omega}$ can be set in accord with the nature of grain boundary. Equation (4.6) can be used to model different classes of grain boundaries. However, in this particular study a simplified case is considered as an example. Here, the grain boundary is assumed not to be a source/sink. This corresponds to $[[\mathbf{\Omega}]] = \mathbf{0}$. Thus, (4.6) reduces to,

$$[[\mathbf{S}]] \times \mathbf{n} = \mathbf{0} \quad (4.7)$$

Consider a sample consisting of two grains, B_1 and B_2 , with c being the interface between them; \mathbf{n} is a unit normal to the interface, as shown in Figure 4.1. For this idealized problem, (4.7) can be written as,

$$(\mathbf{S}_1 - \mathbf{S}_2) \times \mathbf{n} = \mathbf{0} \quad (4.8)$$

where, \mathbf{S}_1 and \mathbf{S}_2 correspond to grains B_1 and B_2 , respectively. This jump condition can be satisfied in two ways:

- a. Imposing $(\mathbf{S}_1 - \mathbf{S}_2) \times \mathbf{n} = \mathbf{0}$ on the interface, c .
- b. Imposing $\mathbf{S}_1 \times \mathbf{n} = \mathbf{0}$ and $\mathbf{S}_2 \times \mathbf{n} = \mathbf{0}$ on the interface, c .

Case (b) allows the modeling of completely constrained (blocked) plastic flow on either side of the grain boundary. This corresponds to the idealized situation of the grain boundary being impenetrable to dislocations.

4.3 Numerical Implementation

Now we discuss the imposition of conditions (a) and (b) mentioned in Section 4.3 in the finite element framework in case of the bicrystal. The weak formulation of (4.4) for the two grains can be written as,

$$\begin{aligned} \int_{B_1} \dot{\boldsymbol{\alpha}} : \delta \boldsymbol{\alpha} \, dv &= - \int_{B_1} \mathbf{S} : \text{curl}(\delta \boldsymbol{\alpha}) \, dv + \int_{B_1} \boldsymbol{\Omega} : \text{curl}(\delta \boldsymbol{\alpha}) \, dv \\ \int_{B_2} \dot{\boldsymbol{\alpha}} : \delta \boldsymbol{\alpha} \, dv &= - \int_{B_2} \mathbf{S} : \text{curl}(\delta \boldsymbol{\alpha}) \, dv + \int_{B_2} \boldsymbol{\Omega} : \text{curl}(\delta \boldsymbol{\alpha}) \, dv \end{aligned} \quad (4.9)$$

where, symbol $\delta \boldsymbol{\alpha}$ represents a test function.

Integrating (4.9) by parts,

$$\begin{aligned} \int_{B_1} \dot{\boldsymbol{\alpha}} : \delta \boldsymbol{\alpha} \, dv &= - \int_{B_1} \text{curl} \mathbf{S} : \delta \boldsymbol{\alpha} \, dv - \int_{\partial B_1} (\mathbf{S} \times \mathbf{n}) : \delta \boldsymbol{\alpha} \, da + \\ &\quad \int_{B_1} \text{curl} \boldsymbol{\Omega} : \delta \boldsymbol{\alpha} \, dv + \int_{\partial B_1} (\boldsymbol{\Omega} \times \mathbf{n}) : \delta \boldsymbol{\alpha} \, da \\ \int_{B_2} \dot{\boldsymbol{\alpha}} : \delta \boldsymbol{\alpha} \, dv &= - \int_{B_2} \text{curl} \mathbf{S} : \delta \boldsymbol{\alpha} \, dv - \int_{\partial B_2} (\mathbf{S} \times \mathbf{n}) : \delta \boldsymbol{\alpha} \, da + \\ &\quad \int_{B_2} \text{curl} \boldsymbol{\Omega} : \delta \boldsymbol{\alpha} \, dv + \int_{\partial B_2} (\boldsymbol{\Omega} \times \mathbf{n}) : \delta \boldsymbol{\alpha} \, da \end{aligned} \quad (4.10)$$

Choosing $\delta \boldsymbol{\alpha}$ such that its value is non-zero along the grain boundary and is zero everywhere else, (4.10) reduces to,

$$\begin{aligned} \int_{c_{B_1}} (\mathbf{S} \times \mathbf{n}) : \delta \boldsymbol{\alpha} \, da + \int_{c_{B_2}} (\mathbf{S} \times \mathbf{n}) : \delta \boldsymbol{\alpha} \, da = \\ \int_{c_{B_1}} (\boldsymbol{\Omega} \times \mathbf{n}) : \delta \boldsymbol{\alpha} \, da + \int_{c_{B_2}} (\boldsymbol{\Omega} \times \mathbf{n}) : \delta \boldsymbol{\alpha} \, da \end{aligned} \quad (4.11)$$

Since, $\boldsymbol{\Omega}_1 = \boldsymbol{\Omega}_2 = \mathbf{0}$ and $\mathbf{n}_1 = -\mathbf{n}_2 = \mathbf{n}$, (4.11) can be written as,

$$\int_c (\mathbf{S}_1 \times \mathbf{n}) : \delta \boldsymbol{\alpha} \, da - \int_c (\mathbf{S}_2 \times \mathbf{n}) : \delta \boldsymbol{\alpha} \, da = 0 \quad (4.12)$$

$$\int_c ((\mathbf{S}_1 - \mathbf{S}_2) \times \mathbf{n}) : \delta \boldsymbol{\alpha} \, da = 0 \quad (4.13)$$

As the test functions are arbitrary, (4.13) implies $(\mathbf{S}_1 - \mathbf{S}_2) \times \mathbf{n} = \mathbf{0}$ on c . This corresponds to the implementation of case (a) mentioned above. The plastic flow at the grain boundary cannot be stopped by imposing this condition. Here, the test functions are assumed to be continuous at the grain boundary. However, it is also

possible to use discontinuous test functions. Let the test functions in grains B_1 and B_2 , be $\delta\alpha_1$ and $\delta\alpha_2$, respectively. In this case, (4.12) will change to,

$$\int_c (\mathbf{S}_1 \times \mathbf{n}) : \delta\alpha_1 da - \int_c (\mathbf{S}_2 \times \mathbf{n}) : \delta\alpha_2 da = 0 \quad (4.14)$$

As $\delta\alpha_1$ and $\delta\alpha_2$ are arbitrary, (4.14) allows us to impose the conditions, $\mathbf{S}_1 \times \mathbf{n} = \mathbf{0}$ and $\mathbf{S}_2 \times \mathbf{n} = \mathbf{0}$ on c in the respective grains. This corresponds to the implementation of case (b) mentioned above.

In order to model (4.14) in the finite element framework, two node numbers are assigned to each node of grain boundary (suppose 1 and 2 are the two nodes numbers assigned to a certain node of a grain boundary). All the nodes of a grain boundary are characterized as surface nodes. The following fields are set to be equal on the two nodes (if a grain boundary is considered to have a non-zero thickness, then none of the fields are solved in the elements belonging to that layer),

$$\begin{aligned} \mathbf{u}|_1 &= \mathbf{u}|_2 \\ \mathbf{z}|_1 &= \mathbf{z}|_2 \\ \boldsymbol{\chi}|_1 &= \boldsymbol{\chi}|_2 \end{aligned} \quad (4.15)$$

These conditions (4.15), with $\mathbf{S}_1 \times \mathbf{n} = \mathbf{0}$ and $\mathbf{S}_2 \times \mathbf{n} = \mathbf{0}$ on the interface c , will correspond to the constrained plastic flow case. However, if $\alpha|_1 = \alpha|_2$ is also considered in addition to (4.15) then the grain boundary will allow dislocations to pass through it.

4.4 Test Case: Deformation of a Bicrystal

A simple test is performed to demonstrate the effect of grain boundary constraints on mechanical response and microstructure. Consider a specimen consisting of two grains as shown in Figure 4.1 and discretized by a finite element grid. Orientation of

both grains is considered to be cubic initially. Each grain has a thickness of $0.5\mu m$ and width of $0.5\mu m$. The sample is unstressed and ED free initially.

Material parameters used for this computational experiment are, $b = 2.5 \times 10^{-4} \mu m$, $k_0 = 20$, $m = 0.03$, $g_s = 210 \text{ MPa}$, $g_0 = 50 \text{ MPa}$, $\theta_0 = 205 \text{ MPa}$, $L = 1.0$, and $c = 1.0$. The physical meaning of these parameters is described in Section 2.2. The reference strain rate is $\dot{\gamma}_0 = 1 \text{ sec}^{-1}$. Isotropic elastic constants of the representative material, Copper, are $E = 110 \text{ GPa}$, $\nu = 0.34$, where E is the Young's modulus and ν is the Poisson's ratio.

The imposed initial conditions are as mentioned in Chapter 2. The boundary conditions are applied in the following way: displacements on the left face are constrained in x_1 direction and the face is traction free in x_2, x_3 directions, the right face is also traction free in x_2, x_3 directions, the bottom face is constrained in x_2 direction and traction free in x_1, x_3 directions, the top face is traction free in x_1, x_2, x_3 directions (Figure 4.1). The front face is displacement-constrained in the x_3 direction and traction free in x_1, x_2 direction. The displacements corresponding to a plane strain tension are prescribed through the kinematic boundary condition,

$$u_1(x_1, x_2, x_3, t) = (d - l)\dot{\epsilon}t \quad (4.16)$$

on the nodes of the right face. Here, d is the edge length of specimen in x_1 direction, l is the thickness of grain boundary in x_1 direction, $\dot{\epsilon}$ is an applied tensile strain rate of 1 sec^{-1} , and t is time. All degree of freedoms on the back face is set to be equal to the value of corresponding degree of freedoms on the front face.

In the interpretation of results, notation σ refers to the nominal (reaction) traction on the left face of the simulation cell.

A mesh refinement study is done in order to use an optimum mesh for subsequent simulations. A bicrystal with the grain boundary being impenetrable to dislocations is considered for this purpose. The stress-strain response for meshes of different sizes is shown in Figure 4.2a. Based on this result, a mesh with dimensions 40x15x1 seems reasonable for this particular case. The element size corresponding to this mesh is used in all simulations presented in this section. This is a conservative choice as experience indicates that gradients are largest in the case with most constraints to plastic flow.

First, the effect of constraints on plastic flow through grain boundary on work hardening is studied. Figure 4.2b shows a significant difference in the stress-strain response between the two extreme cases under consideration. The case with constrained grain boundary shows a harder response as compared to the case with penetrable grain boundary. When the grain boundaries are impenetrable to dislocations, plastic flow is restricted which results in the accumulation of excess dislocations along the grain boundary, as shown in Figure 4.3a. The net excess dislocation density in the bicrystal is increased due to this obstruction and consequently results in harder response. However, if we consider, $\alpha|_1 = \alpha|_2$, in addition to (4.15), then the ED distribution is continuous across the grain boundary (Figure 4.3b). There is no obstruction to the flow of dislocations and the result is a softer response.

In the subsequent series of simulations, the orientation of the left crystal in the bicrystal is kept cubic and the right crystal is misoriented by 15 degrees about the X_3 -axis. First the unconstrained grain boundary case is considered. σ at 1% applied strain is plotted against the misorientation angle between the two grains in Figure 4.4(a). The response gets harder with an increase in misorientation angle. When both the crystals have cubic orientation, dislocations can flow easily between the two grains. With an increase in misorientation, dislocation flow between the two grains is decreased and consequently mechanical response gets harder. The maximum work hardening is observed for 45 degree misorientation angle in both cases. The response gets harder with an increase in misorientation angle in the constrained grain boundary case also as shown in Figure 4.4(b). However, in the constrained case the effect of increasing the misorientation is not that dominant as compared to the unconstrained case. High misorientation results in hardening as slip systems get misaligned and plastic flow cannot be transmitted. But if the interface is blocked already this does not have much effect. The difference in σ of constrained and unconstrained case at 1% applied strain is plotted against the misorientation angle in Figure 4.4c. The maximum effect of grain boundary constraints on the mechanical response is observed in case of both grains with cubic orientation. The effect decreases with an increase in misorientation angle.

In all the experiments mentioned above, dislocation sources are considered to be present throughout the body. Next, simulations with dislocation sources localized in the region close to the grain boundary are done. The objective of this set of simulations is to setup a bicrystal with grain boundary acting as the only source of dislocations. Accordingly, as a first approximation, dislocation sources are localized

to a thin layer close to the grain boundary rather than distributed throughout the grains, as shown in Figure 4.5. In this particular case, the left crystal has cubic orientation whereas the right crystal is misoriented by 5° about the X_3 -axis. Material properties, representative of Copper, as mentioned above are used in this case, except the rate sensitivity for non-source regions is used as 1.0 ($= m$), and 0.03 for source regions. *The grain boundary is considered to be impenetrable to dislocations.* Two different thicknesses of the source layer are considered, $0.05\mu m$ and $0.1\mu m$. First, convergence analysis with respect to stress strain response is done for both thicknesses. Comparison of converged result shows that the stress-strain response of the sample depends upon the thickness of the source layer. In order to understand the cause of size-effect in the current framework, dimensional analysis of the nominal stress (reaction) σ is performed which implies the following relation,

$$\sigma = E\Phi\left(\frac{\theta_0}{E}, \frac{g_s}{E}, \frac{g_0}{E}, \frac{\dot{\Gamma}}{\dot{\gamma}_0}, \frac{b}{H}, \alpha_0 H, m, \Gamma, k_0, \eta, \frac{h}{H}\right) \quad (4.17)$$

where, α_0 is a representative measure of the magnitude of the initial ED density field, h is the thickness of source layer, H denotes the dimension of the body and Φ is a dimensionless function of the arguments shown. The dimensionless arguments $b/H, \alpha_0 H, h/H$ introduce a dependence of average response on the Burgers vector of the material, the geometric proportion of the body, the initial ED density and the thickness of source layer. In this series of tests, the response is independent of $\alpha_0 H$ as the specimens were initially ED-free. The argument (b/H) corresponds to the size effects arising from dislocation mobility, (2.65) and strain hardening, (2.66). Thus, it can be concluded from this set of simulations that the size effect observed here is caused by the thickness of the source layer and the natural length scale that enter the theory through the ED velocity and strain hardening.

4.5 Conclusions

A method of modeling plastic flow through grain boundaries has been presented in this chapter which is otherwise absent in the literature. It is evident from the test case of deformation of a bicrystal that different classes of constraints on plastic flow through grain boundaries have a significant effect on the mechanical response and dislocation microstructure development. In the above discussion, only two extreme cases, grain boundaries acting as impenetrable or penetrable to dislocations, are considered. However, if the behavior of grain boundary is known from experimental observations, modeling can be done accordingly using a corresponding expression for Ω .

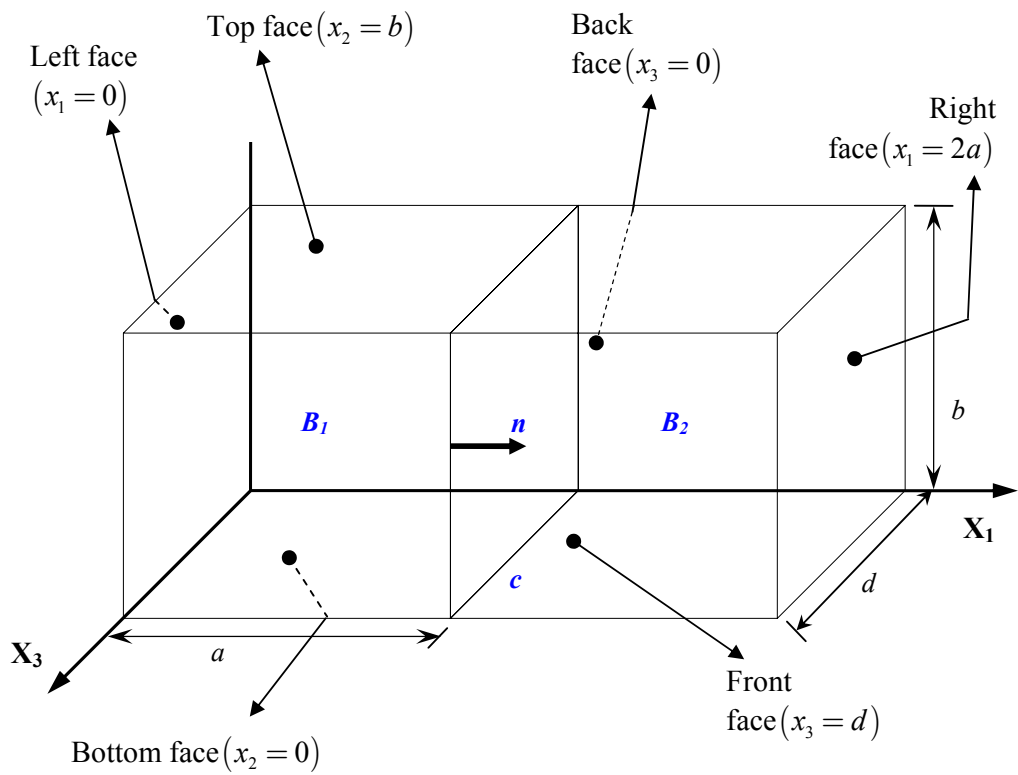


Figure 4.1. Schematic layout of the bicrystal under consideration

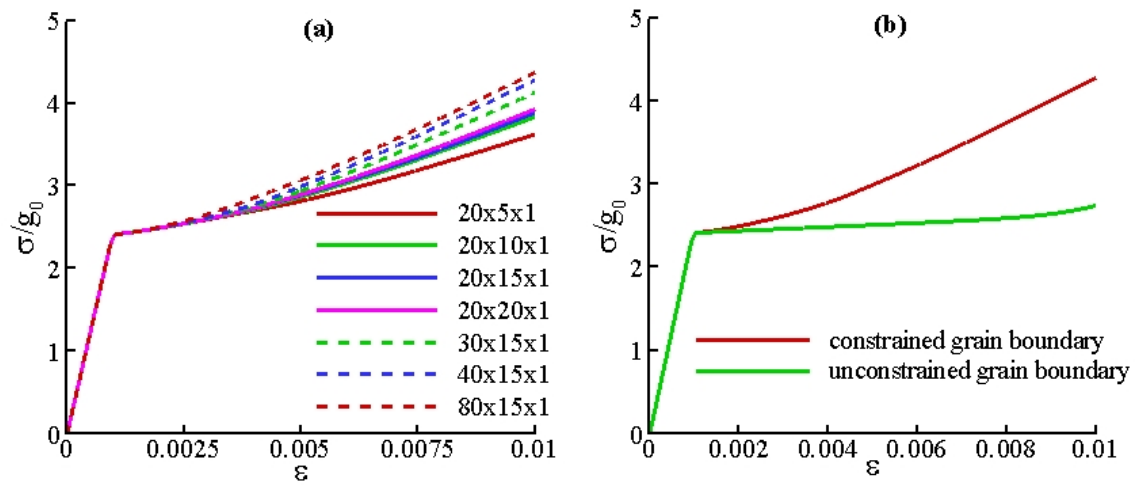


Figure 4.2 (a) Mesh refinement analysis of the bicrystal with constrained grain boundary; (b) Effect of grain boundary constraints on the stress-strain response of a bicrystal with both grains of cubic orientation (g_0 is the initial yield strength)

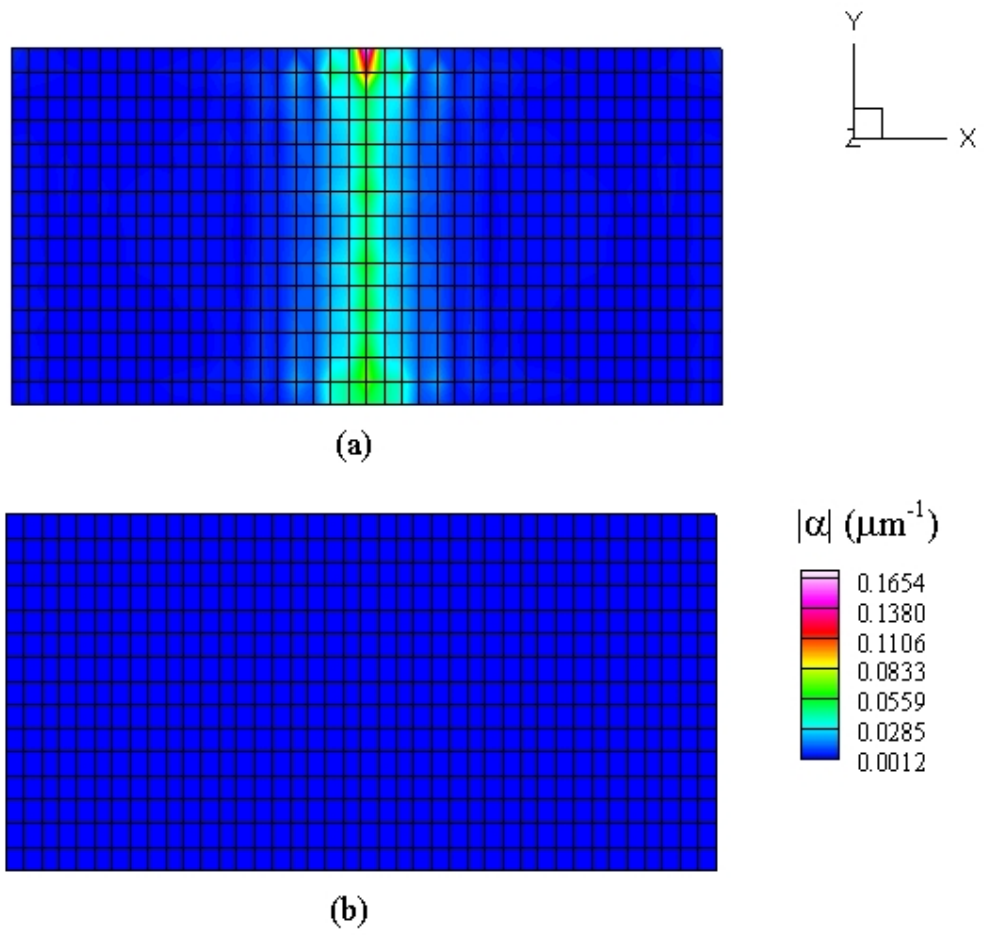


Figure 4.3 Field plot of $|\alpha|$ at 0.2% applied strain, (a) with constrained grain boundary; (b) with unconstrained grain boundary.

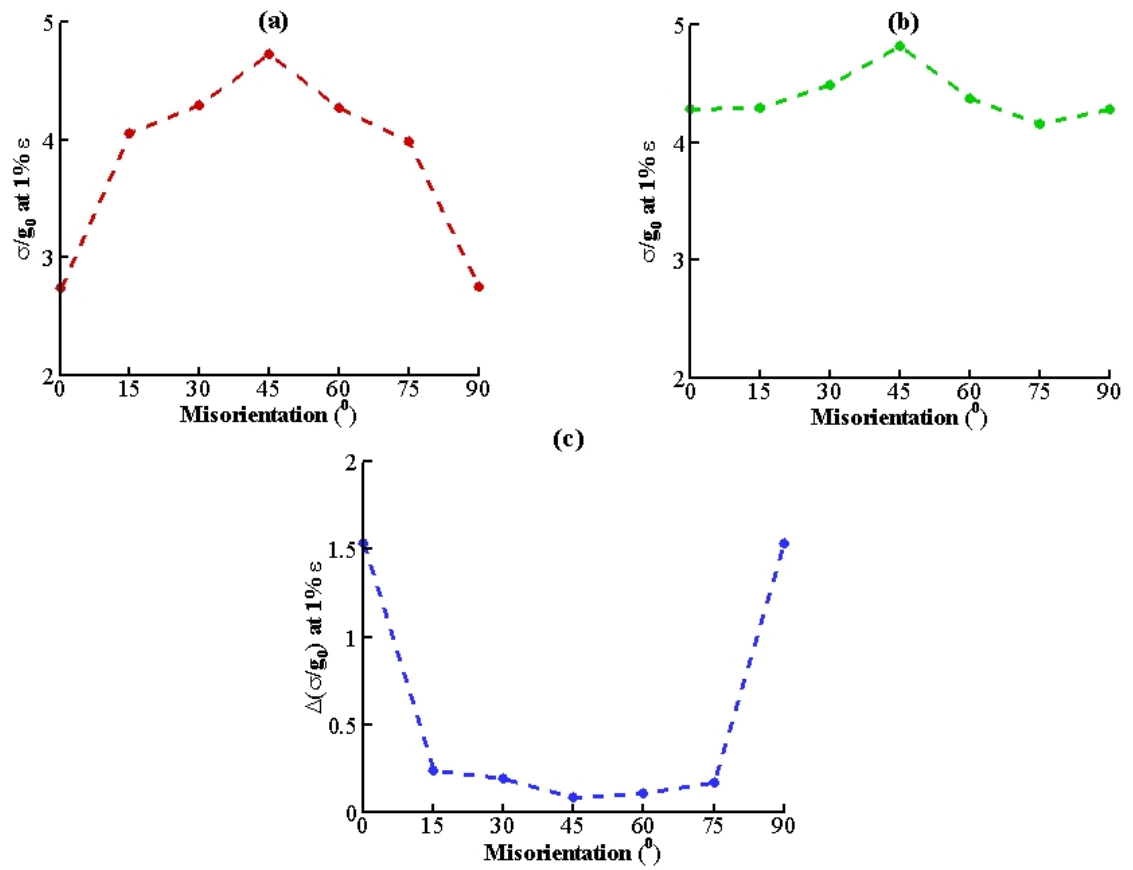


Figure 4.4. Effect of misorientation between the two grains of the bicrystal on the mechanical response, (a) unconstrained grain boundary case, (b) constrained grain boundary, (c) difference between the constrained and unconstrained grain boundary.

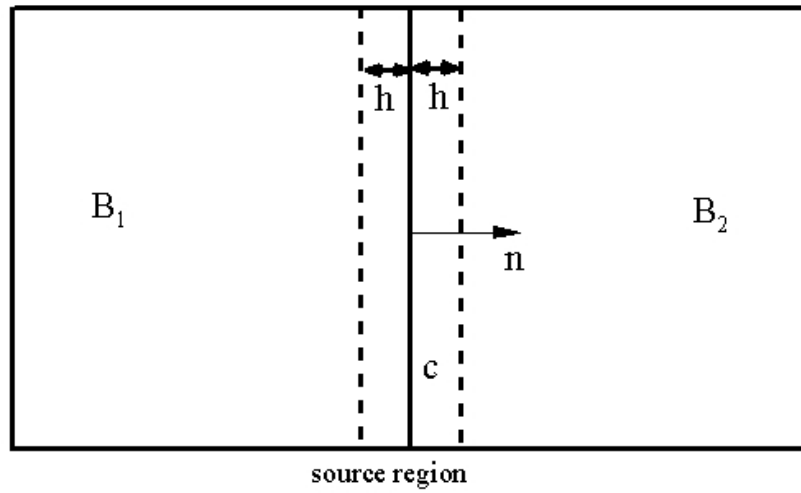


Figure 4.5. Schematic layout of the bicrystal with dislocation sources localized along the grain boundary in a thin layer of width h .

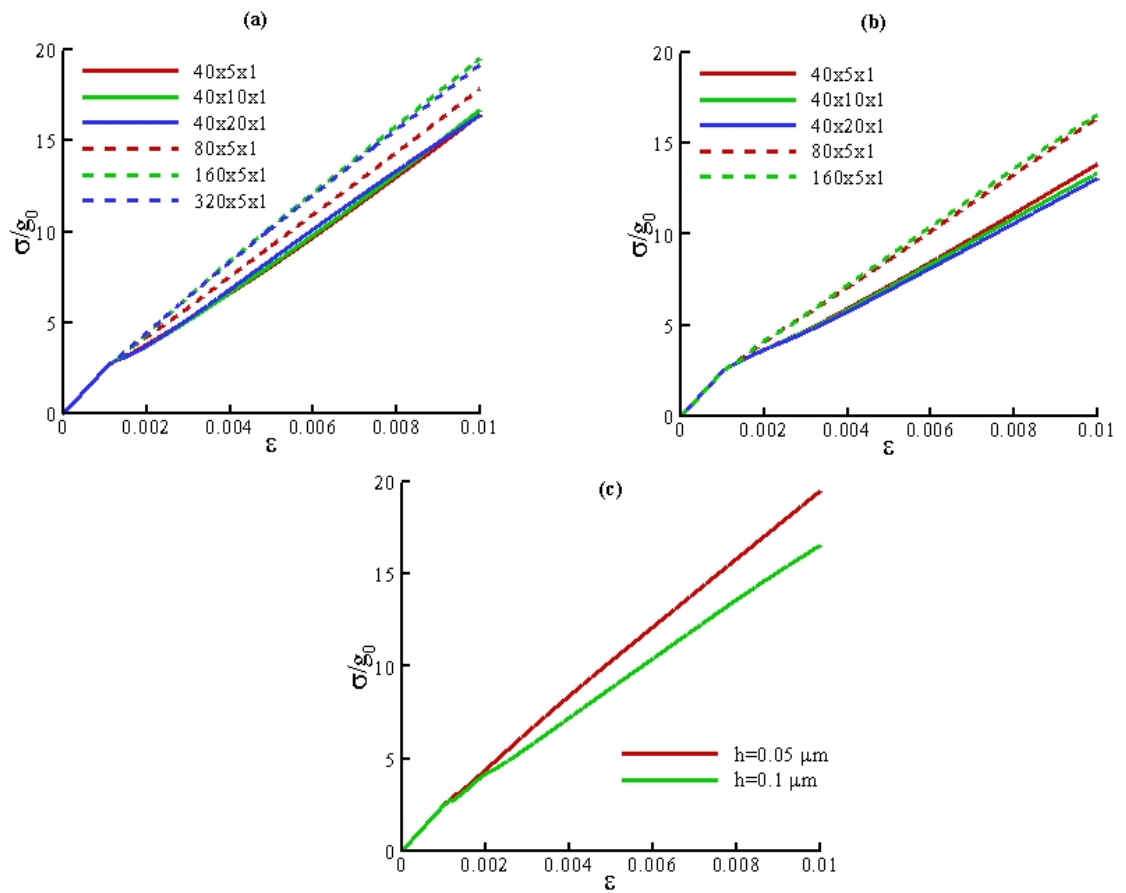


Figure 4.6. (a) Mesh refinement analysis for the case with $h = 0.05 \mu\text{m}$; (b) Mesh refinement analysis for the case with $h = 0.1 \mu\text{m}$; (c) Effect of h on the mechanical response.

CHAPTER 5

PLASTIC DEFORMATION OF MULTICRYSTALLINE THIN FILMS

The mechanical behavior of multicrystalline thin films undergoing plane strain tension is analyzed using *PMFDM* theory motivated by experiments of Xiang and Vlassak (2006). Particularly, the effect of film thickness, grain orientations, and presence/absence of surface passivation on the loading and unloading characteristics is studied. Similar problem was analyzed using strain gradient plasticity theory by Xiang and Vlassak (2006). They were able to model the experimentally observed size effects successfully but not the Bauschinger effect. Lately, Nicola *et al.* (2006) used Discrete Dislocation (DD) technique to model deformation of thin films considering grain boundaries to be impenetrable to dislocations and were successfully able to predict some of the experimentally observed features (Xiang and Vlassak, 2006). A novel feature of our work is to consider the effect of different classes of grain boundary constraints on the mechanical response, which has not been achieved in the modeling of thin films. Also, Nicola *et al.* (2006) performed numerical experiments at very high strain rate to decrease the computation time. *PMFDM* provides a framework to efficiently perform these experiments at reasonable strain rates. However, the expression for plastic strain rate mentioned in Section 2.1 needs to be specified phenomenologically but allows the modeling of mechanical behavior at a realistic relevant strain rate.

Results presented in this chapter are in good qualitative agreement with corresponding experimental observations (Xiang and Vlassak, 2006) and an effort is made to provide a simple physical interpretation for most of them. However, there are certain interesting observations mentioned in this chapter for which we are unable to provide a *simple* explanation.

This chapter is organized as follows: the problem setup is explained in Section 5.1. Section 5.2 involves discussion of results. The chapter ends with some concluding remarks in Section 5.3.

5.1 Problem Setup

For all the simulations mentioned in this chapter, a multocrystal consisting of four grains as shown in Figure 5.1 is used. Samples are unstressed and ED free initially. Each grain has a thickness h and width d . Two different values of h are used, $h = 0.35\mu m$ and $h = 1.4\mu m$ and d is set to be equal to $0.33\mu m$. c shown in Figure 5.1 is set to be equal to $0.5\mu m$. Cases with passivation on both surfaces, and with no surface passivation are considered. Three different sets of orientation of grains in the multocrystal are considered:

1. Misorientation between adjacent grains is 3-5 degrees about the X_3 -axis,
2. Misorientation between adjacent grains is 20-30 degrees about the X_3 -axis, and
3. In the third case, 12 slip systems are oriented such that a (111) plane is parallel to the X_1 - X_2 plane. Misorientation between adjacent grains is 3-5 degrees about the X_2 -axis.

Material parameters representative of Copper are used for all the computational experiments presented in this chapter; $b = 2.5 \times 10^{-4} \mu\text{m}$, $m = 0.03$, $g_s = 210 \text{ MPa}$, $g_0 = 50 \text{ MPa}$, $\theta_0 = 205 \text{ MPa}$, $k_0 = 20.0$, $L = 100$, and $c = 100$. The physical meaning of these parameters is described in Chapter 2. The reference strain rate is $\dot{\gamma}_0 = 1 \text{ sec}^{-1}$. Isotropic elastic constants of the representative material are $E = 110 \text{ GPa}$, $\nu = 0.34$, where E is the Young's modulus and ν is the Poisson's ratio. The *passivation layer(s) is considered as elastic* with elastic constants representing Silica with $E = 70 \text{ GPa}$, and $\nu = 0.17$. The thickness of the passivation layer is set to $0.02 \mu\text{m}$ in all simulations.

The imposed initial conditions are as mentioned in Chapter 2. The boundary conditions are applied in the following way (Figure 5.1): displacements on the left face are constrained in x_1 direction; the face is traction free in x_2, x_3 directions. The right face is also traction free in x_2, x_3 directions. The bottom face is constrained in the x_2 direction and traction free in x_1, x_3 directions and the top face is traction free in x_1, x_2, x_3 directions. The front face is displacement-constrained in the x_3 direction and traction free in x_1, x_2 directions. The displacements corresponding to a plane strain tension are prescribed through the kinematic boundary condition,

$$u_1(x_1, x_2, x_3, t) = (d - l)\dot{\epsilon}t \quad (5.1)$$

on the nodes of the right face. Here, d is the edge length of specimen in x_1 direction, l is the thickness of grain boundary in x_1 direction, $\dot{\epsilon}$ is an applied tensile strain rate of 1 sec^{-1} , and t is time. In order to do a two dimensional problem in the current setup, all degree of freedoms on the back face are set to be equal to the value of

corresponding degree of freedoms on the front face. The boundary conditions corresponding to grain boundary constrained and unconstrained cases are used as mentioned in Chapter 4. All components of the excess dislocation density (α) on the left external face are set to be equal to the components of corresponding nodes on the right face. This implies that the dislocation flow on the right face is equal and opposite to that on left face.

$$\alpha|_L = \alpha|_R \quad (5.2)$$

Constitutive expressions corresponding to crystal plasticity, mentioned in Chapter 4, are used in this work. In the interpretation of results, in order to remove the contribution of passivation layers from the flow stress, the volume average of 11 component of stress σ , over the elastic-plastic elements is plotted against applied strain ε .

A mesh refinement study is done in order to use an optimum mesh for subsequent simulations. Convergence check is done for the thin film of thickness $0.35\mu m$ with surface passivation on both sides and grain boundaries being impenetrable to dislocations. The average stress-strain response for meshes of different sizes is shown in Figure 5.2 (a). The element size corresponding to the mesh with dimensions $16 \times 14 \times 1$ was chosen for this case. Average stress seems to be increasing with mesh refinement. An upper bound to the stress at 1% applied strain is estimated using extrapolation as shown in Figure 5.2 (b). The linearly extrapolated stress at 1% applied strain for zero element size is 0.75 GPa. It is higher by 10% than the corresponding stress for the mesh size used in all simulations in this chapter. The element size corresponding to this case is used in all simulations irrespective of the

physical dimensions of thin film. This is a conservative choice as experience indicates that gradients are largest in the thinnest case with most obstruction to plastic flow.

5.2 Results and Discussions

The effect of surface passivation, thickness and grain boundary constraints on the loading and unloading characteristics of thin films is discussed in the following subsections.

5.2.1 Effect of Passivation

5.2.1.1 Loading: It is observed experimentally that the presence of a passivation layer makes the stress-strain response harder as compared to that of unpassivated films (Xiang and Vlassak, 2006). In order to model this behavior, numerical experiments were performed in the context of conventional plasticity theory initially. Conventional plasticity may be recovered from PMFDM by setting $\alpha = 0$ for all times and replacing (2.9)₄ with,

$$\mathbf{U}^e = \text{grad } \mathbf{u} - \mathbf{U}^p ; \dot{\mathbf{U}}^p = \mathbf{L}^p \quad (5.3)$$

It is found that in conventional plasticity the stress-strain response is independent of the presence/absence of passivation layers as shown in Figure 5.3 (a), (b). This is due to the absence of an explicit characterization of dislocations in the conventional plasticity framework. The same numerical experiment is now performed using *PMFDM* theory. Initially, grain boundaries are considered to be penetrable to dislocations. Figure 5.3 (c), (d) shows a significant difference in the stress-strain response between passivated and unpassivated films for both thicknesses. This is due to the accumulation of

excess dislocations along the passivation layer in the specimen as shown in Figure 5.5(a), (b) and the theory allows for greater hardening at material points with higher value of ED. A thick layer of dislocations is formed along the passivation layer which acts as an obstruction to plastic flow and hence results in a harder response. No such layer is formed in case of unpassivated films as observed in Figure 5.5 (c), (d).

Next, similar tests are done considering grain boundaries to be impenetrable to dislocations. Films with surface passivation layers show a harder response in this case also (Figure 5.3 (e), (f)). However, the difference between the passivated and unpassivated case is less here as compared to the grain boundary unconstrained case. The reason for this behavior is that constraints on plastic flow through grain boundary result in the accumulation of dislocations along them as observed in Figure 5.5 (a), (c) and consequently decreases the relative effect of passivation layer on stress-strain behavior.

Similar simulations were done for three different sets of orientations mentioned in Section 5.2. The volume average of the 11 component of σ at 1% applied strain for different orientations is plotted in Figure 5.6. Similar trends as mentioned above are observed for all three sets of orientations. However, the difference between the stress-strain response of passivated and unpassivated films changes significantly with orientation.

5.2.1.2 Unloading/Bauschinger Effect: The main interest here is to analyze the Bauschinger effect during subsequent cycles of loading and unloading of

multicrystalline thin films undergoing plane strain tension. It is observed experimentally that passivated films show an unusual Bauschinger effect as compared to the films with no surface passivation (Xiang and Vlassak, 2006). The effect is not observed in the framework of conventional plasticity as shown in Figure 5.3 (a), (b). Corresponding numerical experiments are done in the context of PMFDM theory to analyze this behavior. Figure 5.3 (c)-(f) shows a strong Bauschinger effect in passivated films as compared to unpassivated films. To better analyze it, the reverse plastic strain at the end of each unloading cycle is plotted against the pre-strain (at which unloading starts in every cycle) in Figure 5.7.

Orientation set 1 is considered first. For $h = 0.35\mu m$ and penetrable grain boundaries, there is a significant effect of surface passivation on unloading behavior as observed in Figure 5.7(a). In case of film with no passivation, zero reverse plastic strain was observed in first cycle and relatively little in subsequent cycles. Similar trends are observed for impenetrable grain boundaries also. However, the effect of passivation is less dominant in this case as compared to the case with unconstrained grain boundaries. The difference in magnitude of reverse plastic strain between passivated and unpassivated cases for $h = 1.4\mu m$ is less than that for $h = 0.35\mu m$.

In case of orientation set 2, similar observations are made (Figure 5.7(b)); however, orientation set 3 shows some deviation in case of impenetrable grain boundaries (Figure 5.7(c)). For the constrained grain boundary case, there is not a significant difference in Bauschinger effect due to passivation. These

numerical experiments show that the unloading behavior of thin films depends significantly on grain orientations.

To better analyze this behavior, two special cases are considered for orientation set 1 and $h = 0.35\mu m$. The mechanical response of films with (a) surface passivation and impenetrable grain boundaries, and (b) no passivation layer and penetrable grain boundaries, is compared on unloading at different strain levels instead of doing cycles of loading and unloading. It is evident from Figure 5.8(a), that both side passivated film shows a very strong Bauschinger effect at all strain levels. Also, the plot of reverse plastic strain versus pre-strain is a straight line with zero slope in the beginning in the case of unpassivated film (Figure 5.8(b)).

5.2.2 Effect of Thickness (Size Effect)

5.2.2.1 Loading: In plane strain bulge tests done by Xiang and Vlassak (2006), passivated films show a very strong dependence of mechanical response on the thickness of films with thinner being stronger, whereas behavior of unpassivated films is observed to be independent of thickness. In order to model this behavior, two films with thicknesses of $h = 0.35\mu m$ and $h = 1.4\mu m$ are considered. Since there is no length scale in conventional plasticity, this behavior cannot be modeled using it, as shown in Figure 5.9(a), (b). Similar numerical experiments are now performed using *PMFDM*. First, grain boundaries are considered to be penetrable to dislocations. In this case, a significant difference in stress-strain response is observed in films with surface passivation on top and bottom as shown in

Figure 5.9 (c). Figure 5.10(a), (b) shows the field plot of $|\alpha|$ at 0.6% applied strain for the films passivated on both sides and unconstrained grain boundaries. The x_2 co-ordinate is scaled by film thickness. It is evident from this figure that the thickness of dislocation layer along top and bottom surface passivation is more than double for the thinner film in comparison to thick film. The thickness of this layer (in scaled co-ordinates) decreases with an increase in film thickness. Clearly, the greater relative volume covered by this layer in the case of the thin film provides more work hardening as well as back stress representing microscopic internal stress effects not encapsulated in the internal stress field of α . In case of unpassivated films, response seems to be independent of the thickness (Figure 5.9(d)) as observed in experiments.

Next, similar simulations with grain boundaries being impenetrable to dislocations were performed. Both side passivated films show a significant size effect with thinner being stronger (Figure 5.9(e)). A almost negligible reverse size effect is observed in case of unpassivated films (Figure 5.9(f)). The main observation in this case is that the effect of thickness in passivated films is dominant in case of penetrable grain boundaries as compared to impenetrable grain boundaries. Similar trends as above were observed for different orientations of grains, however, the magnitude of difference in stress between films of different thicknesses varies significantly with grain orientation (Figure 5.11).

5.2.2.2 Unloading/Bauschinger Effect: It is observed in experiments that the magnitude of reverse plastic strain increases on decreasing film thickness.

This particular characteristic is initially analyzed for the orientation set 1. Classical plasticity shows similar unloading response for films of different thicknesses as shown in Figure 5.9(a), (b). In the context of *PMFDM* theory, thinner *passivated* films show higher Bauschinger effect (Figure 5.7(a)). For the unpassivated films with penetrable grain boundaries, thickness has a very negligible effect on the unloading behavior, whereas in case of constrained grain boundaries, thicker films show a higher Bauschinger effect. The slope of the plot of reverse plastic strain against pre-strain is almost constant for films of different thicknesses as observed in experiments.

For the orientation set 2, Bauschinger effect decreases with an increase in thickness in passivated films whereas it seems to be independent of thickness for the unpassivated films. (Figure 5.7(b)).

For the orientation set 3, unloading behavior is independent of film thickness in all cases except for passivated films with unconstrained grain boundaries. They show a reasonable size effect in unloading with thinner films having a higher magnitude of reverse plastic strain (Figure 5.7(c)).

5.2.3 Effect of Grain Boundary Constraints

5.2.3.1 Loading: The effect of constraints on plastic flow through grain boundaries on mechanical behavior is discussed in this sub-section. Since dislocations are not explicitly characterized in the framework of conventional crystal plasticity, this particular feature cannot be modeled in that context. The details of modeling it in the *PMFDM* theory are explained in Chapter 4.

First, a film with no surface passivation and $h = 0.35\mu m$ is considered. Figure 5.12(b) shows a significant difference in the stress-strain response between the constrained and unconstrained grain boundary case. The case with constrained grain boundaries shows a harder response as compared to the case with unconstrained grain boundaries. When the grain boundaries are impenetrable to dislocations, plastic flow is restricted which results in the accumulation of excess dislocations along the grain boundary, as shown in Figure 5.5(c). The net excess dislocation density in the thin film is increased due to this obstruction and consequently results in harder response. Similar behavior is observed in unpassivated film with $h = 1.40\mu m$ as shown in Figure 5.12(d). However, the difference in $\sigma = \langle \sigma_{11} \rangle$ between the constrained and unconstrained grain boundary case is higher for $h = 1.40\mu m$ in comparison to that for $h = 0.35\mu m$ (Figure 5.12(d),(b)).

For $h = 0.35\mu m$, the response seems to be independent of grain boundary constraints in the film with surface passivation on both sides (Figure 5.12(a)). This is because in this case, thickness of the layer of dislocations formed along the passivation layer is of the range of film thickness as observed in Figure 5.5(a), (b). Thus the effect of grain boundary constraints is nullified. However, in the passivated film with $h = 1.40\mu m$, $\sigma = \langle \sigma_{11} \rangle$ at 1% applied strain in the constrained grain boundary case is 1.2 times to that of the film with unconstrained grain boundaries, as shown in Figure 5.12(c). Therefore, it

seems that the effect of grain boundary constraints on the mechanical response increases with an increase in thickness.

Similar trends were obtained for other two sets of orientations as shown in Figure 5.13. However, the effect of grain boundary constraints on the stress strain behavior decreases on increasing the misorientation between adjacent grains from 3-5 degrees about Z-axis in set 1 to 20-30 degrees in set 2. This is due to the fact that plastic flow through a grain boundary decreases on increasing the misorientation between adjacent grains. Thus, a grain boundary with a higher misorientation acts as a blockage to the flow of dislocations and consequently not much difference is observed between the constrained and unconstrained case.

5.2.3.2 Unloading/Bauschinger Effect: The effect of constraints on plastic flow through grain boundaries on the unloading behavior is discussed in this subsection. For the orientation set 1, a significant difference in the magnitude of reverse plastic strain is observed in films with no surface passivation as compared to the passivated films (Figure 5.7(a)). It is higher for impenetrable grain boundaries as compared to penetrable grain boundaries. However, the effect is dominant for $h = 1.4\mu m$ in comparison to $h = 0.35\mu m$. Bauschinger effect seems to be independent of grain boundary constraints in the case of passivated films.

In case of orientation set 2, response seems to be independent of the constraints on plastic flow through grain boundaries irrespective of film thickness and presence/absence of passivation layer (Figure 5.7(b)).

In orientation set 3, similar trends as obtained for orientation set 1 are observed except that in this case reverse plastic strain is significantly higher for the constrained grain boundary case with $h = 1.4\mu m$ (Figure 5.7(c)).

5.2.4 Other Observations

It is observed from the set of numerical experiments performed in this chapter that the effect of surface passivation layer on the mechanical response decreases with an increase in the thickness of films. This is shown more clearly in Figure 5.4 for penetrable grain boundaries. The difference in $\sigma = \langle \sigma_{11} \rangle$ between passivated and unpassivated films is higher for $h = 0.35\mu m$ (Figure 5.4 (i),(iii)) as compared to that for $h = 1.40\mu m$ (Figure (ii),(iv)). Similar behavior is observed in the case of impenetrable grain boundaries (Figure 5.3 (e),(f)).

5.3 Conclusions

It is shown from the numerical experiments mentioned in this chapter that in the context of *PMFDM* theory, accumulation of dislocations along surface passivation layers result in a relatively (a) stiffer mechanical response, (b) thickness dependency of stress-strain response, and (c) significant Bauschinger effect in passivated films as compared to corresponding characteristics in unpassivated films. Also, constraints on

plastic flow through grain boundary have a significant influence on size effect and Bauschinger effect. The results appear to be in good qualitative agreement with experimental observations (Xiang and Vlassak, 2006). However, the curvature of the stress-strain curves from experiments and simulations are different (a feature also shared by results from Discrete Dislocation model (Nicola *et al.*, 2006)). This is a current shortcoming and needs to be fixed in the future.

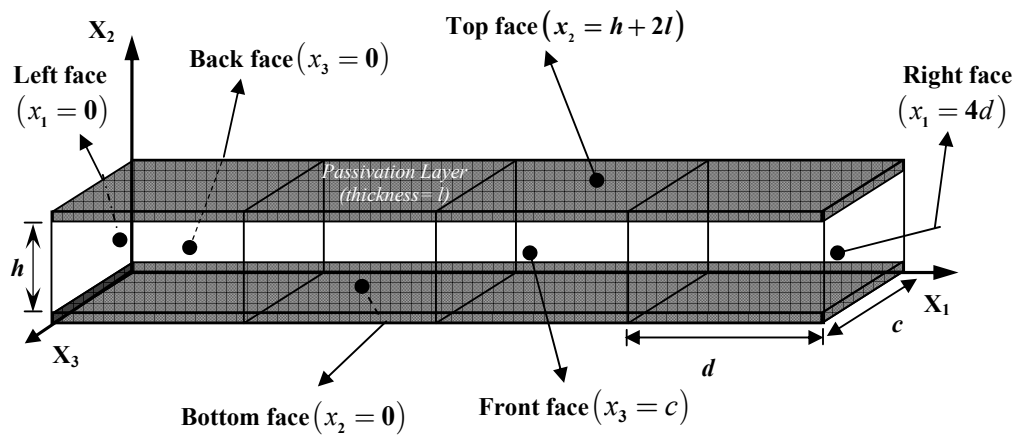
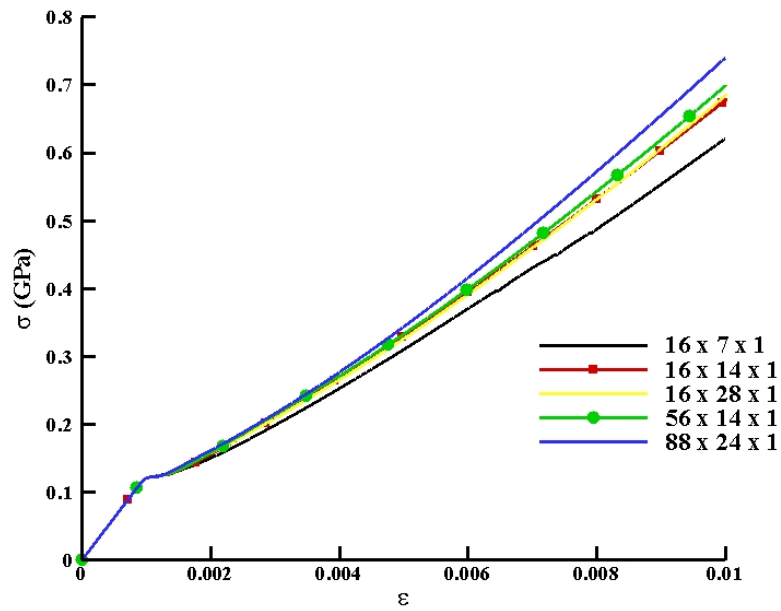
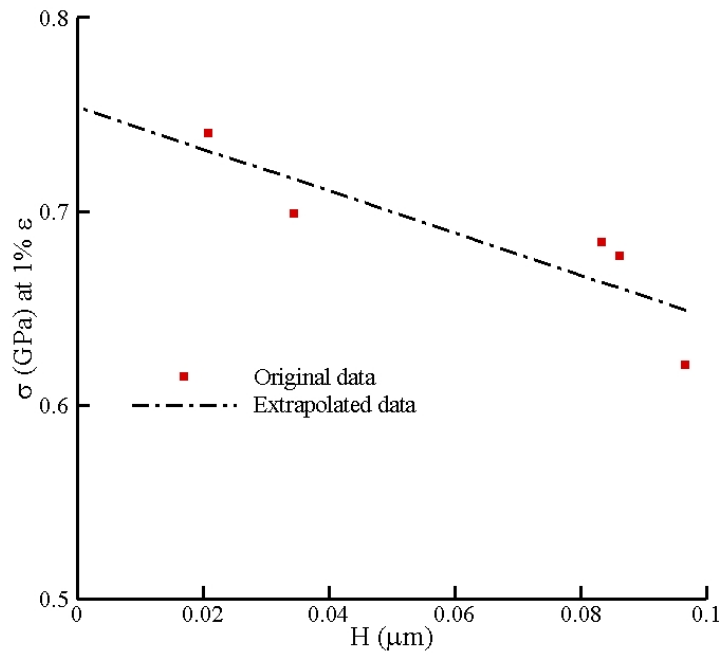


Figure 5.1. Schematic layout of typical model geometry (shaded portion represents the passivation layer)



(a)



(b)

Figure 5.2. Convergence analysis for the film passivated on both sides and grain boundaries being impenetrable to dislocations; (a) stress-strain plot; (b) stress at 1% applied strain plotted against $H (= \sqrt{h^2 + d^2})$.

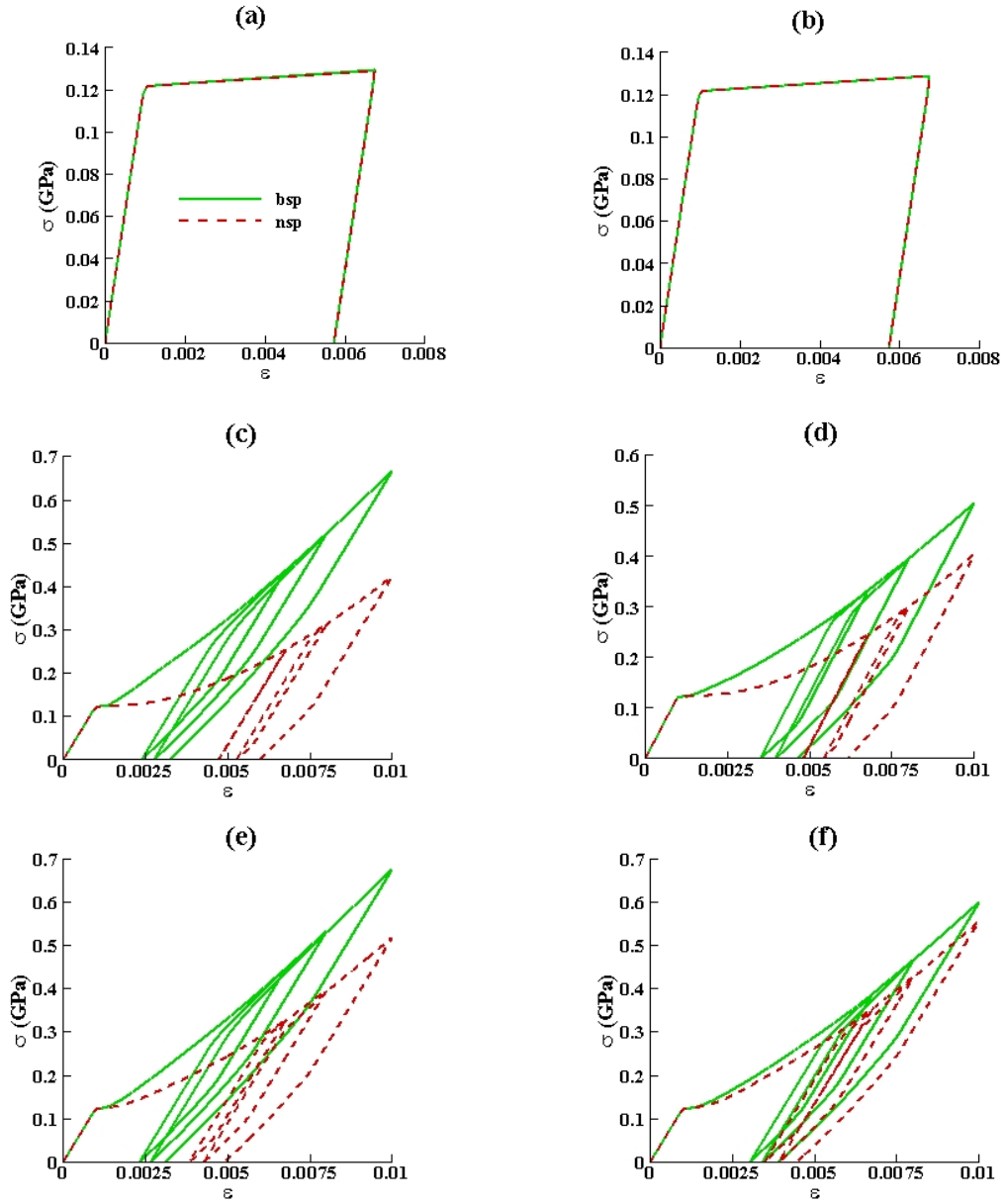


Figure 5.3. Effect of surface passivation on the stress-strain behavior of thin films undergoing cyclic loading; (a) $h = 0.35\mu m$, conventional plasticity; (b) $h = 1.40\mu m$, conventional plasticity; (c) $h = 0.35\mu m$, unconstrained grain boundaries, *PMFDM*; (d) $h = 1.40\mu m$, unconstrained grain boundaries, *PMFDM*; (e) $h = 0.35\mu m$, constrained grain boundaries, *PMFDM*; (f) $h = 1.40\mu m$, constrained grain boundaries, *PMFDM*. (*bsp*- both side passivated; *nsp*- no side passivated)

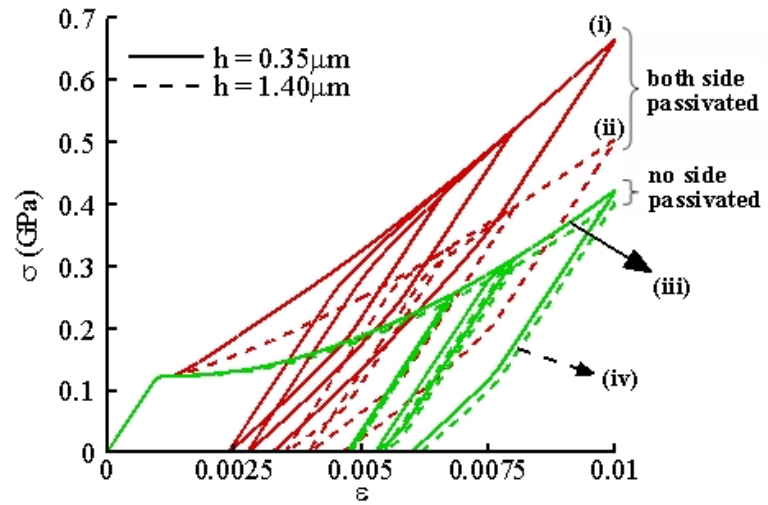


Figure 5.4. Stress-strain behavior of thin films undergoing cyclic loading (grain boundaries are unconstrained)

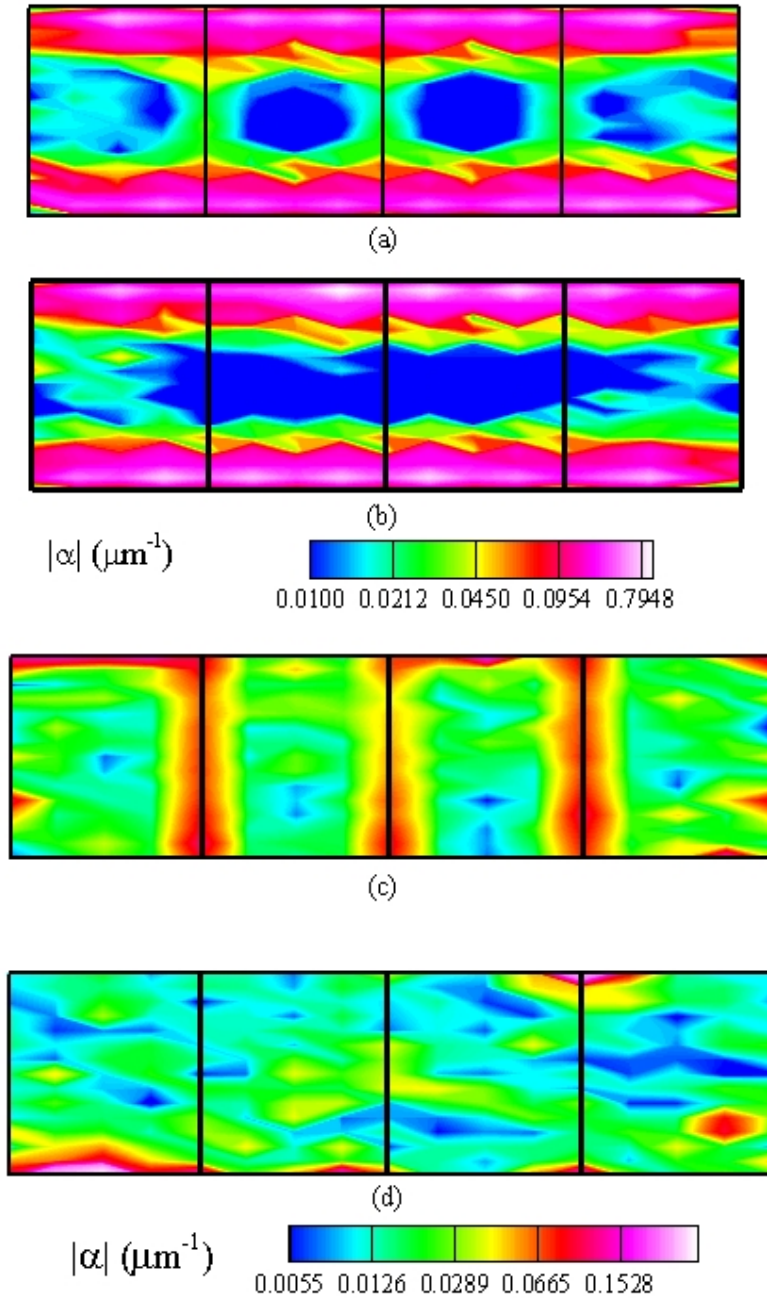


Figure 5.5. Field plot of $|\alpha|$ at 0.6% applied strain for $h = 0.35\mu\text{m}$; (a) both side passivated and constrained grain boundary, (b) both side passivated and unconstrained grain boundary, (c) no side passivated and constrained grain boundary, (d) no side passivated and unconstrained grain boundary. Figures (a) and (b) are plotted using same contour levels; Figures (c) and (d) are plotted using same contour levels.

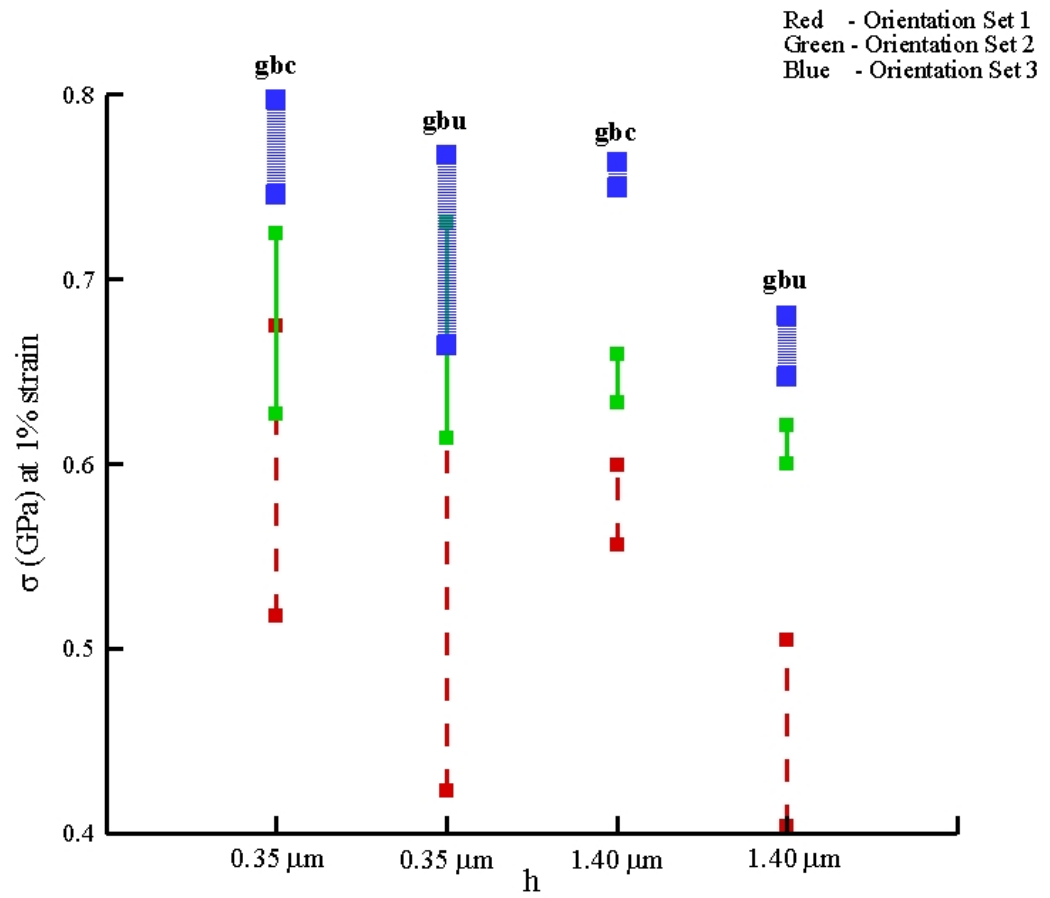


Figure 5.6. Effect of surface passivation on the stress-strain behavior of thin films for different orientation sets (For each line, bottom point represents unpassivated case and top point represents both side passivated case; *gbc*- grain boundary constrained; *gbu*- grain boundary unconstrained)

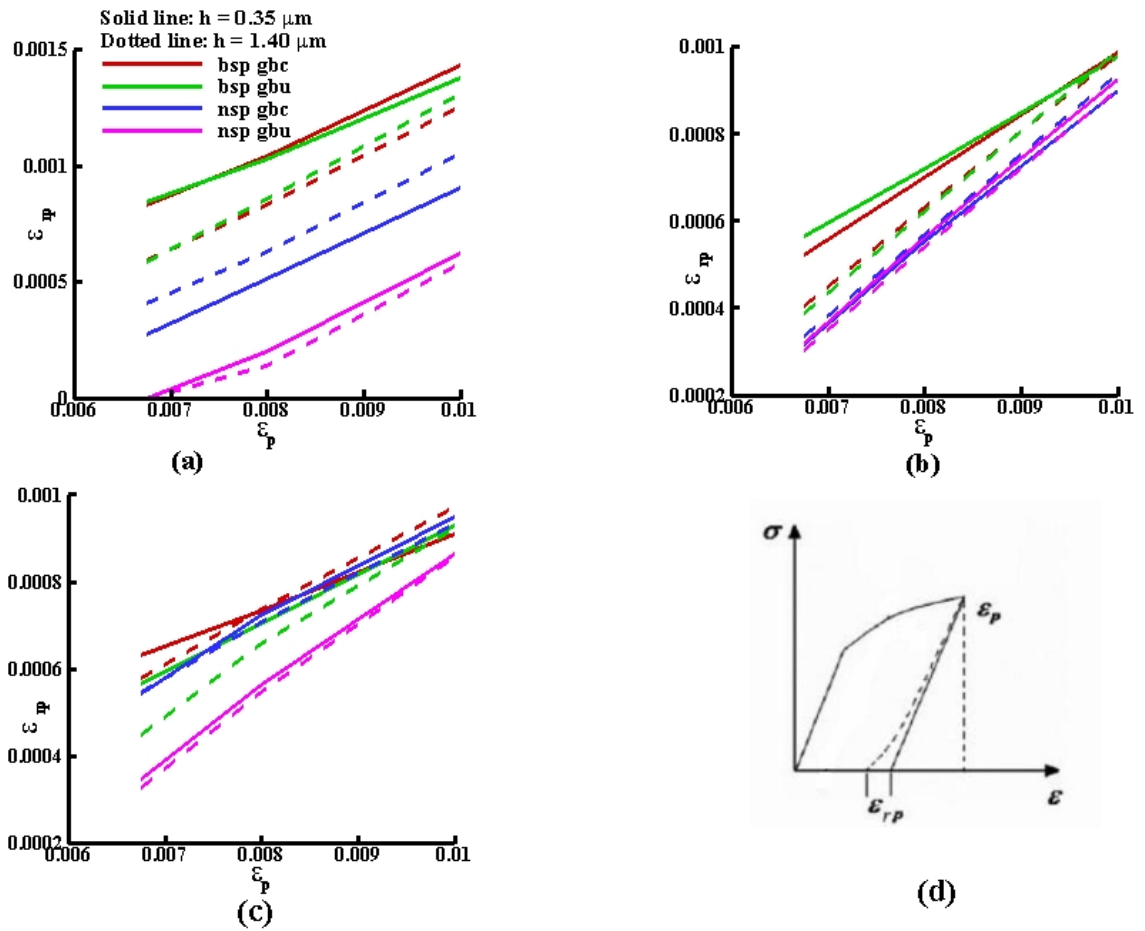


Figure 5.7. Effect of subsequent cycles of loading and unloading on Bauschinger effect; (a) Orientation set 1; (b) Orientation set 2; (c) Orientation set 3; (d) Schematic for defining reverse plastic strain (ϵ_{rp}) and pre-strain (ϵ_p) (after Xiang and Vlassak, 2006) (*bsp*- both side passivated; *nsp*- no side passivated; *gbc*- grain boundary constrained; *gbu*- grain boundary unconstrained).

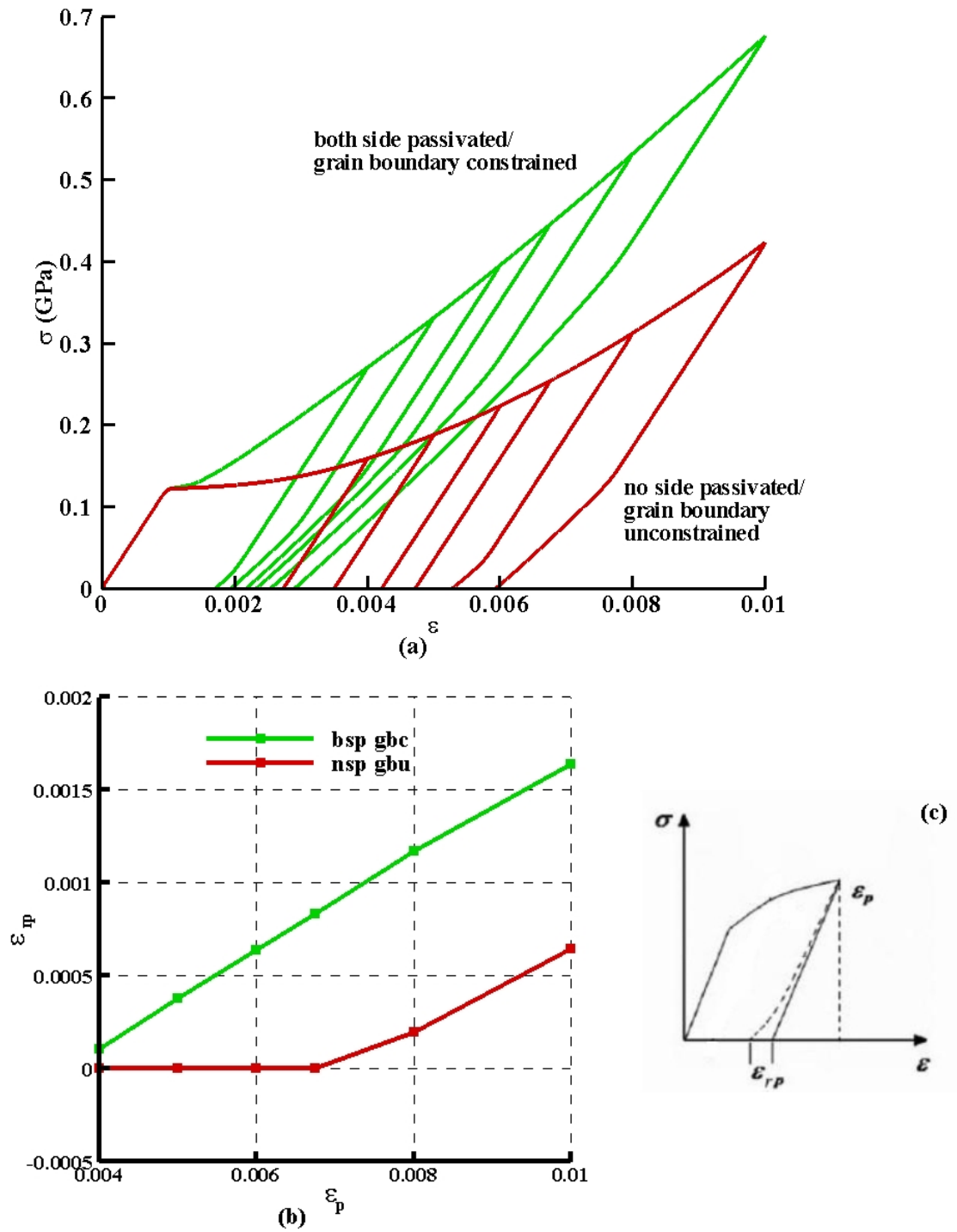


Figure 5.8. (a) Stress-strain behavior and (b) Bauschinger effect in thin films on unloading at different strain levels for $h = 0.35 \mu\text{m}$; (c) Schematic for defining reverse plastic strain (ϵ_{rp}) and pre-strain (ϵ_p) (after Xiang and Vlassak, 2006) (**bsp**- both side passivated; **nsp**- no side passivated; **gbc**- grain boundary constrained; **gbu**- grain boundary unconstrained).

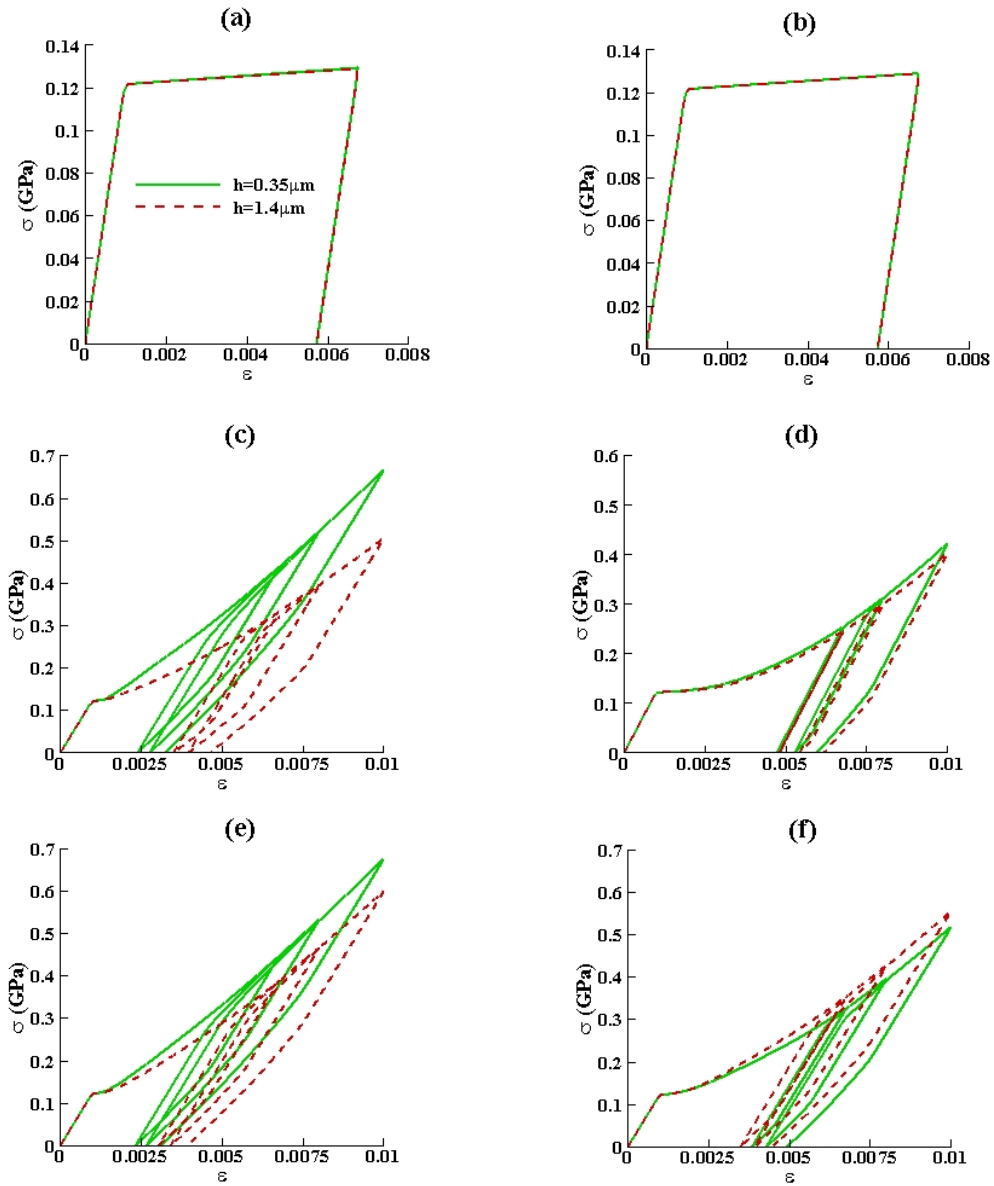


Figure 5.9. Effect of film thickness on the stress-strain behavior of films undergoing cyclic loading; (a) both side passivated, conventional plasticity; (b) no side passivated, conventional plasticity; (c) both side passivated, unconstrained grain boundaries, *PMFDM*; (d) no side passivated, unconstrained grain boundaries, *PMFDM*; (e) both side passivated, constrained grain boundaries, *PMFDM*; (d) no side passivated, constrained grain boundaries, *PMFDM*.

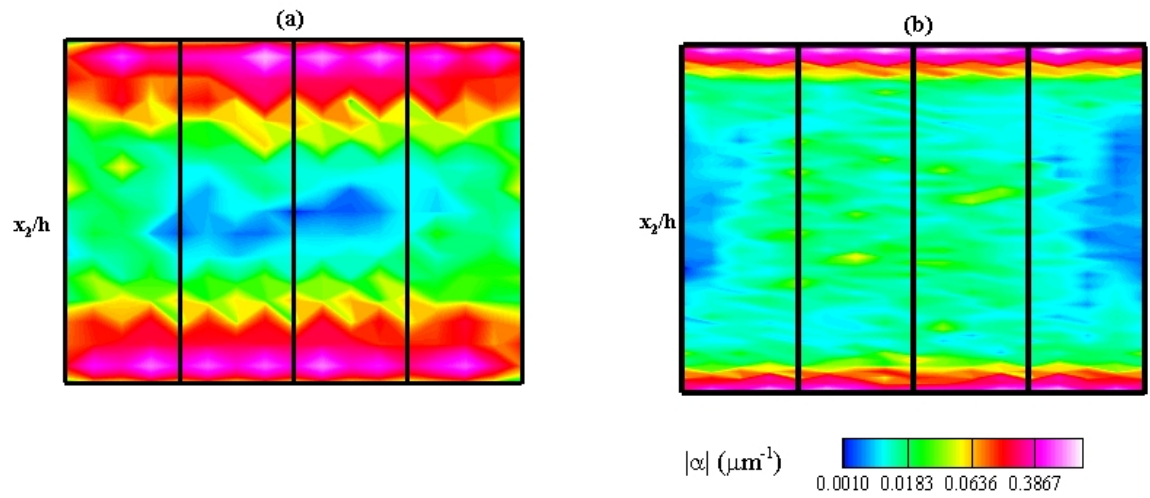


Figure 5.10. Field plot of $|\alpha|$ at 0.6% applied strain for both side passivated and unconstrained grain boundaries case; (a) $h = 0.35 \mu\text{m}$ and (b) $h = 1.40 \mu\text{m}$. X_2 -coordinate in both films is normalized by their thickness.

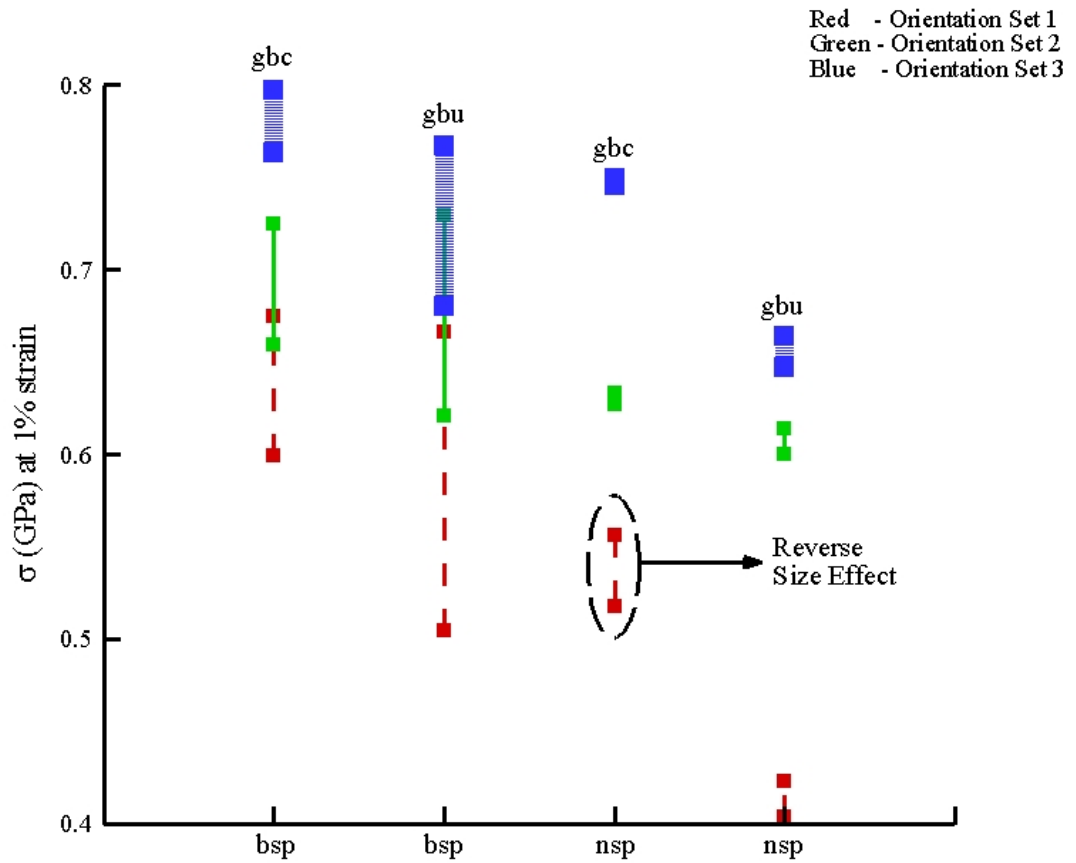


Figure 5.11. Effect of film thickness on the stress-strain behavior for different orientation sets (For each line, bottom point represents $h = 1.40\mu m$ and top point represents $h = 0.35\mu m$, except in no side passivated/grain boundary constrained case; **bsp**- both side passivated; **nsp**- no side passivated; **gbc**- grain boundary constrained; **gbu**- grain boundary unconstrained).

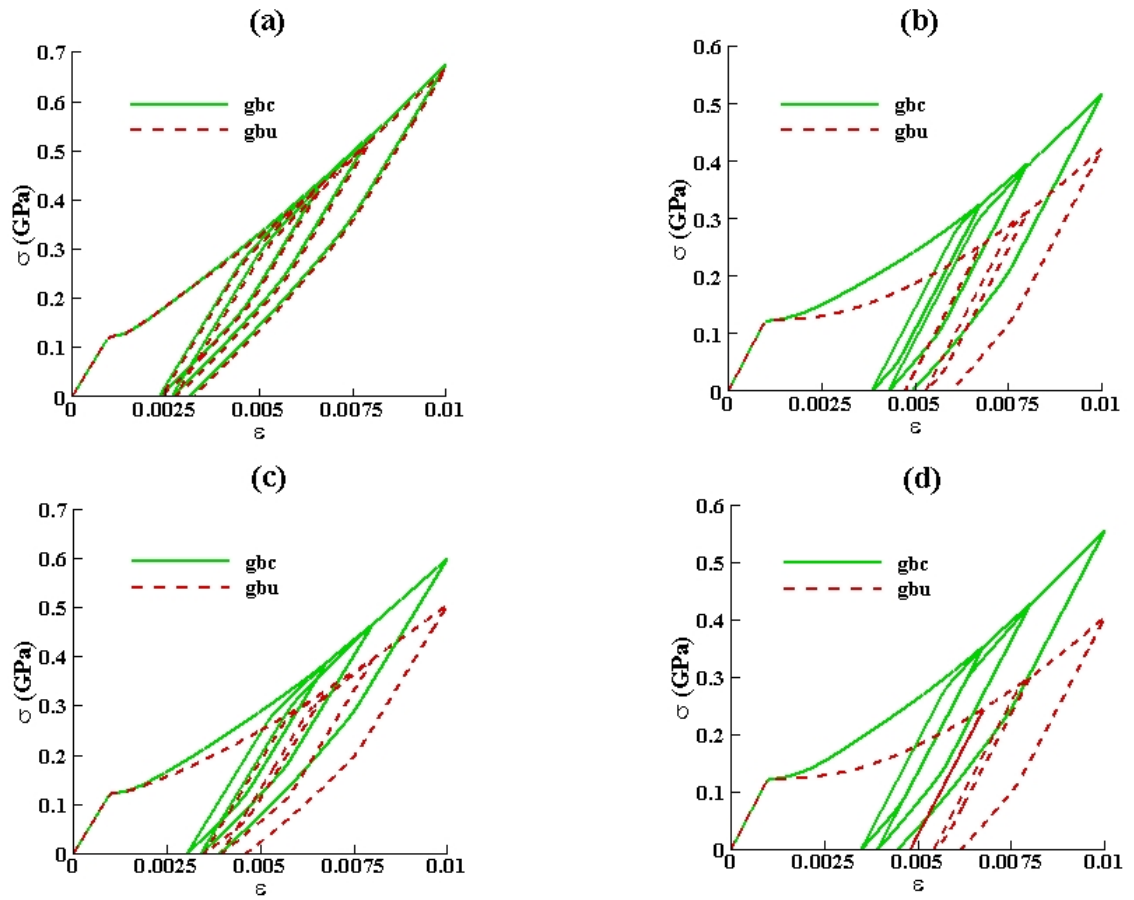


Figure 5.12. Effect of grain boundary constraints on the stress-strain behavior of films undergoing cyclic loading; (a) $h = 0.35\mu\text{m}$, both side passivated; (b) $h = 0.35\mu\text{m}$, no side passivated; (c) $h = 1.40\mu\text{m}$, both side passivated; (d) $h = 1.40\mu\text{m}$, no side passivated (**gbc**- grain boundary constrained; **gbu**- grain boundary unconstrained).

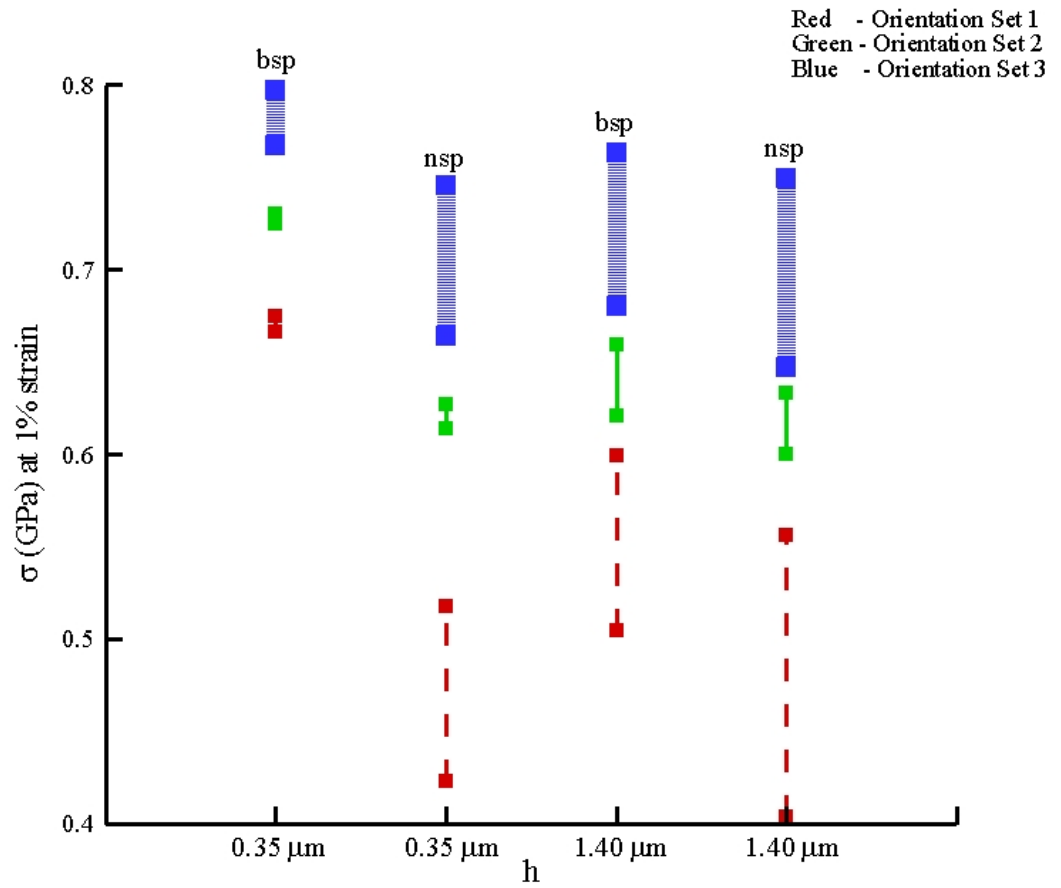


Figure 5.13. Effect of grain boundary constraints on the stress-strain behavior for different orientation sets (For each line, bottom point represents grain boundary unconstrained case and top point represents constrained case; *bsp*- both side passivated; *nsp*- no side passivated)

CHAPTER 6

FINITE DEFORMATION FIELD DISLOCATION MECHANICS

The governing equations, boundary conditions and initial conditions of finite deformation field dislocation mechanics (*FDM/PMFDM*) theory are summarized in this chapter. Details of the theory appear in Acharya (2004) and Acharya and Roy (2006). The salient features are mentioned in Section 6.1 followed by constitutive specifications in Section 6.2. The numerical formulation of the theory using the Finite Element Method is described in Section 6.3 and the algorithm in Section 6.4. Most of Section 6.1 has appeared in references mentioned above. It is included here for this thesis to be self contained. The plastic deformation of unpassivated multicrystalline thin film under plane strain tension is studied using this theory and is discussed in Section 6.5.

6.1 Theory

The field equations of the finite deformation field dislocation mechanics theory may be written as follows (Acharya, 2004):

$$\begin{aligned}
\overset{\circ}{\boldsymbol{\alpha}} &= -\text{curl}(\boldsymbol{\alpha} \times \boldsymbol{V}) \\
\overset{\circ}{\boldsymbol{\alpha}} &\equiv (\text{div } \boldsymbol{v})\boldsymbol{\alpha} + \dot{\boldsymbol{\alpha}} - \boldsymbol{\alpha}\boldsymbol{L}^T \\
\text{curl } \tilde{\boldsymbol{\chi}} &= -\boldsymbol{\alpha} \\
\text{div } \tilde{\boldsymbol{\chi}} &= \mathbf{0} \\
\text{div}(\text{grad } \dot{\boldsymbol{f}}) &= \text{div}(\boldsymbol{\alpha} \times \boldsymbol{V} - \dot{\tilde{\boldsymbol{\chi}}} - \tilde{\boldsymbol{\chi}}\boldsymbol{L}) \\
\boldsymbol{F}^{e-1} &= \tilde{\boldsymbol{\chi}} + \text{grad } \boldsymbol{f} ; \boldsymbol{C}^e = \boldsymbol{F}^{eT} \boldsymbol{F}^e \\
\boldsymbol{T} &= 2\rho \boldsymbol{F}^e \frac{\partial \psi}{\partial \boldsymbol{C}^e} \boldsymbol{F}^{eT} = \boldsymbol{F}^e [\boldsymbol{C} : \boldsymbol{E}^e] \boldsymbol{F}^{eT} \\
\boldsymbol{E}^e &= \frac{1}{2}(\boldsymbol{F}^{eT} \boldsymbol{F}^e - \boldsymbol{I}) \\
\text{div } \boldsymbol{T} &= \mathbf{0};
\end{aligned} \tag{6.1}$$

Here, \boldsymbol{F}^e is the elastic distortion tensor, $\tilde{\boldsymbol{\chi}}$ is the incompatible part of \boldsymbol{F}^{e-1} , $\text{grad } \boldsymbol{f}$ represents the compatible part of \boldsymbol{F}^{e-1} (Figure 6.1), \boldsymbol{f} is the plastic position vector, $\boldsymbol{\alpha}$ is the dislocation density tensor (two point tensor between the current and unstretched lattice configuration), \boldsymbol{V} is the dislocation velocity vector, \boldsymbol{v} represents the velocity field with $\boldsymbol{L} = \text{grad } \boldsymbol{v}$ being the velocity gradient, ψ is the free energy per unit mass dependent only on \boldsymbol{C}^e , ρ is the density and \boldsymbol{T} is the stress tensor. The relation between the $\boldsymbol{\chi}$, \boldsymbol{z} fields of the small deformation theory and the $\tilde{\boldsymbol{\chi}}$, \boldsymbol{f} fields of the finite deformation theory, respectively, is explained in detail in Acharya and Roy (2006). All spatial derivatives are taken with respect to the current configuration and will be discussed in more detail in the numerical formulation (Section 6.3).

Motivated by the averaging of small deformation theory, the equations representing the *average* finite deformation field theory (Acharya and Roy, 2006) are as follows (*The overhead bar for average fields has been removed for convenience*):

$$\begin{aligned}
(\operatorname{div} \mathbf{v}) \boldsymbol{\alpha} + \dot{\boldsymbol{\alpha}} - \boldsymbol{\alpha} \mathbf{L}^T &\equiv \overset{\circ}{\boldsymbol{\alpha}} = -\operatorname{curl} \mathbf{S} \\
\mathbf{S} &= \boldsymbol{\alpha} \times \mathbf{V} + \mathbf{L}^p \\
\operatorname{curl} \tilde{\boldsymbol{\chi}} &= -\boldsymbol{\alpha} \\
\operatorname{div} \tilde{\boldsymbol{\chi}} &= \mathbf{0} \\
\operatorname{div}(\operatorname{grad} \dot{\mathbf{f}}) &= \operatorname{div}(\boldsymbol{\alpha} \times \mathbf{V} + \mathbf{L}^p - \dot{\tilde{\boldsymbol{\chi}}} - \tilde{\boldsymbol{\chi}} \mathbf{L}) \quad (6.2) \\
\mathbf{F}^{e-1} &= \tilde{\boldsymbol{\chi}} + \operatorname{grad} \mathbf{f} \quad ; \quad \mathbf{C}^e = \mathbf{F}^{eT} \mathbf{F}^e \\
\mathbf{T} &= 2\rho \mathbf{F}^e \frac{\partial \psi}{\partial \mathbf{C}^e} \mathbf{F}^{eT} = \mathbf{F}^e [\mathbf{C} : \mathbf{E}^e] \mathbf{F}^{eT} \\
\mathbf{E}^e &= \frac{1}{2} (\mathbf{F}^{eT} \mathbf{F}^e - \mathbf{I}) \\
\operatorname{div} \mathbf{T} &= \mathbf{0}
\end{aligned}$$

\mathbf{S} is the averaged slipping distortion (slip rate), \mathbf{V} is the averaged excess dislocation velocity vector, and \mathbf{L}^p , represents that part of the total slip strain rate which is not represented by the slipping produced by the averaged signed dislocation density (two point tensor). \mathbf{L}^p and \mathbf{V} require constitutive specifications.

6.1.1 *Boundary Conditions:* The following boundary conditions are admitted:

$$\begin{aligned}
\boldsymbol{\chi} \mathbf{n} &= \mathbf{0} \text{ on the boundary } \partial B \text{ of the body with outward unit normal } \mathbf{n}, \\
(\operatorname{grad} \dot{\mathbf{f}}) \mathbf{n} &= (\boldsymbol{\alpha} \times \mathbf{V} + \mathbf{L}^p - \dot{\tilde{\boldsymbol{\chi}}} - \tilde{\boldsymbol{\chi}} \mathbf{L}) \mathbf{n} \text{ on } \partial B, \quad (6.3)
\end{aligned}$$

Standard displacement/traction boundary conditions on ∂B .

where, B is the current configuration. Other than the above conditions, equation (6.2)₁ admits boundary conditions on the dislocation flow (Acharya and Roy, 2006). In general, a natural boundary condition of the form

$$\mathbf{S} \times \mathbf{n} = \boldsymbol{\Phi}, \quad (6.4)$$

where, $\boldsymbol{\Phi}$ is a (second-order tensor valued) specified function of time and position along the boundary satisfying the constraint $\boldsymbol{\Phi} \mathbf{n} = \mathbf{0}$ is appropriate to

model controlled flow at the boundary. A rigid boundary with respect to slipping may be represented with a zero flow boundary condition

$$\mathbf{S} \times \mathbf{n} = \mathbf{0} \quad (6.5)$$

on the entire boundary. Imposing such a boundary condition can lead to the development of shocks or discontinuities. A less restrictive boundary condition is the imposition of the dislocation flux, $\boldsymbol{\alpha}(\mathbf{V} \cdot \mathbf{n})$, on inflow points of the boundary (where $\mathbf{V} \cdot \mathbf{n} < 0$), along with a specification of $\mathbf{L}^p \times \mathbf{n}$ on the entire boundary. This condition allows free exit of dislocations without any added specification.

6.1.2 Initial Conditions: The field equations mentioned above admit initial conditions on the fields \mathbf{u} , $\boldsymbol{\alpha}$ and \mathbf{f} which are as follows. For the \mathbf{u} field we assume $\mathbf{u}|_{t=0} \equiv \mathbf{0}$. Unless otherwise mentioned, we assume that the body is initially dislocation free. Initial condition on the \mathbf{f} field is obtained from solving (6.2)₂₋₃ and (6.2)₅₋₈, with $\mathbf{u}|_{t=0} \equiv \mathbf{0}$.

6.1.3 Auxiliary Condition: \mathbf{f} is specified at an arbitrarily chosen point of the body.

It is generally set to be equal to the reference co-ordinates of the chosen point.

6.2 Constitutive Specification

Physically reasonable choices for the mean (i.e. space-time average) of signed velocity of dislocation segments (that may be associated with the velocity of mean ED), \mathbf{V} , and the mean slip-distortion rate produced by SD, \mathbf{L}^p , are made based on the

requirement of non-negativity of plastic working and ingredients of conventional plasticity theory. The constitutive specifications for a natural extension of crystal plasticity are mentioned below:

$$\begin{aligned} \mathbf{L}^p &= \sum_{\kappa} \text{sgn}(\tau^{\kappa} - \Omega^{\kappa}) \dot{\gamma}^{\kappa} \mathbf{m}_0^{\kappa} \otimes \mathbf{n}^{\kappa} \\ \mathbf{V} &= \nu \frac{\mathbf{d}}{|\mathbf{d}|} ; \nu \geq 0 \end{aligned} \quad (6.6)$$

where, \mathbf{m}_0^{κ} and \mathbf{n}_0^{κ} are the unstretched unit slip direction and normal, respectively, τ^{κ} is the resolved shear stress on slip system κ , \mathbf{d} is the direction of dislocation velocity, Ω^{κ} is the back stress corresponding to individual slip systems κ , $\dot{\gamma}^{\kappa}$ represents the magnitudes of SD slipping rate on the slip system κ and ν is the averaged ED velocity. \mathbf{m}^{κ} and \mathbf{n}^{κ} are the stretched unit slip direction and normal on the current configuration, respectively and are calculated as follows,

$$\mathbf{m}^{\kappa} = \mathbf{F}^e \mathbf{m}_0^{\kappa}; \mathbf{n}^{\kappa} = \mathbf{F}^{e-T} \mathbf{n}_0^{\kappa} \quad (6.7)$$

The resolved shear stress τ^{κ} is calculated as follows:

$$\tau^{\kappa} = \mathbf{m}^{\kappa} \cdot \mathbf{T} \mathbf{n}^{\kappa} \quad (6.8)$$

The expression of back stress is based on the Armstrong–Frederick form,

$$\dot{\Omega}^{\kappa} = \left(|\boldsymbol{\alpha} \mathbf{m}^{\kappa}| + |\boldsymbol{\alpha} \mathbf{p}^{\kappa}| \right) L \mu \dot{\gamma}^{\kappa} - c \Omega^{\kappa} |\dot{\gamma}^{\kappa}| ; \mathbf{p}^{\kappa} = \mathbf{m}^{\kappa} \times \mathbf{n}^{\kappa} \quad (6.9)$$

where, L is the hardening coefficient and c is the recovery coefficient. The direction of the dislocation velocity, \mathbf{d} is,

$$\begin{aligned} \mathbf{d} &:= \mathbf{b} - \left(\mathbf{b} \cdot \frac{\mathbf{a}}{|\mathbf{a}|} \right) \frac{\mathbf{a}}{|\mathbf{a}|}, \\ \mathbf{b} &:= \mathbf{X}(\mathbf{T}' \boldsymbol{\alpha}) ; b_i = e_{ijk} T'_{jr} \alpha_{rk} ; \mathbf{a} := \mathbf{X}(\text{tr}(\mathbf{T}) \boldsymbol{\alpha}) ; a_i = \left(\frac{1}{3} T_{mm} \right) e_{ijk} \alpha_{jk}. \end{aligned} \quad (6.10)$$

Power law relation is chosen for $\dot{\gamma}^\kappa$,

$$\dot{\gamma}^\kappa = \dot{\gamma}_0^\kappa \left(\frac{|\tau^\kappa - \Omega^\kappa|}{g} \right)^{\frac{1}{m}} \quad (6.11)$$

where, m is the rate-sensitivity of the material, g is the strength of the material, and $\dot{\gamma}_0$ is a reference strain rate. The expression for v is assumed to be

$$v(state) = \frac{\eta^2 b}{n_{slip}} \left(\frac{\mu}{g} \right)^2 \sum_{\kappa} \dot{\gamma}^\kappa \quad (6.12)$$

where μ is the shear modulus, b the Burgers vector magnitude, n_{slip} is the total number of slip systems and $\eta = 1/3$ a material parameter.

The strength of the material is assumed to evolve according to

$$\dot{g} = \left[\frac{\eta^2 \mu^2 b}{2(g - g_0)} k_0 |\alpha n^\kappa| + \theta_0 \left(\frac{g_s - g}{g_s - g_0} \right) \right] \left\{ |\alpha \times V| + \sum_{\kappa} \dot{\gamma}^\kappa \right\} \quad (6.13)$$

where g_s is the saturation stress, g_0 is the yield stress, and θ_0 is the Stage II hardening rate.

6.3 Numerical Formulation

This section is a contribution of this thesis work. The discretization methods for the equations of finite deformation theory are similar to those used for the corresponding small deformation equations.

The symbol $\delta(\cdot)$ represents a variation (or test function) associated with the field (\cdot) in a suitable class of functions. $\delta(\cdot)$ is arbitrary up to satisfying any prescribed essential boundary conditions for the field (\cdot) . An increment of time $[t, t + \Delta t]$ is considered, and fields without any superscripts refer to values at $t + \Delta t$ and those

with the superscript t refer to values at time t . All spatial fields are discretized by first-order, 8-node (three-dimensional), isoparametric brick elements.

The discretized equation for (6.2)₁ in components with respect to an orthonormal basis is,

$$\begin{aligned}
& \int_B \delta\alpha_{ij} (\alpha_{ij} - \alpha'_{ij}) dv - \Delta t \int_B [\delta\alpha_{ij,k} \alpha_{ij} V'_k - \delta\alpha_{ij,k} \alpha_{ik} V'_j] dv \\
& + \Delta t \int_{\partial B_s} \delta\alpha_{ij} F_{ij} da + \Delta t \int_{\partial B_s} \delta\alpha_{ij} \alpha'_{ij} (V'_k n'_k) da - \Delta t \int_{\partial B} \delta\alpha_{ij} \alpha'_{ik} n'_k V'_j da \\
& - \Delta t \int_B \delta\alpha_{ij,k} e_{jkl} L_{il}^{p \prime} dv + \Delta t \int_{\partial B} \delta\alpha_{ij} e_{jkl} L_{il}^{p \prime} n'_k da \\
& - \Delta t \int_B \delta\alpha_{ij} \alpha_{ik} L'_{jk} dv + \Delta t \int_B \delta\alpha_{ij} \alpha'_{ij} v'_{k,k} dv \\
& + \int_{B_{interiors}} A_{ri} (\delta\alpha_{ri} + \Delta t [\delta\alpha_{ri,j} V'_j + \delta\alpha_{ri} V'_{j,j} - \delta\alpha_{rj,j} V'_i - \delta\alpha_{rj} V'_{i,j} - \delta\alpha_{rj} L'_{ij} + \delta\alpha_{ri} v'_{j,j}]) dv = 0
\end{aligned} \tag{6.14}$$

where,

$$A_{ri} = \alpha_{ri} - \alpha'_{ri} + \Delta t [\alpha'_{ri,j} V'_j + \alpha'_{ri} V'_{j,j} - \alpha'_{rj,j} V'_i - \alpha'_{rj} V'_{i,j} + e_{ijk} L'_{rk,j} - \alpha'_{rj} L'_{ij} + \alpha'_{ri} v'_{j,j}] \tag{6.15}$$

All the spatial derivatives in (6.14) and (6.15) are taken with respect to the current configuration at time t .

The equation for (6.2)₂₋₃, is given by

$$\int_B e_{ijk} \delta\tilde{\chi}_{rk,j} [e_{imn} \tilde{\chi}_{rn,m} - \alpha_{ri}] dv + \int_B \delta\tilde{\chi}_{ij,j} \tilde{\chi}_{im,m} dv = 0. \tag{6.16}$$

The essential boundary condition (2.11)₁ needs to be imposed and requires, in certain circumstances, the use of linear constraint equations. All the spatial derivatives in (6.16) are taken with respect to the current configuration at time $t + \Delta t$ (details in Table 6.1).

The discretization of (6.2)₄ is

$$\int_B \delta f_{i,j} [f_{i,j} - f'_{i,j} - \Delta t (L'_{ij}{}^t + e_{jmk} \alpha'_{im} V'_k) + \tilde{\chi}'_{ij} - \tilde{\chi}'_{ij}{}^{t-\Delta t} + \Delta t \tilde{\chi}'_{im} L'_{mj}] dv = 0 \tag{6.17}$$

specify $f'_i = 0$ at an arbitrarily chosen point.

All the spatial derivatives in the above equation are taken with respect to the current configuration at time t .

The discretized form of the equilibrium equation (6.2)₈ is,

$$\int_B \delta u_{i,j} T_{ij} dv - \int_{\partial B_i} \delta u_i t_i da = 0 \quad (6.18)$$

and standard displacement b.c.s.

Under traction-free boundary conditions on ∂B_i , (6.18) reduces to,

$$\int_B \delta u_{i,j} T_{ij} dv = 0 \quad (6.19)$$

Equation (6.19) is solved using the Newton-Raphson algorithm. The expression for the residual, R , in discrete form is,

$$R = \delta u_i^A \int_B \frac{\partial N^A}{\partial x_j} T_{ij} dv \quad (6.20)$$

where, $\delta u_i = \delta u_i^A N^A$, N^A is the conventional FEM shape function corresponding to node A , u_i^A is the nodal value of displacement, and x_j represents current configuration at time $t + \Delta t$. The variation of (6.19) is calculated to get the Jacobian, Π ,

$$\begin{aligned}
\Pi = & -\delta u_i^A \left[\int_B \frac{\partial N^A}{\partial X_m} \frac{\partial N^C}{\partial X_p} F_{mn}^{-1} F_{pj}^{-1} T_{ij} dv \right] du_n^C + \\
& \delta u_i^A \left[\int_B \frac{1}{J} F_{mn}^{e-1} \tau_{nj} \frac{\partial N^A}{\partial x_j} F_{ia}^e \frac{\partial f_a}{\partial X_b} F_{bl}^{-1} \frac{\partial N^C}{\partial X_d} F_{de}^{-1} F_{em}^e dv \right] du_l^C + \\
& \delta u_i^A \left[\int_B \frac{1}{J} F_{mn}^{e-T} \tau_{im} \frac{\partial N^A}{\partial x_j} F_{bn}^e F_{lb}^{-1} F_{ed}^{e-1} \frac{\partial f_f}{\partial X_e} F_{if}^e \frac{\partial N^C}{\partial X_l} dv \right] du_d^C + \\
& \delta u_i^A \left[\int_B \frac{1}{J} F_{im}^e C_{mnab} F_{cb}^e F_{jn}^e \frac{\partial N^A}{\partial x_j} F_{da}^e F_{ed}^{-1} \frac{\partial N^C}{\partial X_e} F_{gf}^{-1} \frac{\partial f_k}{\partial X_g} F_{ck}^e dv \right] du_f^C + \\
& \delta u_i^A \left[\int_B \frac{1}{J} F_{im}^e C_{mnab} F_{ca}^e F_{jn}^e \frac{\partial N^A}{\partial x_j} F_{cd}^e \frac{\partial f_d}{\partial X_e} F_{ef}^{-1} \frac{\partial N^C}{\partial X_g} F_{gk}^{-1} F_{kb}^e dv \right] du_f^C
\end{aligned} \tag{6.21}$$

where, $\boldsymbol{\tau}$ is the Kirchhoff stress tensor, J is the determinant of the deformation gradient \mathbf{F} , \mathbf{X} represent the reference configuration and \mathbf{x} represents the current configuration at time $t + \Delta t$ (details in Table 6.1).

6.4 Algorithm

Like the small deformation algorithm, here also a problem is typically solved in steps. The details are given in Table 6.1. The time step in this case is controlled by

$$\Delta t \leq \min \left\{ f \frac{h}{|\mathbf{V}|}, \frac{0.002}{|\boldsymbol{\alpha} \times \mathbf{V}| + \sum_{\kappa} \dot{\gamma}^{\kappa}} \right\}, \quad f \sim 0.1. \tag{6.22}$$

Table 6.1. Solution procedure for the equations of finite deformation theory.

<p>Given: material properties, initial conditions (α_0), boundary conditions, total time (t_{tot}), strain rate.</p>
<p>Step 1: Static problem, finding initial value of f_0 and stress, T_0 (all the spatial derivatives are with respect to reference co-ordinates).</p> <ul style="list-style-type: none"> • Make a guess for f (set to be equal to reference co-ordinates). • Solve for $\tilde{\chi}$ using $curl \tilde{\chi} = -\alpha_0$; $div \tilde{\chi} = 0$; $\tilde{\chi}n = 0$ on ∂B. • Calculate $F^{e-1} = \tilde{\chi} + \frac{\partial f}{\partial X}$; $E^e = \frac{1}{2}(F^{eT} F^e - I)$; $T = F^e [C : E^e] F^{eT}$ • Solve for f using the equilibrium equation, $div T = 0$. This equation is non-linear and solved using the Newton Raphson method. The convergence of a particular iteration is assured by controlling the residual in the following manner, $\frac{f_{\max}}{G} \leq tol$ $G = g_0 \times Area$ <p>where,</p> <p>f_i = value of residual at a particular node for a specific degree of freedom, f_{\max} = maximum value of f_i in the current iteration of the current increment, g_0 = initial yield strength, $Area$ = area of any face of the sample (preferably the largest), tol = tolerance.</p> <ul style="list-style-type: none"> • Update f_0, T_0.
<p>Step 2: Time evolving analysis</p> <p>This step is solved in increments of time, Δt. Δt is calculated as per (6.22). For a particular increment the state at time t is known and the objective is to calculate the state at $t + \Delta t$. This is achieved by following the steps below:</p> <ul style="list-style-type: none"> • Solve for $\alpha^{t+\Delta t}$ using the transport equation (all the spatial derivatives are with respect to the current configuration at time t), $\dot{\alpha} = -curl(\alpha \times V^t + L^{p^t}) + \alpha L^{T^t} - (div v^t) \alpha$ <ul style="list-style-type: none"> • Solve for $f^{t+\Delta t}$ using $div(grad \dot{f}) = div(\alpha \times V^t + L^{p^t} - \dot{\tilde{\chi}}^t - \tilde{\chi}^t L^t)$.

(all the spatial derivatives are with respect to the current configuration at time t)

- Solve for $\tilde{\chi}^{t+\Delta t}$ and $\mathbf{u}_{t+\Delta t}$ in the following way:

1. Make a guess for displacement, \mathbf{u}_{guess} ,

2. Update co-ordinates/geometry, $\mathbf{x}_{guess} = \mathbf{x}_t + \mathbf{u}_{guess}$.

3. Solve for $\tilde{\chi}^{t+\Delta t}$ using

$curl \tilde{\chi} = -\boldsymbol{\alpha}^{t+\Delta t}$; $div \tilde{\chi} = \mathbf{0}$; $\tilde{\chi}\mathbf{n} = \mathbf{0}$ on ∂B (all the spatial derivatives are with respect to the guessed configuration).

4. Calculate

$$\mathbf{F}^{e-1} = \tilde{\chi}^{t+\Delta t} + grad \mathbf{f}^{t+\Delta t};$$

$$\mathbf{E}^e = \frac{1}{2}(\mathbf{F}^{eT} \mathbf{F}^e - \mathbf{I}); \mathbf{T} = \mathbf{F}^e [\mathbf{C} : \mathbf{E}^e] \mathbf{F}^{eT}$$
 (the spatial

derivative is with respect to the guessed configuration)

5. Calculate \mathbf{u}_{corr} using the equilibrium equation, $div \mathbf{T} = \mathbf{0}$. The spatial derivative is with respect to the guessed configuration in first iteration. In the subsequent iterations for calculating \mathbf{u}_{corr} , corrected configuration, $\mathbf{x}_{corr} = \mathbf{x}_t + \mathbf{u}_{corr}$ is used. This system of equations is non-linear as mentioned in Step 1. The jacobian calculation, (6.21), here is non-trivial and very different from the corresponding small deformation case due to the change of configuration in every iteration. The convergence of a Newton Raphson iteration is controlled in the following manner (motivated from Abaqus, 2002),

$$\frac{f_{\max}}{G} \leq tol$$

$$G = \frac{1}{l} \sum_{k=1}^l F_k ; F_k = \frac{1}{mn_j} \sum_{j=1}^m \sum_{i=1}^{n_j} f_i$$

where,

f_i = value of |residual| at a particular node for a specific degree of freedom,

f_{\max} = maximum value of f_i in the current iteration of the current increment,

l = total number of increments, excluding the current increment,

n_j = total number of displacement degree of freedoms of j^{th} node
with prescribed boundary condition,

m = total number of nodes with at least one degree of freedom having
a prescribed boundary condition,

tol = tolerance.

F_k = spatial average of f_i in k^{th} increment, and

G = average of F_k over l increments.

6. Repeat (1)-(5) with \mathbf{u}_{corr} as the guess displacement, unless
 $(\mathbf{u}_{guess} - \mathbf{u}_{corr}) < tol$, tol is the tolerance.

6.5 Plastic Deformation of Thin Films

The plastic deformation of multicrystalline thin films is analyzed using the finite deformation PMFDM theory to test the numerical implementation. A few partial verification tests were done:

- a. Finite Elasticity problem: A cube was deformed elastically with boundary conditions corresponding to plane strain tension. Stresses matching the analytical solution were achieved with quadratic convergence at 100% applied strain.
- b. Formation of a Slip-step when an edge dislocation exits the surface of a cubic sample.

The problem setup and boundary conditions for analyzing the deformation of multicrystalline thin film are same as used in Section 5.1 for the small deformation case. In this section the film with misorientation between adjacent grains in the range

of 3-5 degrees about the X_3 -axis is used. Grain boundaries are considered to be impenetrable to dislocations. Boundary conditions for imposing constraints on grain boundaries are the same as mentioned in Chapter 4. A film with $h = 0.35\mu m$ and no surface passivation is considered (problem setup and meaning of h is shown in Figure 5.1).

Material parameters representative of Copper are used for all the computational experiments presented in this chapter; $b = 2.5 \times 10^{-4} \mu m$, $m = 0.1$, $g_s = 210$ MPa, $g_0 = 50$ MPa, $\theta_0 = 205$ MPa, $k_0 = 20.0$, $L = 100$, and $c = 100$. The physical meaning of these parameters is described in Chapter 2. The reference strain rate is $\dot{\gamma}_0 = 1 \text{ sec}^{-1}$. Isotropic elastic constants of the representative material are $E = 110$ GPa, $\nu = 0.34$, where E is the Young's modulus and ν is the Poisson's ratio. The value of the penalty parameter, k , required for solving the set of equations for z is set to zero in this case (mentioned in Section 4.1).

The stress-strain response till 1% applied strain from finite deformation theory comes out to be similar to that from small deformation theory as shown in Figure 6.2(a). Accumulation of dislocations along the grain boundary is observed in both cases but the spatial distribution of norm of excess dislocation density seems to be different (Figure 6.2(b), (c)).

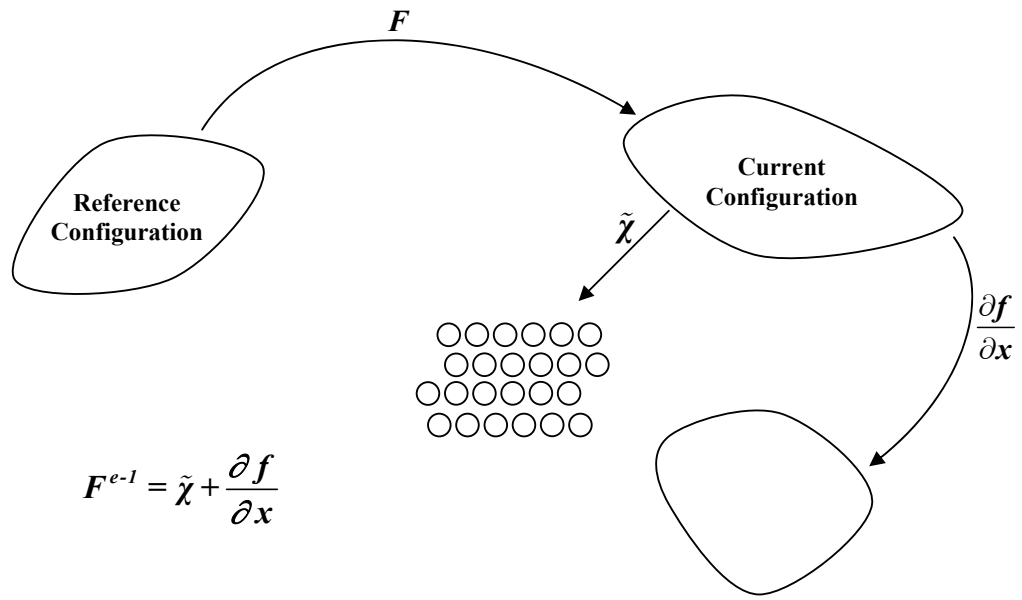


Figure 6.1. Schematic showing the significance of $\tilde{\chi}$ and $\frac{\partial f}{\partial x}$

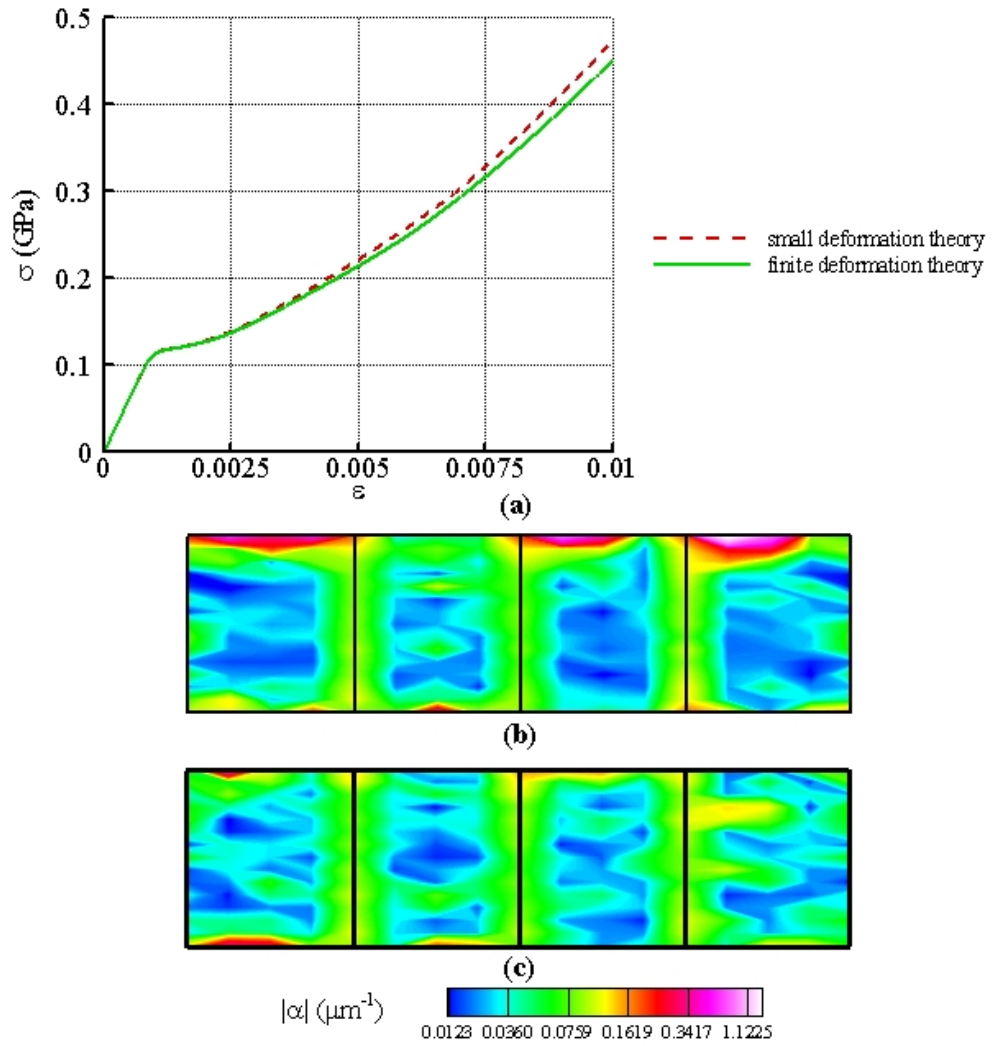


Figure 6.2. Comparison of results from small and finite deformation *PMFDM* theory; (a) stress-strain curve; (b) field plot from small deformation theory; (c) field plot from finite deformation theory.

CHAPTER 7

CONCLUSIONS

The small deformation Mesoscopic Field Dislocation Mechanics theory with constitutive specifications based on $J2$ plasticity theory was already implemented and shown to be successful in predicting some benchmark plasticity problems in Roy (2005). A part of this thesis involves using that framework to model physical problems of current interest. First, some aspects of a distribution of Frank Read source are modeled in the current setup. The developed strategy is then used to model the size effects at initial yield in micron sized specimens. It is inferred from the numerical experiments performed here that the length scales introduced in the model due to the discrete source patterns and the mobility of ED are exclusively responsible for size effects at initial yield. One novel feature of this work is that the dislocation source related size effects are shown in a continuum theory. In order to model the experiments showing size effects at initial yield at sufficiently small scale where individual excess dislocations need to be resolved, *FDM* with non-convex elasticity can be used.

An important contribution of this thesis is the incorporation of crystal plasticity theory into the *PMFDM* model. Another important contribution of this thesis is a framework for modeling controlled plastic flow through grain boundaries. Grain boundaries are usually considered to be impenetrable to dislocations in the modeling of polycrystals in DD (Nicola *et al.*, 2006) and in conventional plasticity their status with respect to explicit effect in mediating plastic flow through them is uncertain. However, constraints on plastic flow through them can have a significant effect on the

microstructure evolution and consequently on the mechanical response. The difference in the mechanical behavior of penetrable and impenetrable grain boundaries is demonstrated through a test case involving the deformation of a bicrystal. In the current modeling of polycrystals, grain boundaries are considered to be stationary. An exact expression for moving grain boundaries have been worked out in Acharya (2007) and needs to be implemented.

With crystal plasticity and a control on plastic flow through grain boundaries, the model was used to predict size effect and unusual Bauschinger effect observed experimentally in polycrystalline thin films undergoing subsequent cycles of plane strain tension and compression. It was concluded from these computational experiments that the grain orientation, surface passivation, thickness and grain boundary constraints significantly affect the mechanical response of thin films.

The effect of lattice rotations is neglected in the study of mechanical response of multicrystalline thin films mentioned in this thesis. However, the interaction of lattice rotations and grain boundary plays a very important role in microstructure evolution and mechanical response. The last part of the thesis involves the implementation of finite deformation *PMFDM* theory.

While there are certain constitutive assumptions involved in the *PMFDM* model, qualitative features like the modeling of dislocation sources, modeling of plastic flow through grain boundaries and effect of passivation on the dislocation microstructure development are independent of these assumptions. The effect of external dimensions of the sample on the mechanical response depends partly on the constitutive assumptions for dislocation velocity and strength evolution.

PMFDM coupled with computational implementation has been successful in modelling some key experimental observations, specifically, size effects in work hardening and initial yield, and Bauschinger effect. These features cannot be modeled using the conventional crystal plasticity theory. With an increase in demand of small scale technological devices it is advantageous to have a continuum model to study the deformation mechanisms at such spatial scales. The computational efficiency associated with continuum models allow them to be used at realistic strain rates.

REFERENCES

- Acharya, A., 2001, A model of crystal plasticity based on the theory of continuously distributed dislocations, *Journal of the Mechanics and Physics of Solids* 49, 761- 785.
- Acharya, A., 2003, Driving forces and boundary conditions in continuum dislocation mechanics, *Proceedings of the Royal Society A* 459, 1343- 1363.
- Acharya, A., 2004, Constitutive analysis of finite deformation field dislocation mechanics, *Journal of the Mechanics and Physics of Solids* 52, 301- 316.
- Acharya, A., 2007, Jump condition for GND evolution as a constraint on slip transmission at grain boundaries, *Philosophical Magazine*, 87, 1349-1359.
- Acharya, A., Beaudoin, A. J., 2000, Grain size effect in viscoplastic polycrystals at moderate strains, *Journal of the Mechanics and Physics of Solids* 48, 2213-2230.
- Acharya, A., Beaudoin, A., Miller, R., 2008, New perspectives in plasticity theory: dislocation nucleation, waves, and partial continuity of plastic strain rate, *Mathematics and Mechanics of Solids*, 13, 292-315.
- Acharya, A., Roy, A., 2006, Size effects and idealized dislocation microstructure at small scales: Predictions of a Phenomenological model of Mesoscopic Field Dislocation Mechanics: Part I, *Journal of the Mechanics and Physics of Solids* 54, 1687- 1710.
- Ahmed, J., Wilkinson, A. J., Roberts, S. G., 1997, Characterizing dislocation structures in bulk fatigued copper single crystals using electron channeling contrast imaging (ECCI), *Philosophical Magazine Letters*, 76, 237-245.
- Ahmed, J., Wilkinson, A. J., Roberts, S. G., 2001, Electron channeling contrast imaging characterization of dislocation structures associated with extrusion and intrusion systems and fatigue cracks in copper single crystals, *Philosophical Magazine Letters*, 76, 237-245.
- Armstrong, P.J., and Frederick, C.O., 1966, A mathematical representation of the multiaxial Bauschinger effect, Technical Report C. E. G. B., Report RD/B/N731, Berkeley Nuclear Laboratories.
- Asaro, R. J., 1983, Micromechanics of Crystals and Polycrystals, *Advances in Applied Mechanics*, 23, 1-115.
- Babic, M., 1997, Average balance equations for granular materials, *Int J Eng Sci*, 35, 523-548.
- Balay, S., Buschelman, K., Gropp, W.D., Kaushik, D., Knepley, M.G., McInnes, L.C., Smith, B.F., Zhang, H., 2001. PetSc Web page. <http://www.mcs.anl.gov/petsc>.
- Balint, D. S., Deshpande, V. S., Needleman. A., Van der Giessen, E., 2006, Size effects in uniaxial deformation of single and polycrystals: a discrete dislocation plasticity analysis, *Modelling and Simulation in Materials Science and Engineering* 14, 409– 422.
- Beaudoin, A. J., Acharya, A., Chen, S. R., Korzekwa, D. A., Stout, M. G., 2000, Consideration of grain-size effect and kinetics in the plastic deformation of metal polycrystals, *Acta Metallurgica* 48, 3409-3423.

- Benzerga, A. A., Brechet, Y., Needleman, A., Van der Giessen, E., 2005, The stored energy of cold work: Predictions from discrete dislocation plasticity, *Acta Materialia* 53, 4765- 4779.
- Benzerga, A. A., Shaver, N. F., 2006, Scale dependence of mechanical properties of single crystals under uniform deformation, *Scripta Materialia* 54, 1937– 1941.
- Chang, Y.W. and Asaro, R.J., 1981, An experimental study of shear localization in aluminum-copper single crystals. *Acta Metall.*, 29, 241-257.
- Convergence Criteria for nonlinear problems, ABAQUS/Standard User's manual, 2002, Volume 1, 8.3.3 (1-11).
- Deshpande, V. S, Needleman, A., Van der Giessen, E., 2001, Dislocation dynamics is chaotic, *Scripta Mater.* 45, 1047-1053.
- Deshpande, V. S., Needleman. A., Van der Giessen, E., 2005, Plasticity Size effects in tension and compression of single crystals, *Journal of the Mechanics and Physics of Solids* 53, 2661-2691.
- Dimiduk, D., M., Uchic, M. D., Parthasarathy, T. A., 2005, Size-affected single-slip behavior of pure nickel microcrystals, *Acta Materialia* 53, 4065– 4077.
- Espinosa, H.D., Prorok, B.C., and Peng, B., 2004, Plasticity size effects in free-standing submicron polycrystalline FCC -films subjected to pure tension, *Journal of the Mechanics and Physics of Solids*, 52, 667 – 689.
- Fleck, N. A., Muller, G. M., Ashby, M. F., Hutchinson, J. W., 1994, Strain gradient plasticity: theory and experiment, *Acta Metallurgica et Materialia* 42, 475– 487.
- Frick, C. P., Clark, B. G., Orso, S., Schneider, A. S., and Arzt, E., 2008, Size effect on strength and strain hardening of small-scale [1 1 1] nickel compression pillars, *Materials Science and Engineering A*, 489, 319–329.
- Greer, J. R., Oliver, W. C., Nix, W. D., 2005, Size dependence of mechanical properties of gold at the micron scale in the absence of strain gradients, *Acta Materialia* 53, 1821- 1830.
- Gurtin, M.E., 2000, On the plasticity of single crystals: free energy, microforces, plastic strain gradients, *J. Mech. Phys. Solids*, 48, 989–1036.
- Gurtin, M.E., 2002, A gradient theory of single-crystal viscoplasticity that accounts for geometrically necessary dislocations, *J. Mech. Phys. Solids*, 50, 5– 32.
- Gurtin, M.E., 2004, A gradient theory of small-deformation isotropic plasticity that accounts for the Burgers vector and for dissipation due to plastic spin, *J. Mech. Phys. Solids* 52, 2545–2568.
- Gurtin, M.E., and Anand, L., 2005, A theory of strain-gradient plasticity for isotropic, plastically irrotational materials, Part I: Small deformations, *J. Mech. Phys. Solids*, 53, 1624–1649.
- Hughes, D., Hansen, N., 1997, High-angle boundaries formed by grain subdivision mechanisms, *Acta Materialia*, 45, 3871-3886.
- Hughes, T.J.R., Franca, L.P., Hulbert, G.M. (1989) A New Finite-Element Formulation For Computational Fluid-Dynamics .8. The Galerkin/Least-Squares Method For Advective-Diffusive Equations. *Computer Methods In Applied Mechanics And Engineering*, 73, 173-189.
- Kroner, E., 1981, Continuum theory of defects, In: Balian, R., et al. (Ed.), *Physics of Defects*, North-Holland Publishing Company, Amsterdam, 217–315.

- Kubin, L.P., Canova, G., Condat, M., Devincere, B., Pontikis, V., Brechet, Y., 1992, Dislocation microstructure and plastic flow: a 3-D simulation. *Solid State Phenomena*, 23 & 24, 455–472.
- Ma, Q., Clarke, D. R., 1995, Size-dependent hardness of silver single-crystals, *Journal of Materials Research* 10 (4), 853– 863.
- Mugharbi, H., Ackermann, F., Herz, K., 1979, Persistent slip bands in fatigued face centered and body centered cubic metals, Technical Report, American Society for Testing and Materials, Philadelphia, 69-105.
- Mura, T., 1963, Continuous distribution of moving dislocations, *Philosophical Magazine*, 89, 843–857.
- Nicola, L., Xiang, Y., Vlassak, J.J., Van der Giessen, E. and Needleman, A., 2006, Plastic deformation of freestanding thin films: Experiments and modeling, *Journal of the Mechanics and Physics of Solids*, 54, 2089–2110.
- Norfleet, D. M., Dimiduk, D. M., Polasik, S. J., Uchic, M. D., Mills, M. J., 2008, Examination of Dislocation Structures and Their Relationship to Strength of Pure Nickel Microcrystals, *Acta Materialia*, submitted for publication.
- Nye, J. F., 1953, Some geometrical relations in dislocated crystals, *Acta Metallurgica* 1, 153-162
- Ortiz M. and Phillips R., 1999, Nanomechanics of Defects in Solids, *Advances in Applied Mechanics*, 36, 1-79.
- Parthasarathy, T. A., Rao, S. I., Dimiduk, D. M., Uchic, M. D., Trinkle, D. R., 2006, Contribution to size effect of yield strength from the stochastics of dislocation source lengths in finite samples, *Scripta Materialia* 56, 313-316.
- Puri, S., Roy, A., Acharya, A., Dimiduk, D., 2008, Modeling dislocation sources and size effects at initial yield in continuum plasticity, accepted in *Journal of Mechanics of Materials and Structures*.
- Rao, S. I., Dimiduk, D. M., Parthasarathy, T. A., Uchic, M. D., Tang, M., Woodward, C., 2008, Athermal mechanisms of size-dependent crystal flow gleaned from three dimensional discrete dislocation simulations, *Acta Materialia*, submitted for publication.
- Roy A., 2005, Computational Approach to Phenomenological Mesoscopic Field Dislocation Mechanics, Ph.D. Thesis.
- Roy, A., Acharya, A., 2005, Finite element approximation of field dislocation Mechanics, *Journal of the Mechanics and Physics of Solids* 53, 143-170.
- Roy, A., Acharya, A., 2006, Size effects and idealized dislocation microstructure at small scales: Predictions of a Phenomenological model of Mesoscopic Field Dislocation Mechanics: Part II, *Journal of the Mechanics and Physics of Solids* 54, 1711- 1743.
- Roy, A., Puri, S., Acharya, A., 2007, Phenomenological mesoscopic field dislocation mechanics, lower-order gradient plasticity, and transport of mean excess dislocation density, *Modelling Simul. Mater. Sci. Eng.* ,15, S167–S180.
- Senger, J., Weygand, D., Gumbsch, P., and Kraft, O., 2008, Discrete dislocation simulations of the plasticity of micro-pillars under uniaxial loading, *Scripta Mater.* 58, 587-590.
- Stölken, J. S., Evans, A. G., 1998, A microbend test method for measuring the plasticity length scale, *Acta Materialia* 46 (14), 5109-5115.
- Tang, H., Schwarz, K. W., Espinosa, H. D., 2007, Dislocation escape-related size effects in single-crystal micropillars under uniaxial compression, *Acta Materialia* 55, 1607- 1616.

- Tang, H., Schwarz, K. W., Espinosa, H. D., 2008, Dislocation-source shutdown and the plastic behavior of single-crystal micropillars, *Physical Review Letters* 100, 185503-1-4
- Uchic, M. D., Dimiduk, D. M., Florando, J. N., Nix, W. D., 2004, Sample dimensions influence strength and crystal plasticity, *Science* 305, 986-989.
- Van der Giessen, E. and Needleman, A., 1995, Discrete dislocation plasticity: A simple planar approach, *Modelling and Simulation in Materials Science and Engineering*, 3, 689-735.
- Varadhan, S. N., Beaudoin, A. J., Acharya A., Fressengeas, C., 2006, Dislocation transport using an explicit Galerkin/least-squares formulation, *Modelling and Simulation in Materials Science and Engineering* 14, 1245-1270.
- Weygand, D., Poignant, M., Gumbsch, P., Kraft, O., 2007, Three-dimensional dislocation dynamics simulation of the influence of sample size on the stress-strain behavior of fcc single-crystalline pillars, *Mater. Sci. Engr. A*, in press
- Willis, J. R., 1967, Second-order effects of dislocations in anisotropic crystals, *Int. J. Eng. Sci.*, 5, 171-190.
- Xiang, Y., and Vlassak, J. J., 2006, Bauschinger and size effects in thin-film plasticity, *Acta Materialia*, 54, 5449-5460.